Fabrication and characterization of nano carbon-based electrochemical double-layer capacitors

by

Jin Hee Kang

A thesis
presented to the University of Waterloo
in fulfilment of the
thesis requirement for the degree of
Doctor of Philosophy
in
Mechanical Engineering (Nanotechnology)

Waterloo, Ontario, Canada, 2015

I hereby declare that I am the sole author of this thesis. This is a true copy of the thesis, including any required final revisions, as accepted by my examiners. I understand that my thesis may be made electronically available to the public.

Abstract

Porous electrode is a key component in electrochemical double layer capacitors (EDLCs), also called supercapacitors, which provides effective charge storage sites and ion transport channels along the electric double-layer interface between a solid electrode surface and liquid electrolyte. In particular, the micro-structure of an electrode is extremely important to optimize the ion's transport channel and subsequently increasing the ion storage capacity on porous electrodes. This research focuses on three types of porous carbon materials, activated carbon (AC), graphene and single-walled carbon nanotube (SWCNT), with varying surface area and internal porosity as electrode materials. Depending on the type of carbon materials, three different fabrication methods, cast-coating, electrophotretic deposition (EPD) and vacuum filtration deposition, were developed to exploit the unique properties of electrodes. Their structural, electrochemical, thermodynamic properties were characterized, and the temperature/frequency-dependent capacitive and resistive behaviors were correlated to the microstructures, BET surface area, pore size and pore size distribution (PSD) of the electrodes. Under various operating temperatures between -30 ℃ and 60 ℃ and frequency operations, these electrochemical parameters were quantified using cyclic voltammetry (CV), constant current charging/discharging (CCD) measurements and electrochemical impedance spectroscopy (EIS). The differences in their temperature/frequency-dependent characteristics, including their current response to high scan rates, capacitance retention, resistance variation, and degradation of energy and power densities, were addressed by investigating ion kinetics and transport into the micro-, or meso-pores of the electrodes.

An equivalent circuit model for an EDLC device was proposed through analyzing the EIS measurements. This model was developed based on the Grahame theory, while the effects of charge diffusion and the ion adsorption at the double-layer interface and bulk media were investigated. This circuit model, upon its validation against the EIS data, was successfully applied to characterize practical EDLC devices. Experimental results were obtained from different EDLC cells consisting of activated carbon-based electrodes and two distinct electrolytes, aqueous (H_2SO_4) and organic (Et_4NBF_4/PC). The model predicted the useful parameters (such as charge transfer, diffusion, adsorption and bulk media impedance) which help interpret electrochemical processes at the electrode/electrolyte interface. The quantitative dependence of impedance on the applied electrode potential was analyzed for the two electrolytes during charging/discharging, and its correlation with the internal resistance (referred ESR) was derived. Their temperature-dependent electrochemical properties were also investigated using a specified characterization procedure, and the capacitance, internal resistance and energy/power densities of the two capacitors were quantified. The temperature dependency of their impedances was analyzed through simulations of the EIS data by the proposed equivalent circuit model. The simulated impedances were then utilized to address the performance discrepancies between the two electrolytes.

Acknowledgements

I would like to thank my advisors, Prof. John Wen and Prof. Sheshakamal Jayaram, for providing me continuous support and encouragement throughout my graduate study. I appreciate all your help and efforts in developing my experimental skills, writing style and pushing me to publish valuable research papers. I am grateful about the comments and constructive suggestions given by my committee members: Prof. Zhongwei Chen, Prof. Soo Jeon, Prof. Xianguo Li and Prof. Igor Zhitomirsky. I would also like to thank Prof. Aiping Yu for opening her lab to me and sharing her equipment.

I would like to express my gratitude to all research members in the Lab for Emerging Energy Research, Sanam Atashin, John Rawlins, Abhishek Raj, Kang Pan and Mohammad Saleh Lavaee.

Very special thanks to my wife and two adorable daughters for their love and support. Most notably, I would like to thank my wife for supporting me emotionally and exploring a new life in Canada. I am also grateful for my family in Korea. Without them, I would never have even dreamed of attaining a Ph.D.

Table of Contents

Author’s Declaration ii

Abstract iii

Acknowledgements v

Table of Contents vi

List of Figures ix

List of Tables xiv

List of Abbreviations xvi

Chapter 1. Introduction 1

1.1 Energy Storage Systems 1

1.2 Electrochemical Capacitors (ECs) and its Applications, Challenges 4

1.3 Research Objectives 8

Chapter 2. Background and Literature Review 11

2.1 Principles of Electrochemical Capacitors 11

2.1.1 Electrochemical Double-Layer Capacitor (EDLC) 12

2.1.2 Pseudo-Capacitors 15

2.1.3 Electrochemistry in ECs 17

2.1.3.1 Thermodynamic Considerations 17

2.1.3.2 Kinetic Considerations 19

2.1.4 Critical Parameters in EC Design and Performance 24

2.2 Materials and Components of ECs 28

2.2.1 Carbon Materials as Electrodes in EDLCs 29

2.2.1.1 Activated Carbon 30

2.2.1.2 Carbon Nanotube 31

2.2.1.3 Graphene 35

2.2.2 Electrode Fabrication Methods 37

2.2.2.1 Cast-Coating 38

2.2.2.2 Electrophoretic Deposition (EPD) 39

2.2.2.3 Vacuum Filtration Method 42

2.2.3 Electrolytes in EC 44
2.2.3.1 Inorganic (Aqueous) Electrolytes 44
2.2.3.2 Organic (Non-aqueous) Electrolytes..45
2.3 Characterization Techniques for EC devices 47
2.3.1 Nano-structures Characterization...47
2.3.1.1 Specific Surface Area 47
2.3.1.2 Pore Size and Distribution 49
2.3.2 Electrochemical Characterization 51
2.3.2.1 Cyclic Voltammetry...51
2.3.2.2 Constant Current Charge/Discharge 53
2.3.2.3 Electrochemical Impendence Spectroscopy and Circuit Modeling 55
2.3.3 Thermal Characterization..59
2.3.4 Test Cell Configuration...62
Chapter 3. Fabrication of Nano-Carbon Electrodes 65
3.1 Fabrication and Characterization of SWCNT Electrodes 65
3.1.1 Experimental 66
3.1.1.1. Preparation for Functionalized SWCNT Suspension 66
3.1.1.2. Fabrication of SWCNT Electrodes using EPD and Measurements 67
3.1.2 Results and Discussion 69
3.1.2.1 Influence of pH Values of the Suspension on EPD 69
3.1.2.2 Electrochemical Characterization of SWCNT Electrodes 74
3.1.2.3 Electrochemical Impedance and Equivalent Circuit Modeling 79
3.1.3 Summary 83
3.2 Fabrication of Activated Carbon Electrodes 85
3.3 Fabrication of Graphene and SWCNT Electrodes using Vacuum Filtration 86
Chapter 4. Development of an Equivalent Circuit Model...88
4.1 Introduction 88
4.2 Circuit Model Development..88
4.2.1 Electrochemical Double Layer Capacitance at the Double-layer Interface 91
4.2.2 Resistance at the Double-layer Interface Region..95

4.2.3 Bulk Solution Impedance 97

4.3 Experimental 98

4.4 Results and Discussion 99

4.4.1 Electrochemical Characteristics 99

4.4.2 Simulations with an Equivalent Circuit and Potential Dependency 106

4.5 Summary 115

Chapter 5. Characterization of Electrochemical and Thermal Behaviors with Porous Caron Electrodes....................116

5.1 Introduction 116

5.2 Experimental 117

5.3 Results and Discussion 119

5.3.1 Structural Properties of Electrodes 119

5.3.2 Electrochemical Characterization 124

5.3.3 Thermal Characterization 131

5.4 Summary 145

Chapter 6. Characterization of Thermal Behaviors with Electrolytes 147

6.1 Introduction 147

6.2 Experimental 148

6.3 Results and Discussion 149

6.3.1 Characterization of Thermal Behaviors 149

6.3.2 EIS Simulations and Temperature-dependent Reactions 158

6.4 Summary 164

Chapter 7. Conclusions and Future Work 166

7.1 Conclusions 166

7.2 Future Work 170

References 172

List of Figures

Figure 1.1 Ragone plot for electrochemical energy storage devices: fuel cells, batteries, conventional capacitors and electrochemical capacitors [14] 2
Figure 2.1 Classification of common types of capacitors 12
Figure 2.2 Schematic diagram of a charged EDLC 13
Figure 2.3 Schematic of different types of capacitive charge storage mechanisms 16
Figure 2.4 Schematic of electrode reactions 20
Figure 2.5 The effects of a potential change on the free energies of activation for electrode reactions 21
Figure 2.6 Illustration of CNTs: (a) representation of a SWCNT (left) and a MWCNT (right) [65]; and (b) schematic diagram of CNT spaces available for electrolyte ions storage [66]........ 32
Figure 2.7 Comparison of carbon materials for use as EC electrodes: (a) activated carbon, (b) carbon nanotube, (c) graphene [90] 36
Figure 2.8 Description of cast-coating using slurry 39
Figure 2.9 Schematic diagram of electrophoresis [106] 40
Figure 2.10 Schematic of the preparation of electrodes using vacuum filtration 43
Figure 2.11 Schematic explanation of a cyclic voltammogram (b) in the absence of a redox process and (c) with an active redox reaction 53
Figure 2.12 Typical CCD test results for ideal EDLCs 54
Figure 2.13 IR drop in CCD measurement due to an equivalent series resistance (ESR) 55
Figure 2.14 EIS data samples: (a) Nyquist plot of a typical EDLC. (b) example of equivalent circuit model for a pure EDLC. (c) example of equivalent circuit model for an EDLC that includes a pseudo-capacitance (Cp) 56
Figure 2.15 Capacitance and resistance frequency dependence of BCAP0010 for different temperatures [143] 61
Figure 2.16 Schematic diagram of EC test cells: (a) two-electrode cell and (b) three-electrode cell 63
Figure 3.1 Images of functionalization processing for SWCNTs 67
Figure 3.2 Schematic diagram of EPD SWCNT coating process 68

Figure 3.3 Photographs of SWCNT suspensions at pH4, 6 and 10, respectively 70
Figure 3.4 Schematic explanations for highly charged SWCNT by increasing pH values 71
Figure 3.5 FE-SEM images of SWCNT electrodes processed from suspensions with different pH values and with the EPD period of (a) 3min, (b) 30min, respectively. (c) The qualitative illustration of the deposition mechanisms with varying pH values 72
Figure 3.6 Cyclic voltammograms of SWCNT electrodes, in 1M H_2SO_4 with various pH values (a) pH4, (b) pH7 and (c) pH 10 75
Figure 3.7 The dependence of the capacitance (evaluated by CV) on the EPD processing times for varying pH values 76
Figure 3.8 Specific capacitance (F/g) and BET surface area of SWCNT electrodes fabricated with different pH values 78
Figure 3.9 Pore size distributions of SWCNT electrodes fabricated with different pH values: (a) Pore area and (b) Pore volume 79
Figure 3.10 (a) Nyquist plots for the SWCNT electrodes with different pH values at EPD processing times, 3 min., and (b) Enlarged sections of the Nyquist plots at high frequency. (c) Nyquist plots for the SWCNT electrodes with different pH values at EPD processing time of 30 min. (d) Enlarged sections of the Nyquist plots at high frequency for (c) 80
Figure 3.11 Correlation between Nyquist plots with different pH values: (a) pH 4, (b) pH 7, (c) pH 10 82
Figure 3.12 Schematic of vacuum filtration deposition process 86
Figure 4.1 Schematics of an electrochemical double layer and the electrode/electrolyte interfaces model 90
Figure 4.2 Equivalent circuit modeling of (a) interfacial processes at doulbe-layer, (b) consideration of bulk processes and (c) the completed circuit 94
Figure 4.3 Cyclic voltammetry for organic and aqueous electrolytes at the scan rate 20 mV/s... 99
Figure 4.4 Cyclic voltammery at various scan rates, 5, 10 and 40 mV/s: (a) organic (1 M Et_4NBF_4/PC) electrolyte up to 2.4 V, (b) aqueous (1 M H_2SO_4) electrolyte up to 0.8 V, respectively 100

Figure 4.5 Discharging processes at the constant current (30 C-rate) and the determination of ohmic drops with different charging voltages for (a) Organic electrolyte,up to 1.2 vs. 2.4 V and (b) Aqueous electrolyte, up to 0.2 vs. 0.6 V, respectively 102

Figure 4.6 Nyquist plots for cells in 1 M H_2SO_4 and 1 M Et_4NBF_4/PC electrolytes, respectively. Measurement was performed at the applied voltage of 5 mV, with the frequency range from 10 mHz to 100 kHz 104

Figure 4.7 Bode polt of (a) real impedance and (b) real capacitance vs. frequency for two electrolytes 105

Figure 4.8 Simulated impedances, Zreal and Zimag, with measured Nyquist plots for aqueous and organic electrolytes 107

Figure 4.9 Measured and simulated impedances for the different applied voltage on (a) organic electrolyte, (b) aqueous electrolyte, respectively. The insert is an enlarged view at high frequencies 109

Figure 4.10 Measured and simulated differential capacitances and resistances depending on the applied voltages for (a) organic electrolyte, (b) aqueous electrolyte, respectively.............. 110

Figure 4.11 Correlation between EIS modeling and CCD measurement; ESR difference from the applied voltages for (a) organic electrolyte, (b) aqeuous electrolyte, respectively.............. 113

Figure 5.1 FE-SEM images of the electrodes: (a) AC, showing schematics of 3D randomly dispersed AC structures; (b) graphene, showing 2D agglomerated graphene sheets, including a TEM image of graphene layers; and (c) SWCNT, showing a 1D ramdomly dispersed SWCNT network 120

Figure 5.2 Graphene results: (a) SEM image of a typical graphene nanoplatelet; (b) AFM ichnography image; and (c) cross-section analysis of overlayered graphene nanoplatelets with A-D indicating the positions on the dotted line where the tip scanned 120

Figure 5.3 Nitrogen adsoprtion isotherms for the carbon electrodes: (a) AC; (b) graphene; and (c) SWCNT 121

Figure 5.4 Pore volume distributions: (a) within meso-/macropore ranges of 2nm and above, based on the BJH method; and (b) within micropore range under 2nm, based on the HK method.. 122

Figure 5.5 Cyclic voltammetry curves for the AC, graphene and SWCNT electrodes in an organic 1M Et_4NBF_4/PC electrolyte, produced with a scan rate of 20 mV/s 125

Figure 5.6 Cylic voltammetry curves: (a) for AC, (b) graphene, and (c) SWCNT electrodes in 1M Et_4NBF_4/PC electrolyte at different scan rates.. 126

Figure 5.7 (a) Nyquist plots of AC, graphene and SWCNT electrodes in 1M Et_4NBF_4/PC with (b) the enlarged image 128

Figure 5.8 Bode plots for AC, graphene and SWCNT electrodes in 1M Et_4NBF_4/PC 129

Figure 5.9 Cyclic voltammetry at a scan rate of 20 mV/s for (a) activated carbon, (b) graphene and (c) SWCNT electrodes at operating temperatures from -30 to 60 ℃ 131

Figure 5.10 Discharging process at constant current (a rat of 30 C) and ohmic drop (ΔV) for (a) activated carbon, (b) graphene, and (c) SWCNT electrodes in 1M Et_4NBF_4/PC electrolyte at operating temperatures ranging from -30 ℃ to 60 ℃.. 132

Figure 5.11 Plots for the activated carbon, graphene, and SWCNT electrodes based on the CCD cureves: (a) comparison of specific capacitance levels; (b) the differences in internal resistance with temperatures.. 134

Figure 5.12 Ragone chart with specific power / energy density for (a) activated carbon, (b) graphene and (c) SWCNT-based EDLCs 135

Figure 5.13 Bode plots of real capacitance for (a) activated carbon, (b) graphene and (c) SWCNT electrodes 137

Figure 5.14 Bode plots of real impedance for (a) activated carbon, (b) graphene and (c) SWCNT electrodes 139

Figure 5.15 Plots of the measurement results for the activated carbon, graphene and SWCNT electrodes with respect to (a) capacitance (C_{real}) retention and (b) comparative Zreal values (measured at 10 mHz from Bode plots)... 140

Figure 5.16 Schematic diagrams of ion adsorption and the interactions associated with micro-pores and meso-/macro-pores at varied temperatures... 141

Figure 5.17 Arrhenius plots of the temperature dependency of kinetic and diffusion resistances in (a) activated carbon, (b) graphene and (c) SWCNT electrodes........................... 144

Figure 6.1 Cyclic voltammetry of (a) 3M H_2SO_4 and (b) 1M Et_4NBF_4/PC electrolyte at operating temperature from -30 to 60 ℃ at a scan rate of 20 mV/s , respectively.................... 150

Figure 6.2 Discharging process at constant current (30 C rate) and ohmic drop (ΔV) for (a) 3M H_2SO_4 and (b) 1M Et_4NBF_4/PC electrolyte at various temperatures, respectively 151

Figure 6.3 Capacitance retention and internal resistance (ESR) deviation for (a) 3M H_2SO_4 and (b) 1M Et_4NBF_4/PC electrolyte depending on temperatures, respectively 153

Figure 6.4 Ragone chart with specific power (W/kg)/energy density (Wh/kg) for 3M H_2SO_4 and 1M Et_4NBF_4/PC electrolytes operating from V_{min} to V_{max} at different temperatures 154

Figure 6.5 Nyquist plots for cells in (a) 3M H_2SO_4 and (b) 1M Et_4NBF_4/PC electrolytes, including enlarged images at right side 155

Figure 6.6 Bode plots of real capacitance for (a) 3M H_2SO_4 and (b) 1M Et_4NBF_4/PC electrolytes 156

Figure 6.7 Bode plots of real impedance for (a) 3M H_2SO_4 and (b) 1M Et_4NBF_4/PC electrolytes 157

Figure 6.8 Correlation between the simulated total impedance at 10 mHz and the measured ESR from CCD measurement in log scale 161

Figure 6.9 An Arrhenius plot of the temperature dependency of kinetic and diffusion resistances in (a) H_2SO_4 and (b) Et_4NBF_4/PC electrolyte 163

List of Tables

Table 1.1 Comparison of conventional capacitor, electrochemical capacitor and battery 3

Table 2.1 Examples of CNT electrodes using different deposition method 34

Table 2.2 Properties of aqueous, organic and ion liquid electrolytes 46

Table 2.3 Circuit elements used in the electric circuit models 56

Table 3.1 BET surface areas, pore volumes and average pore diameters of SWCNT electrodes processed with different pH conditions 77

Table 3.2 Proposed equivalent circuit models for SWCNT electrodes fabricated from different pH values.. 81

Table 3.3 Equivalent circuit parameters (C_P, R_S & R_F) obtained from the modeling results 83

Table 3.4 Typical specifications for a single electrode made of activated carbon 85

Table 3.5 Typical specifications of a single electrodes made of graphene and SWCNT 87

Table 4.1 Circuit elements used in the model and mathmatical equation for each impedance 92

Table 4.2 Measured values of ohmic drop and ESR from the charging/discharging cycle at the constant current (30 C-rate) for two electrolytes 103

Table 4.3 Equivalent circuit parameters (Capacitance and Resistance) obtained from the simulation results with two electrolytes... 108

Table 4.4 Calculated parameters (Capacitance and Resistance) obtained from the simulation results with different applied voltages on aqueous electrolyte (1M H_2SO_4) 112

Table 4.5 Calculated parameters (Capacitance and Resistance) obtained from the simulation results with different applied voltages on organic electrolyte (1M Et_4NBF_4/PC)...................... 112

Table 5.1 Specific BET surface areas, external areas, pore diameters and pore volumes of the AC, graphene and SWCNT electrodes 123

Table 5.2 Variation of the specific capacitance (F/g) calculated from cyclic voltammetry measurents with 1M Et_4NBF_4/PC was the electrolyte and with different scan rates.................. 127

Table 5.3 Values measured for C_{real} (F/g) from Bode plots at 0.1 Hz for activated carbon, graphene, and SWCNT electrodes.. 137

Table 6.1 Simulated specific capacitances (F/g) from the circuit model vs. measured ones from Bode plots at 10 mHz for (a) 3M H_2SO_4 and (b) 1M Et_4NBF_4/PC with different temperatures 158

Table 6.2 Simulated resistances from the circuit model for (a) 3M H_2SO_4 and (b) 1M Et_4NBF_4/PC with different temperatures 160

Table 7.1 Structural and electrical properties of porous carbon electrodes, and their electrochemical and thermal behaviors 169

List of Abbreviations

EC	Electrochemical capacitor
ELDC	Electrochemical double-layer capacitor
CNT	Carbon nanotube
SWCNT	Single-walled carbon nanotube
AC	Activated carbon
CV	Cyclic voltammetry
CCD	Constant current charge-discharge
EIS	Electrochemical impedance spectroscopy
PSD	Pore size distribution
EPD	Electrophoretic deposition
BET	Braunauer, Emmett and Teller method
FE-SEM	Field emission scanning electron microscopy
AFM	Atomic force microscopy
SSA	Specific surface area
BJH	Barrett, Joyner & Halenda method
HK	Horvath−Kawazoe method
ESR	Equivalent series resistance
G	Gibbs free energy
CPE	Constant phase element
W	Warburg element
IHP	Inner Helmholtz plane
OHP	Outer Helmholtz plane
Et_4NBF_4	Tetraethylammonium tetrafluoroborate
PC	Propylene carbonate

Chapter 1 Introduction

1.1 Energy Storage Systems

Today, electric energy use grows dramatically due to rapidly increasing demand in emerging economies and in human life. However, the finite amounts of natural resources, the high cost of fossil fuel and environmental awareness are driving efforts to find alternative solutions to the world's energy needs. Eventually, all sustainable energy systems will have to be based on limited use of fossil fuels and greater use of renewable energy. On the other hand, the production of electricity is highly centralized, and often occurs a long distance away from end consumers. This delocalized electricity production and the difficulty of stabilizing the power network have caused a supply-demand imbalance [1]. Accordingly, it is extremely important to generate, transmit, convert and store energy in manageable and smart way. For instance, electrical energy storage (EES) is a systematic approach currently under development, and it enables electricity to be produced from intermittent energy sources and be stored for utilization when it is needed. In fact, the storage of electric energy has recently become a necessity owing to the emergence of applications such as hybrid electric vehicles and many other types of portable electrical devices. The tremendous growth of electric or hybrid electric vehicles has also promoted the urgent and increasing demand for advanced energy storage technologies [2-7]. Therefore, significant advancement in enabling efficient and sustainable energy use requires an urgent development of storage methods to meet growing energy demands and to balance supply and consumption while avoiding resource depletion and long-term damage to the environment.

Large-scale research efforts have been made in various locations around the world to develop a variety of electrical energy storage devices. As a result, many possible techniques have been introduced for energy storage systems and devices, such as flywheels[8], fuel cells [9], batteries [10, 11], electrochemical capacitors and conventional capacitors [12, 13]. Among these devices, batteries, electrochemical capacitors (ECs, called electrochemical double-layer capacitors, or ultra-capacitors) and conventional capacitors are the three main electrochemical energy storage technologies thanks to their practical power/energy capabilities, portability with light weight, high efficiency and low cost. Each however offers different characteristics and applications with inherent advantages, including in performance, cost and reliability. To better understand their differences, a Ragone plot can be drawn to illustrate their respective performances. The Ragone plot is often used to graph a device's characteristic power density (W/kg) in relation to its energy density (Wh/kg) as shown in Figure 1.1. The diagonal lines demonstrate the energy charge/discharge times.

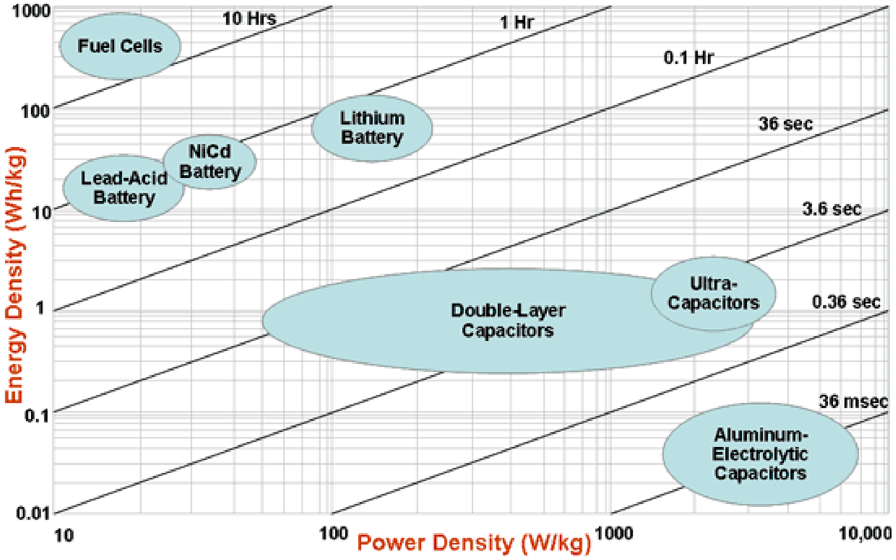

Figure 1.1 Ragone plot for electrochemical energy storage devices: fuel cells, batteries, conventional capacitors and electrochemical capacitors [14]

From a general point of view, batteries, for example, Li-batteries and lead-acid batteries, can have high energy densities ranging from 10 to 100 Wh/kg, but their power densities are relatively low, under 0.01 kW/kg. Because of the low power density, batteries are not suitable for high power demand applications, such as regenerative braking or load leveling systems. Additionally, most batteries need a long charging time (0.3~3 hrs) and have a limited lifetime of up to a thousand cycles. On the other hand, ECs can deliver a higher power density (15 kW/kg) than batteries and possess a larger stored energy than conventional capacitors. They exhibit fast charging and discharging with extremely high cycle stability (100,000 cycles). Table 1.1 shows a detailed comparison of the properties and performance of batteries, conventional capacitors and electrochemical capacitors [15], which confirms that ECs are particularly suitable for applications where high power is needed for a few seconds. Otherwise, they can act as a complement to batteries in applications in which high energy and high power delivery have to be achieved. However, ECs are clearly limited by the energy density (below 10 Wh/kg), which prevents them from becoming a primary energy source in a variety of applications.

Table 1.1 Comparison of conventional capacitor, electrochemical capacitor and battery

Factors	Batteries	Conventional Capacitors	Electrochemical Capacitors
Specific Power (W/kg)	50 ~ 200	10,000	1000 ~ 2000
Specific Energy (Wh/kg)	20 ~ 100	< 0.1	1 ~ 10
Charge Time	0.3 ~ 3 h	10^{-6} ~ 10^{-3} s	1 ~ 30 s
Discharge Time	1 ~ 5 h	10^{-6} ~ 10^{-3} s	1 ~ 30 s
Cycle Life (cycle)	500 ~ 2000	> 500,000	> 100,000
Charge/Discharge Efficiency (%)	70 ~ 85 %	~100 %	90 ~ 95 %

To resolve this issue related to EC’s limitations, many researchers have committed to improving the performance of ECs including increasing energy and power densities. The advancements made in nano-material research and nano-scaled structures, including carbon-based materials, nanowires, metal oxides and polymer composites, are utilized to pursue the device-development trend, leading to improved performances. Nano carbon materials or nano-structured materials are novel energy materials since their reduced dimensions and the uniqueness of surface properties are able to provide a high volume fraction of interfaces which favour increased reaction rates. For those developments, it is necessary to gain better understanding about nano carbon electrodes/electrolytes interfaces through characterizing all EC’s component properties and verifying their performance in advanced energy storage applications. Also of interest is to reduce the manufacturing costs and to develop the optimized component that will satisfy the full range requirements for various applications. In this regard, exploring carbon materials to develop novel solutions for advanced ECs is accompanied by a systematic approach involving fabrication methods, characterization and reliable evaluation for their performance. Furthermore, it is important to note that the characteristic power performance and acceptable reliability of existing EC devices should be preserved to maintain their function, rather than just simply developing alternatives to the average battery.

1.2 Electrochemical Capacitors (ECs) and their Applications, Challenges

Electrochemical capacitors are energy devices that store and release electric energy through nanoscopic ion separation at the electrochemical interface between an electrode and a liquid electrolyte [16, 17]. In recent years, ECs have attracted increasing attention, mainly due to their high power density, long life-cycle and ability to bridge the power/energy gap between batteries/fuel cells (which have high energy density) and conventional capacitors (which have high power density) as described in Figure 1.1. In comparison to fundamental operating mechanisms, batteries and fuel cells produce their stored energy through chemical reactions, whereas ECs generate by utilizing electrostatic separation between electrolyte ions and high-surface area electrodes [17, 18]. Unlike batteries or fuel cells, negligible chemical charge transfer reactions and phase changes are involved in charging and discharging, so that the charge-discharge process will not necessarily be limited by chemical kinetics in the electrode. For that reason, the charging and discharging rates are much faster than the electrochemical redox reactions inside batteries, eventually leading to higher power density in ECs. They have been already shown with a nearly unlimited cycle-ability, and with a high cycle efficiency. Moreover, ECs can not only function effectively at extremely high and low temperatures (typical operating temperature ranges from -40 to 70 ℃), but also contain no hazardous or toxic materials, and their waste materials are easily disposed of, compared to batteries.

Thanks to these merits in EC devices, the US Department of Energy (DoE) recognized the promising aspects of ECs in the early nineties for use in hybrid electric vehicles (HEV), and recommended the importance of EC research and the development of energy storage devices in future technologies [19]. It was also suggested that EC can play an important role in complementing batteries or fuel cells in their energy storage functions, by providing back-up power supplies and allowing the recovery of brake energy to improve energy efficiency. In addition, small devices are widely used for power buffer applications or for memory back-up in toys, cameras, video recorders, mobile phones and so forth [20-22].

However, several major problems have restricted the development of ECs to be the primary power source in various applications. In particular, their energy density is not high enough, and more effective design of ECs is required to optimize their structures and component materials for the improvement of a device’s reliabilities. Moreover, the practical issues in engineering an EC include manufacturing cost-effective energy storage systems at large scales.

Three main challenges for developing ECs are summarized as:

- Low energy density

  As discussed before, ECs suffer from limited energy density (up to about 5 Wh/kg) compared to batteries (normally 50 Wh/kg). For instance, commercially available ECs can provide energy densities of only 3 - 4 Wh/kg, which limits the use of ECs to a few seconds, typically within the range of 1 - 30 s.

- High self-discharge (Internal resistance)

  Another challenge that needs to be met for ECs to fulfill their promise is in improving their tendency to self-discharge. In practical use of EC devices, there is a decline in voltage on an open circuit due to an internal resistance. Self-discharge is intrinsic to all electrochemical energy storage systems, including batteries and capacitors. However, it occurs at higher rate for ECs because ECs have no mechanism to thermodynamically and kinetically stabilize voltage unlike batteries. As a result, the voltage of ECs can be easily disturbed by some depolarizing process from the internal resistance. This self-discharge characteristic tends to more detrimental in ECs than batteries, and leads to lower power and energy density. Therefore, the self-discharge behavior of ECs is an unreliability factor in energy storage and need to be solved.

- High cost

  The costs of raw materials continue to be major challenges for EC commercialization. The main cost of an EC arises from its electrode materials, and when EC use organic electrolytes, their cost is far from negligible. Furthermore, the manufacturing cost is also determined by fabrication methods for real products. Therefore, the development of manufacturing is required to design not only optimized EC's structure but also scalable, cost-effective fabrication methods.

In order to overcome these challenges, one of most common approaches is the development of new nano-structured carbon materials for EC electrodes. Carbon-based electrodes, such as activated carbon, carbon nanotube and graphene, are desirable because of their low cost under scalable mass production, high surface area, good corrosion resistance and high thermal stability. Currently, the most popular material is activated carbon, which has high surface area for energy charge storage as well as low cost when used in the fabrication of ECs. However, in spite of their large specific surface areas, the charges physically stored on the carbon particles in porous electrode layers are limited by their poor wettability to electrolytic ions (i.e. electrolytic ion's accessibility). The study described in the literature [23] suggests the importance of the relationship between electrolytic ion's size and the pore size of carbon materials. Higher performance of nano-structured electrodes may be obtainable if carbon electrodes can be assembled in a manner that enables optimization of their surface area so that it is properly accessible to the electrolytic ions. The first progress in this area was to formulate porous carbon electrodes with an optimal pore structure through various carbon manipulations [24-28]. Alternatively, the fabrication method of electrodes may also affect their porosity, which influences how easily the electrolyte ions can move into and out of the electrode during the charge/discharge process [29, 30]. More research is still needed to develop optimized electrode architectures, in order to facilitate ECs as a desirable energy storage technology for many applications. Meanwhile, the selection of appropriate electrolytes is fundamentally important in achieving the desired power/energy densities because these are strongly relevant to a cell's operating voltage, its internal resistance and thermal reliabilities. These properties principally depend on an electrolyte's properties, such as its breakdown voltage and conductivity. Therefore, it is essential to find strategies for selecting ideal electrolytes with respect to their stability in operation voltages, temperatures and electrical conductivity.

1.3 Research Objectives

The research goals are to establish qualitative understanding of charge mechanisms in nano-structured ECs by characterizing each component's electrochemical and thermal behavior, and to develop a technique for fabricating advanced EC devices with the desirable performance in a variety of applications. This work has been designed to analyze both carbon-based electrodes and electrolytes' properties. Both can be engineered to realize the optimized EC structures for reliable and cost-effective energy storage systems, which require an optimized combination by taking full advantage of each component’s characteristics. Furthermore, electric-circuit modeling of carbon-based EC devices should be developed and simulated with experimental impedance data. This empirical modeling is useful in providing sufficient information on physical processes at nano-structured electrode/electrolyte interfaces. Eventually, this modeling will be useful for the optimum utilization of a nano-structured carbon electrode with different electrolytes, and help in the simulation of fabricated devices without experimental data for the design stage.

This research is a part of a joint project with General Motors Co., investigating fundamental properties of ECs and their component optimization for high-energy density applications in hybrid electric vehicles (HEVs) or electric vehicles (EVs), and characterizing the existing EC devices for cost-effective hybrid energy storage system (HESS).

The first objective of this research is to identify critical properties of nano-structured electrodes and characterize their performance. More specifically, this approach is focused on characterizing fundamental properties of three representative carbon-based electrodes, activated carbon, carbon nanotubes and graphene, with simultaneous tailored parameters of their pore structure and specific surface area. This work provides not only fundamental characteristics of nano-structured carbon electrodes but also the crucial parameters to design the suitable electrode’s structures for enhanced electrochemical/thermal behavior in practical EC’s applications. In particular, this research is intended to evaluate each element’s performances over a range of practical parameters for the usage of EC devices. The quantitative difference in a cell’s performance, such as its capacitance retention, the degradation of energy/power densities, the variation of internal resistance (or self-discharge) and the temperature dependency, are taken into account for practical use in EC devices. At the same time, it is expected to fabricate advanced nano-structured electrodes, and eventually, to lead to the development of new fabrication techniques with cost-efficient production.

As the second objective, different electrolytes, such as aqueous and organic ones, are to be characterized to investigate the effect of their electrochemical and thermal properties on an EC device's performances. The potential window of electrolytes, their conductivity, ion size, thermal reliability and potential dependency are considered as critical characteristic parameters and compared.

The third objective is to develop an equivalent electrical circuit model based on the theoretical description of double-layer interfaces, which can be valuable in determining the critical electrochemical reactions at the interface between electrodes and electrolytes. The effect of each engineered component, including electrodes and electrolytes, on EC's performance can be simulated from equivalent circuit models by means of electrochemical impedance spectroscopy (EIS) analysis. This simulation with the proposed circuit model is particularly aimed to provide meaningful information for the electrode's kinetics (ion adsorption, charge transfer) and electrolytic ion's transportation (diffusion) under a variety of real operating conditions.

Chapter 2 Background and Literature Review

2.1 Principles of Electrochemical Capacitors

A wide variety of capacitors types are currently available, which can be classified according to their usage of specific dielectric materials constituents or according to their physical state, as shown in Figure 2.1. Each type has specific characteristics and applications, ranging from small-sized capacitors for electronics, to large-powered capacitors for high-voltage systems, to high-energy electrochemical capacitors (ECs). ECs are a special kind of capacitor that can store and release electrical energy based on the electrostatic interactions between the ions in the electrolyte and the high-surface area electrodes. This interaction occurs near the surfaces of the electrodes in what are called electrochemical double-layer capacitors (EDLCs), or supercapacitors. Although these capacitors are governed by the same basic principles as the conventional capacitors, they incorporate electrodes that have a greater effective surface area along with the microscopic properties of dielectrics at the molecular level (thinner thickness of the layers at the nano-scale), leading to a significant increase in capacitance. However, for many applications, EC capacitances are still not large enough to operate as independent energy storage devices, resulting in a low energy density. To resolve this issue of insufficient capacitance, another class of capacitors, called pseudo-capacitors, has been developed. The principles governing electrochemical capacitors are based primarily on two types of capacitive behavior: (1) one associated with EDLCs and (2) another associated with pseudo-capacitance.

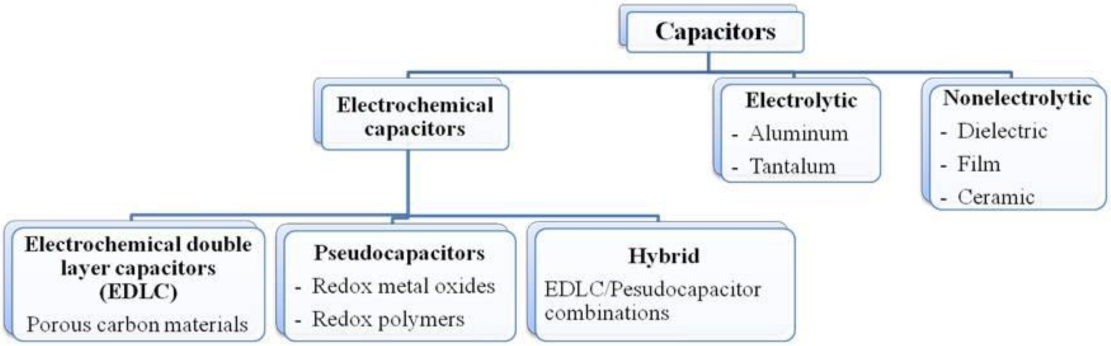

Figure 2.1 Classification of common types of capacitors

2.1.1 Electrochemical Double-Layer Capacitor (EDLC)

The concept of the EDLC was first described and modeled by von Helmholtz in the 19th century. He stated that two layers of opposite charges form at the electrode/electrolyte interface and are separated by an atomic distance [31]. In principle, the positively or negatively charged surface is balanced by an accumulation of counter-ions from the solution, which form a double-layer of positive-negative charges that ideally remains electrostatic, with no electron transfer between the layers throughout the process. As illustrated in Figure 2.2, according to his model, the capacitance is dependent on the specific surface area (SSA) of the electrodes, the type of electrolyte (dielectric constants), and the effective thickness of the double layer, which is referred to as the Helmholtz layer. The estimated capacitance of an EDLC, or Helmholtz layer capacitance, is determined according to the following:

$$C_H = \frac{\varepsilon_r \varepsilon_0 A}{d} \tag{1}$$

where C is the capacitance of the EDLC in the Helmholtz model, ε_r is the relative dielectric constant of the electrolyte, ε_0 is the dielectric constant of the vacuum, d is the effective thickness of the double layer, and A is the SSA of the electrode.

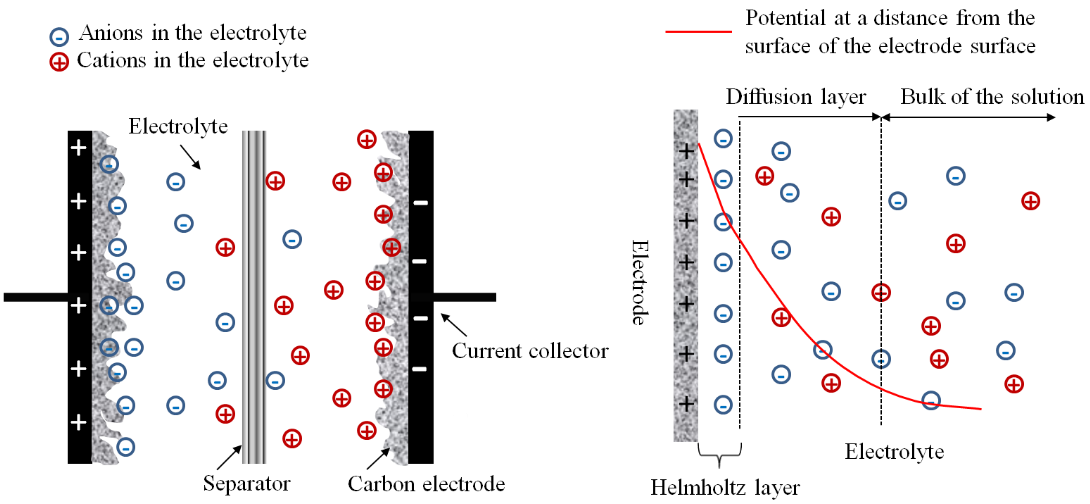

Figure 2.2 Schematic diagram of a charged EDLC

At the same time, the accumulation of the electrolyte ions also forms a diffusion layer in which the ions (anions or cations) are distributed according to the interfacial potential on the electrolyte side, and tend to diffuse into the liquid phase until the counter potential set up by their departure restricts this tendency. The Helmholtz model fails to provide an adequate explanation of this feature of the diffuse layer, and this concept was expanded upon by Gouy and Chapman[32], Stern [33] then combined it with the Helmholtz model. According to this theory, the ions on the solution side of the EDLC are subjected to the effects of thermal fluctuation [34] rather than remaining static in a compact layer, as in the Helmholtz model. The capacitance contribution from the net charges in the diffusion layer can be considered an additional capacitor in series and that is governed by the combined application of Boltzmann's energy distribution equation [35] and Poisson's equation [36]. The capacitance of the diffuse layer can therefore be defined as

$$\mathrm{C_{diff}} = \left(\frac{\mathrm{z^2F^2c\varepsilon}}{2\pi\mathrm{RT}}\right)^{\frac{1}{2}} \cosh\frac{\mathrm{zF(E-E^0)}}{2\mathrm{RT}} \tag{2}$$

where C_{diff} is the capacitance of the diffusion layer, z is the charge of the electrolyte ion, F is the Faraday constant, c is the concentration of the electrolyte, E is the potential, E^0 is the electrode potential at a zero charge, R is the molar gas constant, and T is the temperature. After Gouy and Chapman proposed their theory, Stern combined the Helmholtz model with the refined Gouy-Chapman model and recognized that two regions of ion distribution exist at the electrode/electrolyte interface: the inner region called the compact, or Helmholtz layer, which is related to an adsorption process, and the region beyond this inner layer, which is related to a diffusion process. Therefore, the overall EDLC capacitance, C_{dl} is actually a series of two capacitances: C_H, the Helmholtz layer capacitance, and C_{diff}, the diffusion layer capacitance. The total capacitance can be expressed as follows:

$$\frac{1}{\mathrm{C_{dl}}} = \frac{1}{\mathrm{C_H}} + \frac{1}{\mathrm{C_{diff}}} \tag{3}$$

As can be seen from Eq. (1) to (3), the C_{dl} is determined mainly based on the two components, the electrode and the electrolyte, whose properties are important for determining the electrochemical behavior of an EDLC and its capacitance. To achieve a large capacitance, EDLCs have been developed based on the adaptation of high SSA carbon powder or porous carbon materials according to Eq. (1). However, when porous carbon electrodes are employed, EDLC behavior can become more complex because ion transportation can be drastically affected by a number of parameters; the mass transfer path onto an electrode, the space constraint inside the pore, the electric field across the electrode, the nature of the electrolyte ions, the ohmic resistance of the electrolyte, and the wetting behavior of the electrolyte with respect to pore surface. The utilization of suitable electrode materials adapted for an appropriate type of electrolyte solution is therefore considered to be a critical factor governing the direction of EDLC technological development. [17]. Effective control of pore structure (i.e., ion accessibility) corresponds directly to good EDLC performance in terms of both the rate of power delivery and energy storage capacity. At the same time, EDLC development can also be achieved through an enhanced understanding of the electrochemical behavior at the interface between the porous surface of the electrode and the electrolytic ions.

2.1.2 Pseudo-Capacitors

The energy storage system of a pseudo-capacitor is much more complex than that of an EDLC. The distinction begins at the electrode surface, where a completely different charge-storage mechanism applies, a simple illustration of which is provided in Figure 2.3.

The primary difference between an EDLC and a pseudo-capacitor is that the EDLC utilizes a non-Faradaic process (electrostatically) to store energy, while the pseudo-capacitor adheres to the conventional Faradaic process that involves fast and reversible redox reactions between the electrolyte and electro-active species such as conducting polymers (e.g. polypyrrole, polyailine) [37, 38] and metal oxides (e.g. MnO_2, RuO_2) [39, 40]. The redox reactions correspond in a formal general way to an electron transfer process between an oxidized species, O_X (e.g. H+, Li+ or metal ion redox regent) and a reduced species, Red (e.g. adsorbed H, a metal ion in a reduced state):

$$O_X + ne \Leftrightarrow \mathrm{Red} \tag{4}$$

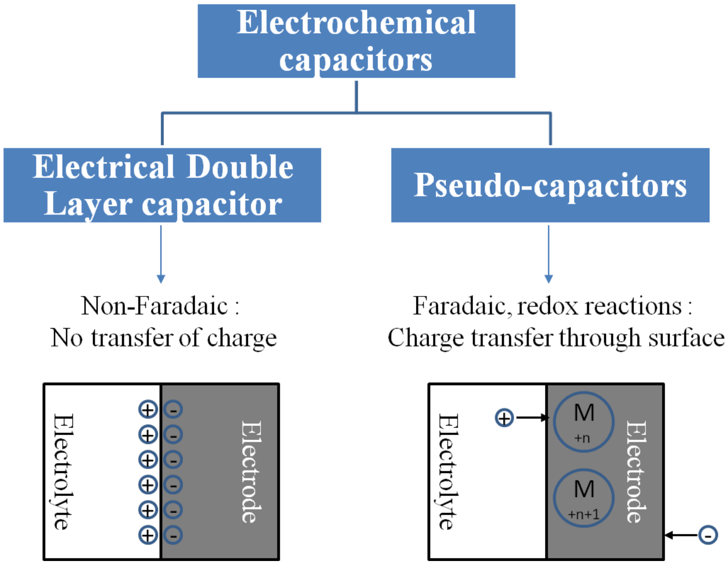

Figure 2.3 Schematic of different types of capacitive charge storage mechanisms

In principle, pseudo-capacitance is governed by thermodynamics according to which the extent of a reaction (q) that stems from Faradaic charge-transfer processes is a continuous function of the applied potential (V), so that a derivative, dq/dV, arises, which is equivalent to a capacitance. The capacitance can thus be described as follows:

$$C = \frac{\partial(\Delta q)}{\partial(\Delta V)} \tag{5}$$

Pseudo-capacitance is similar to an EDLC process, in that the stored charge is proportional to the applied potential. However, it should be noted that such a process is a Faradaic reaction involving chemical changes of the state of the reactant species that results from the electron transfer between O_X and Red. These Faradaic processes can produce a remarkable enhancement of the capacitance values and energy density. However, pseudo-capacitors exhibit somewhat lower power density than EDCLs because Faradaic processes are normally slower than non-Faradaic ones. It has also been observed that, like batteries, capacitors often lack stability during cycling [41].

2.1.3 Electrochemistry in ECs

This section explains from a thermodynamic perspective and kinetic treatment in the double-layer interface, which enables a detailed illustration of the structure of the double layer along with their related implications for electrode kinetics. This background is important for interpreting the thermal behavior of ECs as well as the interfacial processes (e.g., charge transfer, adsorption, and diffusion reactions) across the double-layer.

2.1.3.1 Thermodynamic Considerations

Double-layer charging is an interfacial phenomenon, and information about double-layer structure can be obtained by following the approach employed by Gibbs. The change in free energy in a region between a pure electrode and a pure electrolyte phase can be usefully represented by Gibbs free energy, G, and a reference system (indicated with a superscript R) where the free energy is dependent on the usual values: temperature, pressure and the molar quantities of all the components, as follows:

$$G^{R} = G(T, P, n_i) \tag{6}$$

However, an actual double-layer system (defined with a superscript, S) has a tendency to maximize the interfacial area so that the real system depends on the interfacial area A. The free energy is thus defined as the electrode, electrolyte and the interfacial region in which

$$\mathrm{G^S} = \mathrm{G(T, P, A, n_i)} \tag{7}$$

With consideration of their derivatives, and only experiments performed at a constant temperature and pressure, the overall change in energy can be expressed in the following form:

$$d\mathrm{G} = d\mathrm{G^S} - d\mathrm{G^R} = \left(\frac{\partial \mathrm{G^S}}{\partial \mathrm{A}}\right) d\mathrm{A} + \sum \left(\frac{\partial \mathrm{G^S}}{\partial \mathrm{n_i^S}}\right) d\mathrm{n_i^S} - \sum \left(\frac{\partial \mathrm{G^R}}{\partial \mathrm{n_i^R}}\right) d\mathrm{n_i^R} \tag{8}$$

Here, $\partial \mathrm{G^S}/\partial \mathrm{A}$ is the surface tension, γ, and the partial derivatives $\partial \mathrm{G^R}/\partial \mathrm{n_i^R}$ are the electrochemical potentials, μ_i of various species, i. When equilibrium applies, the electrochemical potential is constant throughout the system for any given species. The equation can then be re-expressed as

$$d\mathrm{G} = \gamma d\mathrm{A} + \sum \mu_i d\mathrm{n_i^{surface\ excess}} \tag{9}$$

After Euler's theorem and the Gibbs-Duhem equation are applied, the equation can be stated as what is called the electrocapillary equation [42]:

$$-d\gamma = \sigma^\mathrm{M} dE + \sum \Gamma_i d\mu_i \tag{10}$$

This equation expresses a relation that involves several measureable properties, such as the surface charge density, σ^M and the excess surface concentrations, $\Gamma_i = \mathrm{n_i^{surface\ excess}}/\mathrm{A}$ which account for the accumulation of ions at the double-layer interface.

Here, when Eq. 10 is differentiated at a constant electrochemical potential, the differential capacitance is defined as the following:

$$C_d = \frac{\partial \sigma^M}{\partial E} = \left(\frac{\partial^2 \gamma}{\partial E^2}\right)_{\mu_i = \text{constant}} \tag{11}$$

From this equation, it is realized that the differential capacitance can be obtained from the electrocapillary curves (surface tension plotted versus potential), which are measurable quantities. The measurement of surface tension is generally carried out based on estimations the surface tension of mercury-electrolyte interfaces. However, because of the difficulty of measuring the surface tension of a solid electrode, the differential capacitance is characterized by other techniques such as electrochemical impedance spectroscopy (EIS) measurements.

2.1.3.2 Kinetic Considerations

Kinetic theory describes the evolution of mass flow throughout a system, including both the equilibrium state and the dynamic state, whereas thermodynamics addresses only equilibrium. A kinetic picture of a system can therefore provide an accurate description of the interfacial reactions in the double-layer region. In this section, the mechanisms of electrode reactions are explained with respect to the simplest case of an electron transfer without chemical transformation. In the general case, an electrode reaction can be described as similar to that provided in Eq. (4):

$$O_X + ne \underset{kb}{\overset{kf}{\rightleftarrows}} Red \tag{12}$$

This mechanism is usually composed of the charge transfer, adsorption/desorption, and mass transport parts shown in Figure 2.4.

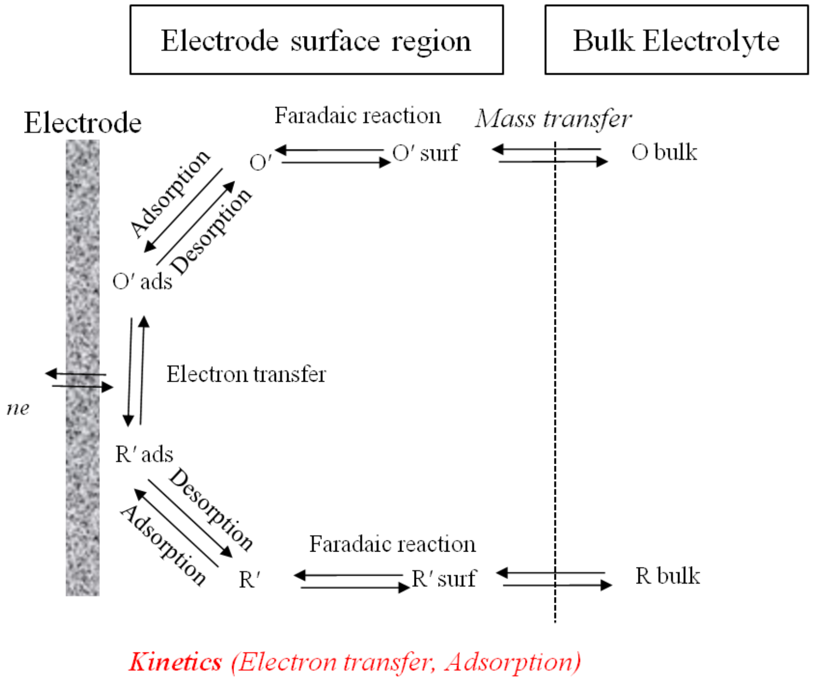

Figure 2.4 Schematic of electrode reactions

A polarized electrode can cause a current to flow via electrochemical reactions that occur at the surface of electrode, or it can change the interface status through kinetic restrictions such as adsorption or diffusion of the species to the surface of the electrode. These effects are explained below.

- **Rate of electrode reactions and current flow**

For any type of electrode reaction, the Arrhenius equation relates the activation energy to a rate constant, k:

$$k = A\,e^{-\Delta G/RT} \qquad (13)$$

where G is Gibbs free energy of activation (known as the activation energy), R = 8.314 J/mol/K (gas constant), T is the absolute temperature in Kelvins, and A is the coefficient of reactions or frequency factor when the interpretation of G is based on the energy barrier. In a fashion similar the way the kinetics of electrode reactions are described, the free energy can be related to the electrode potential. A typical free energy profile along a reaction coordinate has been shown in Figure 2.5. The heavier dashed line in the figure indicates the effect of a positive potential, E = V. A shift in the potential to value E changes the relative energy of the electron on the electrode by –nFV, where n is the number of electrons exchanged, and F is the Faradic constant (equal to 96,500 C), which enables the anodic (Ox) and cathodic (Red) activation energies to be expressed as follows:

$$\Delta G_c = \Delta G_{0c} + \alpha nFV \qquad (14)$$

$$\Delta G_a = \Delta G_{0a} - (1 - \alpha)nFV \qquad (15)$$

α is called the transfer coefficient and ranges from zero to unity.

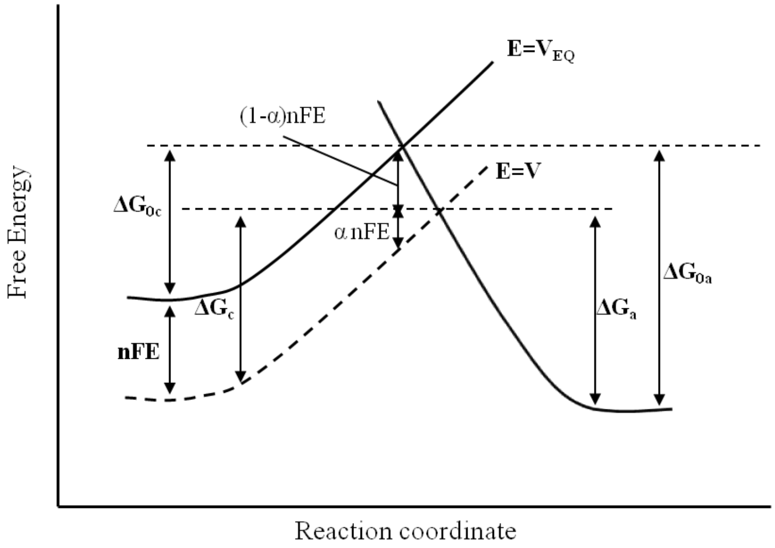

Figure 2.5 The effects of a potential change on the free energies of activation for electrode reactions

Based on the Arrhenius form, the rate constants, k_f and k_b can also be defined:

$$k_f = A_f\, e^{-\Delta G_c/RT} \qquad (16)$$

$$k_b = A_b\, e^{-\Delta G_a/RT} \tag{17}$$

Inserting the activation energies (14) and (15) gives

$$k_f = A_f\, e^{-\Delta G_{0c}/RT} e^{-\alpha n FV/RT} \tag{18}$$

$$k_b = A_b\, e^{-\Delta G_{0a}/RT} e^{(1-\alpha) n FV/RT} \tag{19}$$

The equilibrium condition at the interface can then be considered, where the first two factors are designated by k_f^0 , k_b^0 and are equal to the rate constant, at $E=V_{EQ}$:

$$k_f = k^0 e^{-\alpha n F(V-V_{EQ})/RT} \tag{20}$$

$$k_b = k^0 e^{(1-\alpha) n F(V-V_{EQ})/RT} \tag{21}$$

Insertion of these relations into the net current yields the complete current-potential characteristic, which is called the Bulter-Volmer equation [41]:

$$i = i_f - i_b = nFAk^0\left[C_{ox} e^{-\alpha n F(V-V_{EQ})/RT} - C_{Red} e^{(1-\alpha) n F(V-V_{EQ})/RT}\right] \tag{22}$$

For a particular case, $C_{OX} = C_{Red} = C$, so that

$$i = i_0\left[e^{-\alpha n F(V-V_{EQ})/RT} - e^{(1-\alpha) n F(V-V_{EQ})/RT}\right] \tag{23}$$

where $i_0 = nFAk^0C$, which is defined as the exchange current. This equation can be used for consideration of electrode reactions that require description of the charge transfer, and adsorption processes but involve no mass transport effects.

- **Charge-transfer and adsorption impedance**

The charge transfer process involves tunneling over the double-layer region that separates the electroactive species from the interface (Figure 2.4), and is controlled by the Faradaic current, which refers to the rate of electron transfer near the surface of electrode in the double layer. This charge transfer behavior is thus reflected by the relation between the potential and the current, as defined in Eq. (23).

When the overpotential, $V - \mathrm{V_{EQ}}$, is very small and the electrochemical system is at equilibrium, the net current can be written as

$$\mathrm{i} = \mathrm{i_0} \left[\frac{-\mathrm{nF}(V - \mathrm{V_{EQ}})}{\mathrm{RT}}\right] \tag{24}$$

This expression establishes that the net current is linearly related to the overpotential. Consequently, the ratio $-(V - \mathrm{V_{EQ}})/\mathrm{i}$ has dimensions of resistance and is often called the charge transfer resistance:

$$\mathrm{R_{ct}} = \frac{\mathrm{RT}}{\mathrm{n\,F\,i_0}} \tag{25}$$

This parameter can be evaluated directly in some way, and it serves as a convenient index of the kinetics on the surface of electrode. For example, if no electron transfer exists, the charge transfer resistance becomes very large, and the electrode is polarizable, with poorly defined potential.

The adsorption process usually originates from the kinetics of specifically adsorbed or desorbed species in the double layer. The adsorbed species typically do not exchange electrons directly with the electrode and do not produce a Faradaic current, but they change the density and capacity of the surface charge, creating a purely AC current path and resulting in adsorption impedance. This process is also generated from the formation of a charge associated with the specific adsorption or desorption of charged species so that the adsorption process causes an additional pseudocapacitive effect.

A derivative of adsorption impedance is connected with the amount of adsorbed species Γ (in units of mol/cm^2), and the adsorption capacitance (C_{ads}) and adsorption resistance (R_{ads}) are then expressed [43] as follows:

$$C_{ads} = \frac{F^2 A \Gamma}{4RT} \quad (26)$$

$$R_{ads} = \frac{2RT}{F^2 A \Gamma k_f} \quad (27)$$

where A is the surface area of the electrode, and k_f is the rate constant for the adsorption-driven kinetics. With respect to their relationship, it is recognized that the adsorption capacitance often increases and the resistance decreases due to the acceleration of the adsorption kinetics rate constant and the associated increase in the amount of the adsorbed species with elevated temperatures. However, it is known that these effects exceed the direct decrease in C_{ads} and the increase in R_{ads} with the temperatures indicated in Eq. (26) and Eq. (27).

2.1.4 Critical Parameters in EC Design and Performance

With the goal of designing an EC for a specific application that requires a high level of energy density or high power density or both, many researchers have made significant progress with respect to both the theoretical and practical development of ECs and have published a large number of research articles and technical reports. The reported results reveal that EC performance is predominantly characterized by the following factors:

- **Specific capacitance and equivalent series resistance**

As discussed in the previous section, the capacitance (C) is dependent on the mechanism through which electrochemical capacitors store energy. For a typical parallel plate capacitor, the capacitance, which is measured in farads (F), is directly proportional to the SSA of the electrode and the relative permittivity of the electrolyte, and inversely proportional to the effective thickness of the double layer as indentified in Eq. (1). The density of the electrode material will also significantly affect capacitor performance; such parameters are usually expressed as gravimetric energy (Wh/kg) and power (W/kg) densities. The most important metric of an electrode material is therefore its specific capacitance parameter, such as the gravimetric (F/g) or volumetric capacitance (F/cc) of the device.

The main indicator of EC power capability is based on the direct current resistance or equivalent series resistance (ESR). A lower ESR can obviously supply peak powers more efficiently, leading to increased overall system efficiency and cycle stability. In practical EC devices, a number of factors contribute to resistance: the electronic resistance of the electrode material, the interfacial resistance between the electrode and the current-collector, the resistance of the ions moving through the separator, and the intrinsic resistance of the electrolyte.

- **Energy and power density**

Two primary attributes of an EC are its energy and power density. The electrical energy stored in a charged capacitor is established between the plates that accommodate charges +Q and –Q at a voltage difference, V; the stored energy (E) is therefore calculated from

$$\mathrm{E} = \frac{1}{2}\mathrm{Q} \times \mathrm{V}\ (\text{or } \Delta\mathrm{V}) = \frac{1}{2}\mathrm{CV}^2 \tag{28}$$

Maximum energy density is achieved when V and C are at maximum levels, but this value is applicable only in the case of ideal EDLCs that have no equivalent series resistance or parallel leakage resistance. This value thus reflects the theoretical maximum energy density

[17]. In practice, the cell voltage usually falls appreciably with the extent of the charge consumed, and an integral Q·dV is required because V drops during the discharge.

Power (P) generally refers to the rate of energy delivery per unit of time, or it can correspond to a specific rate of discharge into a given load resistance at a particular current. Power density can be defined as the current (I) multiplied by the differential potential (V), but the internal resistance of a capacitor limits its maximum power. The potential normally decreases with increasing I owing to an ohmic IR drop caused by the internal series resistance of the cell (R_S) or by the effects of kinetic polarization. However, Miller has shown how maximum power delivery can be calculated with use of a simple series RC circuit [44]. When maximum power delivery as described in Eq. (29) is considered, the maximum discharging current I_{max} is V_i (initial potential)/$2R_S$ so that the maximum potential can then be defined as $V_i/2$. The maximum power densities can therefore be expressed as

$$P_{max} = I \times (V_i - IR_S) = I_{max} \times V_{max} = \frac{1}{4R_s} V^2 \text{ or } \frac{\text{Energy}}{\text{Discharging time}} = \frac{E}{t} \qquad (29)$$

From these equations, it can be seen that V, C and Rs are three important variables that determine EC energy and power densities. Maximum energy density is proportional to its capacitance and operating voltage window, meaning that increasing the capacitance and the EC voltage within the stability of the electrolyte is an effective method of improving energy density. Such an enhancement can be achieved by increasing the specific capacitance of the electrode materials as well as by selecting appropriate electrolytes. Eq. (29) also indicates that the larger the ESR, the lower power density will be. If the goal is to improve EC performance by increasing the power density, the major focus should be reducing the ESR.

- **Self-discharge**

In contrast to their discharged state, charged batteries are in a state characterized by a high level of free energy, which means that a specific thermodynamic force provides a stable voltage in a charged state. Unlike batteries, electrostatically charged ECs have no mechanism that thermodynamically or kinetically stabilize their voltages. As a result, the charge status can be easily disturbed, causing to their self-discharge. To date, very little work has been conducted with the objective of uncovering the self-discharge mechanism in ECs, but it is known that an electrostatically determined potential difference can be easily disturbed by a depolarizing process set up, e.g., from an impurity or from internal redox reactions [45-48]. The self-discharge creates a decline in voltage so that the charge is lost, causing the capacitor to approach malfunctioning condition. EC self-discharge behavior therefore constitutes an unreliability factor in energy storage and makes the self-discharge characteristics of an EC important in evaluating its performance. A study revealed that ECs are characterized by a low duration and by a high self-discharging rate of 10 to 40% per day [49].

- **Temperature dependence**

The dependence of EC performance on temperature can be of practical significance in the operation of a variety of applications. For example, if their cycle life performance for a wide range of temperature is considered, ECs could function effectively in specific environments such as in vehicles or for cold-starting in northern climates. Typical operating temperatures range from -40 ℃ to 70 ℃. However, under high power operating conditions, internal heat generation raises the temperature of the device, which strongly influences cycle life performance. Capacitance degradations are also influenced by temperature. A practical evaluation of the effects of temperature on power availability, capacitance and degradation of materials with respect to cycle life is therefore necessary. These factors will play an important role in technology development and device testing for a variety of applications, in which reliable energy storage is required for the operation of proprietary electronic devices under all temperature conditions.

2.2 Materials and Components of ECs

As discussed previously, a key challenge with respect to ECs is their limited energy density, which has hindered their wider application in the field of energy storage. To overcome this challenge, a major focus of EC research and development should be to discover new electrode materials whose properties offer high capacitance and reliability. For the design of EC electrode materials, preferred material properties include: (1) a larger SSA, which translates into a greater number of active sites; (2) suitable pore-size distribution, an appropriate pore network, and an effective pore length for facilitating a high rate of ion diffusion of ions at a high rate; (3) a low internal electrical resistance for efficient charge transport in electrodes, and (4) better electrochemical and mechanical stability for good cycling performance. EC electrode materials can be categorized into four general types: (1) carbon-based materials; (2) conducting polymers; (3) metal oxides, such as RuO2, MnO2; and (4) composite materials. A second key component is related to the properties of the electrolytes which determine the performance of EC devices in three ways: (1) the conductance of the electrolytes is responsible for the ESR of the device; (2) the effective ioin size determines the accessibility of the electrolyte on the surface of the electrodes, which influences specific capacitance; (3) the limitation of operating voltage due to their decomposition, which results in reduced energy and power density. The reminder of this section discusses the types of carbon materials used in EC electrodes, especially in EDCLs, the fabrication method of electrodes, and the kinds of electrolytes.

2.2.1 Carbon Materials as Electrodes in EDLCs

A number of forms of carbon materials have recently been used for storing the charge in EDLC electrodes: activated carbon, carbon nanotubes and graphene. The advantages of these carbon materials include low cost, ease of processing, large surface area, good electronic conductivity, strong chemical stability, and a wide range of operating temperatures. Carbon materials normally store charges primarily in an electrochemical double-layer formed at the interface between the surface of the electrode and the electrolyte, rather than in the bulk of the material as with conducting polymers or metal oxides. According to Eq. (1), the capacitance of an EC is observably dependent on the SSA of the electrode materials. However, the experimentally measured capacitance of a variety of materials fails to increase linearly with an increasing SSA because not all of the surface area is electrochemically accessible to the electrolytic ions [26, 50]. In other words, specific capacitance is sometimes not directly proportional to the SSA because electrode pores that are too small (usually micro-pores under 2nm) offer poorly accessible porosity for the electrolytic ions, resulting in lower capacitance. One researcher [51] has suggested an empirical relationship between the distribution of pore size, the energy density, and the power density of a device. A larger pore size correlates with higher power densities, and a smaller pore size correlates with higher energy densities. Important factors in EC performance include therefore the SSA, pore-size distribution, pore shape and structure, electrical conductivity, and surface functionality at the interface between the electrodes and the electrolytes [24, 52-56].

2.2.1.1 Activated Carbon

The term activated carbon (AC), also referred to as engineered carbon, encompasses a variety of materials, from amorphous carbon to ordered graphite. The properties of these materials are determined based on their processing through high temperature carbonization in an inert gas (generally, N_2 or Ar) in conjunction with the choice of precursor material [57, 58]. Following the carbonization of the precursor materials, further enhancement by way of activation may be required in order to open existing pores blocked by residual amorphous carbons and in the process, to create new ones, thus increasing the overall porosity. Commercially available ACs generally have a large surface area resulting from the activation process, and are commonly used in existing EC products. The re-activation of commercial ACs has also been carried out as a means of improving EDLC performance, and has been reported to have a beneficial effect [59]. Another method is based on wettability as a factor for increasing the accessible surface of ACs, which can be improved through surface functionalization, thus enhancing the affinity between the electrolyte and the carbon surface [60]. These functionalization processes can also provide a means of incorporating pseudo-capacitive mechanisms during cycling; however their concentration must be optimized in order to avoid degradation of mechanical stability (aging) and loss of intrinsic conductivity in the electrode [61, 62]

On the other hand, research [26] has revealed that available AC materials have a large SSA (1100 m^2/g to 2570 m^2/g) but unfortunately also exhibit poorly accessible porosity for electrolyte ions, resulting in limited capacitance: around 100 F/g for AC with 2130 m^2/g but only 63 F/g for AC with 2570 m^2/g. Another study [27] has reported capacitance values of 150 F/g and 300 F/g with the use of aqueous and organic electrolytes, respectively. The difference in capacitance observed through the use of varied electrolytes is due to the relationship between pore and ion size: organic electrolytes are larger than their aqueous counterparts and thus cannot penetrate the pore volume to an equivalent extent (in the range of micro-pores). These research results lead to the conclusion that an empirical relationship exists between the distribution of pore size and performances, and suggest that the control of pore size is critical for optimizing ion transport channels and for increasing the charge stored on electrodes [63, 64].

2.2.1.2 Carbon Nanotube

Carbon nanotubes (CNTs) possess unique properties that promote their use as an EDLC electrode material. Their high degree of electrical conductivity, effective mechanical and thermal stability, and highly accessible network of pores have motivated considerable research with respect to the development of high-power ECs [54]. As shown in Figure 2.6 (a), based on differences in geometric structure and in electrical and mechanical properties, CNTs can be classified into two types, single-walled nanotubes (SWCNTs) and multi-walled nanotubes (MWCNTs) [65, 66]. CNTs ideally provide 4 types of spaces that are accessible to electrolyte ions, as shown in Figure 2.6 (b).

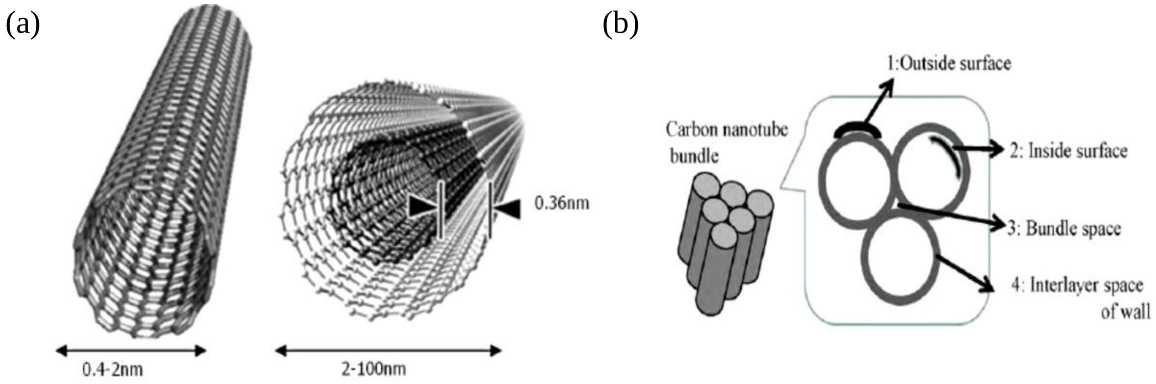

Figure 2.6 Illustration of CNTs: (a) representation of a SWCNT (left) and a MWCNT (right) [65]; and (b) schematic diagram of CNT spaces available for electrolyte ions storage [66]

However, most CNTs are known to be bundled together due to the van Waals force and the so-called bundle spaces among the tubes (indicated by #3 in Figure 2.6 (b)) are really the only exposure to the electrolyte, which hinders the formation of the EDLC. De-bundling of the CNTs is therefore required so that all of the tube surfaces are available for electrolyte ions. In one study [67], the SSA of individual carbon nanotubes and bundles of carbon nanotubes were calculated as a function of the tube diameter, the number of walls and the number of carbon nanotubes in a bundle. The SSA of an individual tube with a 1 nm diameter can be as high as 1315 m^2/g, but is only 400 m^2/g for bundles with a 7 nm diameter (comprised of 1 nm SWCNT). These results indicate that significant potential for improvement with respect to CNT surface area through optimization of the morphology of the CNT film used as an electrode.

The reported specific capacitance values of the CNTs range from 20 F/g to 300 F/g, and are reliant on their production, treatment methods and the type of electrolyte [68-71]. EC electrodes prepared from MWCNT were first reported by Niu et al.[69]. Their specific capacitance, power and energy density values were 113 F/g, 8 kW/kg and 0.56 Wh/kg, respectively, when a 38 wt% H_2SO_4 aqueous solution was used as the electrolyte. A study by An et al. [71] demonstrated that the specific capacitance achievable using an electrode based on heat treated SWCNTs as the active layer is around 180 F/g in 7 M KOH and that the BET surface area was 357 m^2/g. They also found that increasing treatment temperatures resulted in a corresponding increase in SSA, a decrease in average pore diameter, and an increase in specific capacitance. Organic electrolytes have also been employed for the development of CNT supercapacitors [72-74]. Emmenegger et al. [73] showed that the average specific capacitance can reach 66 F/g with 1M Et_4NBF_4 mixed in acetonitrile. Liu et al.[74] reported that the specific capacitance of SWCNTs in an organic electrolyte ($TBAPF_6$) is around 80 F/g.

Due to their relative ease of fabrication, randomly networked CNTs were the first type of CNT electrodes to produce elevated power capabilities with a moderate SSA, however, the small surface area still leads to lower energy density. As with all other nanostructures, CNTs have a tendency to agglomerate, resulting in an entangled arrangement with an irregular pore structure. This effect can alter the SSA of the CNT network and the ion mobility in the electrolytes, with a consequent negative effect on performance. As a result, essential goals now include either the development of an appropriate processing technology that enable CNTs to be coated with effective structural geometries (e.g., a large surface area and uniform pores with optimized ion accessible paths) or the creation of enhanced processing treatments, such as functionalization or aligned CNT growth.

Several research groups are currently developing a variety of deposition techniques that will increase the adsorption sites available to the ions in CNT networks. A typical procedure for preparing carbon-based electrodes usually involves cast-coating using a slurry mixture of carbons, conductive agents (such as carbon black) and a polymer binder. However, this method is inefficient for CNT materials because of their agglomeration. As listed in Table 2.1, several fabrication techniques have been recently developed for CNT materials and have demonstrated higher specific capacitances: electrophoretic deposition (EPD) [75], vacuum filtration [76], ink jet printing [77, 78], and electrostatic spray deposition [79, 80].

Table 2.1 Examples of CNT electrodes using different deposition method

Fabrication method	CNT type	Capacitance (F/g)	Reference
Vacuum filtration	DWCNT	67	[76]
Ink jet	SWCNT	74	[78]
Spay deposition	SWCNT/MWCNT	90-150	[79, 80]
Layer by Layer	MWCNT-COOH MWCNT-NH2	150	[81]
Electrophoretic deposition	MWCNT	85	[75]

Drawing meaningful conclusions about electrode fabrication methods based on a comparison of these studies is difficult because the researchers employed different CNT sources as well as disparate solution processing and characterization protocols. However, the deposition method obviously affects the porosity of the electrode, which is dependent on how easily the electrolyte ions can move into and out of the electrode during the charge/discharge process. Recent research has also demonstrated that aligning CNTs through pyrolysis methods enable bulk CNT materials to retain their intrinsic properties to produce a more mesoporous and more accessible surface [82]. Several studies have demonstrated that the improved rate capability of aligned CNTs compared to randomly entangled CNTs [83-85]. The effective arrangement obtained by Chen et al. [84] can provide a greater capacitance of 365 F/g for an aligned CNT array electrode in a 1M H_2SO_4 electrolyte as well as reduced resistances compared to that in entangled networks. An additional important property that affects the capacitance behavior of CNT electrodes is the wetting capability of the electrode materials. For instance, chemically treated CNTs exhibit improved electron transfer kinetics and create greater surface area. In this regard, CNT electrodes functionalized with nitric acid [86], fluorine [87], or ammonia plasma [88] have been tested with respect to their effect on capacitance performance. However, the pseudo-Faradaic reaction induced by the surface functional groups leads to unstable capacitance and increased current leakage [86].

2.2.1.3 Graphene

Graphene, a two-dimensional single layer of carbon atoms, is distinctly different from ACs and CNTs. The comparison in Figure 2.7 shows that graphene is characterized by a unique morphology that is described by a single layered 2-D lattice structure of carbon atoms so that its accessible surface area of graphene is distinct from that of any other carbon materials used in EDLCs. While other materials rely on a fixed porous structure for transporting and adsorbing electrolyte ions, a graphene layer well-dispersed within a solution provides a theoretically available surface area of 2630 m^2/g. Such an SSA would ideally remain completely accessible to the electrolyte ions and is much larger than that associated with AC or CNTs. Other outstanding characteristics of graphene are its high level of intrinsic carrier mobility (200,000 cm^2/V·S), high degree of thermal conductivity (~5000 W/m·K), high Young's modulus (~1.0 TPa) and high optical transmittance value (~97.7 %) [89]. These exceptional features make graphene a promising carbon candidate for EC electrodes.

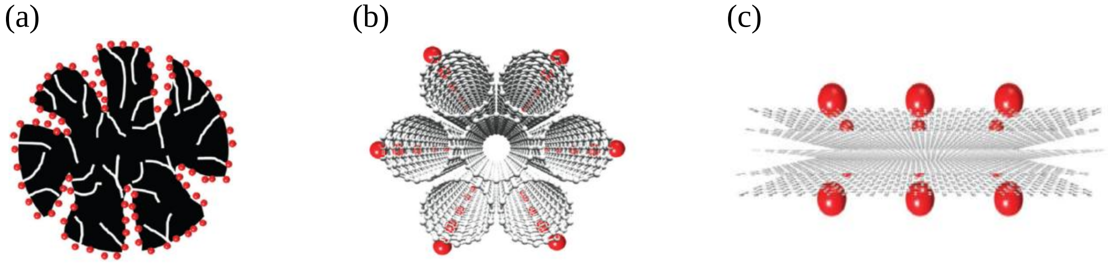

Figure 2.7 Comparison of carbon materials for use as EC electrodes: (a) activated carbon, (b) carbon nanotube, (c) graphene [90]

In several studies, graphene has produced a high specific capacitance ranging from 100 to 250 F/g, and recent work has achieved notably high energy density values with a variety of electrolytes [91-96]. Vivekchand et al. [92] prepared graphene in three different ways: (1) by thermal exfoliation of graphite oxide (GO); (2) from a nano-diamond heated at 1650 ℃ in a helium atmosphere; and (3) through decomposition of camphor over nickel nanoparticles. Graphene samples prepared through the first two processes have been observed to exhibit a high specific capacitance in aqueous H_2SO_4: up to 117 F/g, with an appreciably high energy density value. Chemically modified graphene (CMG) has also been utilized as an electrode material for energy storage devices. Stoller and his co-workers [93] achieved a substantially high BET surface area (750 m^2/g) for CMG aggregates and demonstrated specific capacitance values of 135 F/g and 99 F/g in aqueous (KOH) and organic (TEABF$_4$ in AN) electrolytes, respectively. Using another approach, functionalized graphene sheets (FGS) were prepared through a low-temperature thermal exfoliation procedure [95]. A first type of FGS was obtained by thermal exfoliation of GO at a low temperature in air. A second type was prepared by carbonizing the first type of FGS at a higher temperature in N^2. The specific capacitance value of the first type of FGS was 230 F/g, compared to 100 F/g obtained in an aqueous electrolyte (KOH). However, the second type of FGS demonstrated higher capacitance retention, with a high current density, as result of it favorable conductive behavior.

Owing to unique structure and desired electrical and mechanical properties, graphene has a strong potential for effective use in advanced ECs. However, a few remaining obstacles still stand in the way of industry development. First, like other materials, graphene is also likely to form irreversible agglomerates or to restack to form graphite, which causes a reduction in electrolyte ion accessibility. Second, fabricating a graphene electrode without a binder is challenging and usually results in a lower specific capacitance. A final consideration is that the development of a production process requires the creation of more cost-effective methods that would also retain the intrinsic properties of the graphene.

2.2.2 Electrode Fabrication Methods

For the design of EC structures, the most important EC component is the electrode. The development of EC electrodes has generally originated from efforts to optimize the structure of the interface reaction between the electrodes and the electrolyte and to advise relatively low cost in fabrication methods. Significant progress with respect to techniques for fabricating nano-structured electrodes has been achieved, which has greatly improved their performance. To date, a variety of methods have been introduced for fabricating EC electrodes, including cast-coating, electro-deposition [97, 98] and vacuum filtration [99, 100]. In the cast-coating technique, electrodes are fabricated from conducting particles of carbon powder (e.g., AC) along with a fluorine-containing polymer (PTFE) binding agent, which are mixed together by means of a solvent to produce a paste or slurry material. This technique is already well known and is used in the production of commercial ECs. For CNT materials as mentioned in section 2.2.1.2, different deposition methods have been developed in order to address the agglomeration of carbon materials. A promising fabrication technique for carbon-based electrodes is electrophoretic deposition (EPD). Another method is vacuum filtration, which forms a thin film as an electrode. These three common electrode fabrication methods are described in detail in the following subsections.

2.2.2.1 Cast-Coating

A thin film can be obtained by cast-coating or drop-coating colloidal materials (slurry) directly onto substrates. Active materials (carbon powders) can be mixed with conductive additives (carbon black, etc.) and a binder to produce slurries, which can then be pasted on or penetrated into flat or porous substrates as depicted in Figure 2.8. In this process, the attainable storage capacity and the internal resistance of an electrode are significantly dependent on its microstructure, and the electrical contact between the active materials is of great importance. According to the literature, integrating conductive nanoparticle powders such as carbon black or carbon nanotubes, has been shown to increase gravimetric capacity.

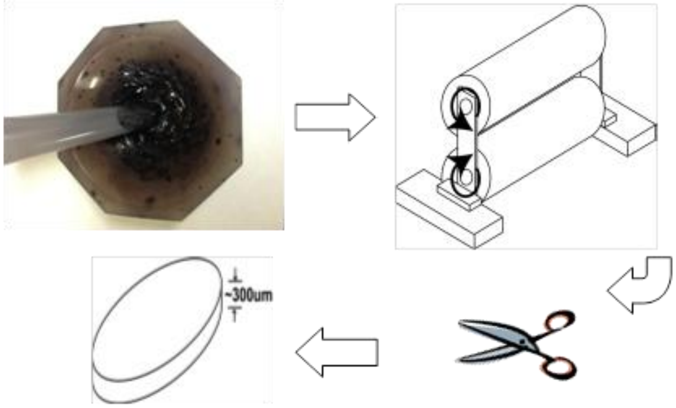

Figure 2.8 Description of cast-coating using slurry

Conductive powder shows negligible self-capacitance, but electrically isolated regions are avoided in the microstructure of the electrode [101]. Other research has shown that the solvent content is an important variable that controls pore size and ultimately the capacitance of an electrode [102].

2.2.2.2 Electrophoretic Deposition (EPD)

Electrodeposition, specifically electrophoretic deposition (EPD), is the preferred method of fabricating thin film electrodes due to the low capital investment costs involved, the rigid control of film thickness, the uniformity of the final product, the fast processing rate and the suitability of this method for large-scale production [103, 104]. An additional attraction lies in its simplicity and feasibility for manufacturing homogeneous composite coatings on complex substrate shapes. EPD is fundamentally a combination of electrophoresis and deposition processes. In the first step, an electrical charge is developed in the surface via charged species when dispersed in a polar solvent. The individual charged nano-particles suspended in the solution are forced to move toward an oppositely charged electrode under an external electric field. This motion, which is referred to as electrophoresis, is illustrated in Figure 2.9. In this process, the plane that separates the tightly bound liquid layer from the remainder of the liquid is called the slip plane. The electric potential at the slip plane is known as the zeta potential, which is an important parameter for determining the stability and transport of a nano-particle suspension. The zeta potential, ζ (V), around a particle can be described as follows [105]:

$$\zeta\,(\mathrm{V}) = \frac{\mathrm{Q}}{4\pi\varepsilon_{\mathrm{r}}a(1+ka)} \tag{30}$$

where Q is the charge on the particle, *a* is the radius of the particle, ε_{r} is the relative dielectric constant of the solvent and *k* is a system constant calculated based on the concentration and temperature of the solution. In the second step, the nano-particles are deposited and collected on the surface of the electrode, where they form a thin film.

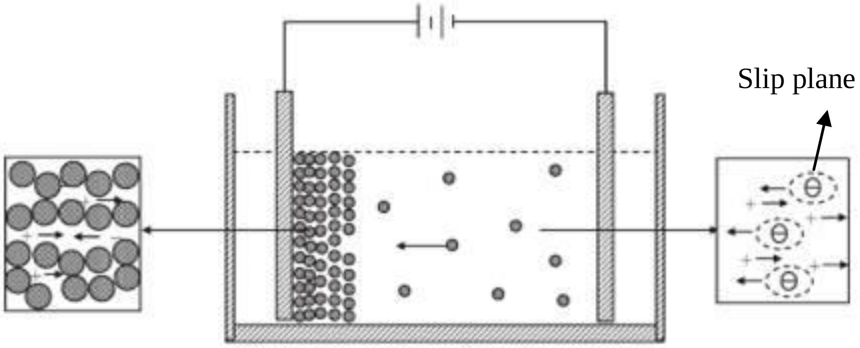

Figure 2.9 Schematic diagram of electrophoresis [106]

The literatures contains reports [107-111] of the use of the EPD for the fabrication of nanostructures, and it is now well known that this technique is very convenient for manipulating nano-structured materials, including nano-sized metal particles, carbon nanotubes (CNT), nanowires and nanorods. For CNT, the first report, by Gao et al. [108] published the first reported investigation of the use of EPD for single-walled CNTs that had been sonicated in either methanol or dimethiylformamide as means of preparing stable suspensions. After a 10min deposition time, thin CNT films (~1 μm thickness) were obtained using a DC field of 20 V/cm. In related research, Du et al. have fabricated CNT films using EPD and have described the properties of such thin film electrodes for supercapacitors [110]. Thomas et al. produced uniform deposits of multi-walled CNTs on stainless-steel substrates. They controlled the thickness of the coating by varying the voltage and deposition time during the EPD [109]. Detailed investigations have also been carried out in order to examine the correlations between the electrochemical properties of the deposited CNT films and EPD processing parameters, such as particle mobility, deposition temperature, and processing time. Previous studies [75, 98] revealed that the EPD deposition rate is dependent on electrophoretic mobility, μ (m^2/Vs); field strength, E (Vm); processing temperature and processing time. More importantly, as discussed previously, electrophoretic mobility is determined by the properties of the suspended particles, such as their surface charges (indicated by the zeta potential) as well as the properties of the suspensions themselves, including the viscosity of the liquid and the concentration of the solution. The successful production of CNT films by EPD processing requires a well dispersed colloidal suspension. For instance, an acid-treatment has often been applied, which has been obtained by mixing a specific oxidizing agent (e.g., HNO_3/H_2SO_4, O_3, KMnO4 or H_2O_2) into CNT suspensions. The presence of hydrophilic oxygen-containing functional groups on the surface of acid oxidized CNTs generates either negative or positive surface charges and helps disperse individual CNTs within the suspension. The surface charges of the CNTs also vary with the oxidation levels (indicated by the concentration of surface oxygen on the CNTs in the form of COOH, C-OH or C=O) and the pH values of the suspension. Studies [112, 113] have shown that the nanotubes are negatively charged if the pH value is greater than 3 and that more negative charges are homogeneously accumulated on the surface of CNTs if the pH value increases. It can be concluded that varying the pH value of the suspension changes the surface charge state of acid-treated CNTs and consequently affects the transport properties of the CNTs as well as the EPD deposition rate.

2.2.2.3 Vacuum Filtration Method

Compared with other methods, the vacuum filtration method is regarded as the simplest process for the fabrication of thin, transparent, optically homogeneous conducting film, usually composed of CNTs or graphene. As shown in Figure 2.10, this method involves drawing a surfactant-based suspension through cellulose, ceramic or another filter that has a pore size in the micrometer range. A vacuum or other pressure differential is created in order to force the suspension through the filter, and the surfactant is then washed away with purified water so that a film of pure CNTs or graphene can be formed. Vacuum filtration is usually faster than simple gravity filtration which is used for removing an insoluble solid material from a solution. However, the limitations of this method are the lack of control of variations in the thickness, the difficulty of separating the thin film from the filters, size restrictions, and the challenges associated with the handing of the processed films [114].

In several studies, the vacuum filtration technique has been employed for producing nano-structured electrode films that provide a high degree of conductivity and transparency. Wang et al. [99] fabricated graphene films based on a cellulous ester filter membrane for the vacuum filtration of a graphene aqueous colloid. The resulting graphene films offered excellent electrical conductivity with superior transparency of well over 80 % as well as sheet resistance lower than that of spin-coated films. A filtration method was also used for preparing thin CNT networks, whose characteristics were then studied. Cooper et al. [76] reported that freestanding, thin and bendable electrodes for supercapacitors can be fabricated by filtering dispersed multi-walled CNTs in the form of a film, and that such a film exhibited non-Faradic double layer behavior. Another study [115] demonstrated that single-walled CNTs post-treated with nitric acid or fabricated with an acid pre-treatment provide superior performance compared to those made with high-purity CNTs without any acid treatment.

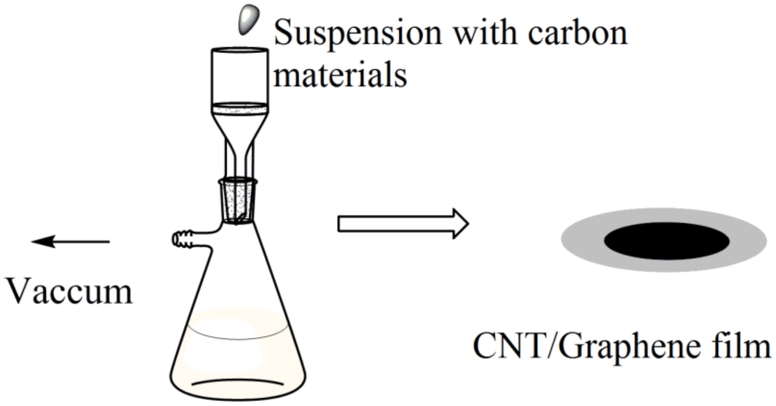

Figure 2.10 Schematic of the preparation of electrodes using vacuum filtration

2.2.3 Electrolytes in ECs

Because EC performance is dependent not only on the electrode materials but also on the properties of the electrolyte, an understanding of electrolyte properties is essential for improving EC performance with respect to such factors as energy density, power density, efficiency, and reliability for high-temperature operation. The previous section discussed the development of two types of ECs, EDLCs and pseudocapacitors, and explained the requirements of both types with respect to a wider potential window (operating voltage, V) and lower ESR (internal resistance, Ω) in order to achieve high energy and power densities. An additional factor is that capacitance is also affected by the effective size of the ions, which determines the accessibility of the electrolyte on the surface of the electrodes. For commercialized EC devices, electrolyte choices include organic and inorganic (aqueous). Based on their inherent properties, each type offers specific benefits and disadvantages with respect to electrolyte conductivity, ion size, and electrochemical stability (voltage limitations), all of which must ultimately be taken into account when a capacitor cell is designed for a desired application.

2.2.3.1 Inorganic (Aqueous) Electrolytes

The advantages of aqueous electrolytes are their higher conductance (e.g., 800 mS·cm for H_2SO_4 compared with 5 mS·cm to 60 mS·cm for non-aqueous electrolytes) [116] and the fact that the purification and drying processes during production are less stringent. Aqueous electrolytes also have smaller solvated ions and higher dielectric constants, both of which promote capacitance, as expressed in Eq. (1). The cost of aqueous electrolytes is usually much lower than that of suitable organic electrolytes. Despite these advantages, aqueous electrolytes have the drawback of being limited to applications for industrial capacitors because of their thermodynamic electrochemical decomposition, which results in a restrictive, relatively narrow potential range [117]. With aqueous electrolytes, in general, the unit cell voltage of the EC is typically constrained to 0.8 V to 1.0 V in order to avoid the loss of the electrolyte, thus significantly reducing the energy density available compared to organic electrolytes. However, one of the benefits of aqueous electrolytes is that, especially on carbon materials, they enable the existence of a pseudocapacitance based on the redox reaction of the hydrated functional groups at the surface of the carbon materials. This effect can, for example, double the value of the capacitance on a carbon material in an aqueous electrolyte relative to the results with the same material in an organic electrolyte.

When electrolytes that contain strong acids or alkaline ions are used, additional consideration must be given to the current collector/electrolyte choice. These ions are preferred because of their increased ion conductivity, but corrosion can be a problem with stainless steel current collectors. From this perspective, ECs that employ aqueous electrolytes would be attractive, but strategies must be found not only for increasing the operating voltage but also for acquiring inexpensive and light current collectors that are resistant to acidic corrosion.

2.2.3.2 Organic (Non-aqueous) Electrolytes

The advantage of an organic electrolyte is the higher achievable voltage it creates. According to the equation of energy density (Eq. (28)), the square of the cell voltage determines the maximum stored energy. Organic electrolytes produce a cell voltage above 2 V with the possibility of short-term increases to 2.7 V, which gives rise to energy densities six to nine times those provided with an aqueous solution. However, the solvated ion size of organic electrolytes is supposedly larger than that of the protons in inorganic electrolytes, and generally leads to a smaller capacitance. Organic electrolytes also have a significantly higher internal resistance than aqueous electrolytes, which lowers their power density. Nevertheless, organic electrolytes are preferred over the aqueous version for commercialized EC devices since the reduction in power is compensated for by the higher energy level and wider cell voltage. Table 2.2 indicates the differences in resistivity and voltage limitations among a variety of types of electrolytes used in ECs. Due to their greater operating potential (up to 2.7 V), either organic acetonitrile (AN) or propylene carbonate (PC) are currently used as the electrolyte in the majority of commercial ECs.

Table 2.2 Properties of aqueous, organic and ion liquid electrolytes

Electrolyte	Density (g/cm)	Conductivity (mS/cm)	Resistivity (Ω cm)	Cell voltage (V)
H_2SO_4	1.2	750 (30 wt.%)	1.35	1
KOH	1.29	540 (30 wt.%)	1.9	1
Propylene carbonate	1.2	14.5 (1M Et_4NBF_4)	52	2.5-3
Acetonitrile	0.78	59.9 (1M Et_4NBF_4)	18	2.5-3
Ionic liquid	1.3-1.5	1.5~15	125 (25 ˚C) 28 (100 ˚C)	4 3.25

Further considerations related to the use of organic electrolytes include the requirement for additional procedures to ensure quality with respect to conductivity and resistivity. Solvents are needed for a purification process that removes any residual water content, which can lead to the corrosion of the current collectors at high operating potentials. With respect to commercialization, organic electrolytes are generally associated with a number of safety issues related to transporting toxic, flammable materials. Although propylene carbonate gives rise to fewer safety concerns than acetonitrile, it is considered an environmentally unfriendly solution, and its resistivity is greater than that of acetonitrile. Unfortunately, efforts to find a nontoxic replacement organic electrolyte that yields good ion conductivity have thus far been unsuccessful.

2.3 Characterization Techniques for EC devices

2.3.1 Nano-structures Characterization

2.3.1.1 Specific Surface Area

Initial consideration of surface area with respect to EC characterization is that, based on Eq. (1), a large SSA directly results in a greater capacitance. In general, the surface area of the electrode, i.e., the total non-planar surface area of the carbon, is measured using a technique known as the BET method, named for Brunauer, Emmett, and Teller, who in 1983 described analytically the adsorption of a gas on a solid surface [118]. The resulting measurement is known as the BET surface area, specified in units of m^2/g.

The underlying concept is an extension of the Langmuir theory, which postulates the mechanisms for monolayer molecular adsorption and multilayer adsorption based on the following hypotheses: (a) gas molecules physically adsorb on a solid in infinite layers; (b) no interaction takes place between the adsorption layers; and (c) the Langmuir theory can be applied to each layer individually. In this model, the gas molecules physically adsorb on a solid in infinite layers, and forces active in the condensation of the gases are also responsible for the binding energy that occurs in multi-molecular adsorption. The phenomenon of adsorption based on the BET equation can thus be expressed as

$$\frac{1}{\mathrm{n}[\left(\frac{\mathrm{P_0}}{\mathrm{P}}\right)-1]} = \frac{\mathrm{c}-1}{\mathrm{N_m c}}\left(\frac{\mathrm{P}}{\mathrm{P_0}}\right) + \frac{1}{\mathrm{N_m c}} \tag{31}$$

where P and P_0 are the equilibrium and the saturation pressure of the adsorbates at the temperature of adsorption, respectively; n is the adsorbed gas quantity: and N_m is quantity of the monolayer adsorbed gas. Eq. (31) is an adsorption isotherm and can be plotted as a linear relationship between $1/n\ [(P_0\ /\ P) - 1]$ on the y-axis and P/P_0 on the x-axis, based on experimental results. This type of plot is called a BET plot. The linear relationship of the equation is maintained only in the range of $0.05 < P\ /\ P_0 < 0.35$. The value of the slope b and the y-intercept a of the line are determined in order to calculate the quantity of the monolayer adsorbed gas in nm and the BET constant c according to

$$\mathrm{N_m} = \frac{1}{a+b}\ , \qquad c = 1 + \frac{b}{a} \tag{32}$$

The specific BET surface area S_{BET} can therefore be evaluated by the following equation:

$$S_{\mathrm{BET}} = \frac{(\mathrm{N_m} \cdot \mathrm{N_A} \cdot \mathrm{S})}{\mathrm{m} \cdot \mathrm{V_0}} \tag{33}$$

where N_m is the monolayer quantity of adsorbate gas; N_A is Avogadro's number; S is the adsorption cross section of the adsorbing species; m is the mass of the adsorbent; and V_0 is the molar volume of the adsorbent, which is 22,414 cm^3/molar for a gas at atmospheric pressure. If the pores are viewed as cylinders, then the pore volume V is $\pi(D/2)^2L$, and the pore surface area, S, is equal to πDL. The average pore width is thus equal to 4 V/S based on the BET model, where D is the diameter of the pore, L is the length of the pore, and V is N_m.

2.3.1.2 Pore Size and Distribution

Nano-structured carbon electrodes are usually designed to incorporate both micro-pores (< 2 nm) and meso-pores (2 nm to 50 nm) and are considered critical for the development of energy storage and for the resultant power performance of the electrode. For example, the capacitive and resistive behaviour of EDLCs is strongly correlated with the pore distribution and pore size of the carbon material. In the literature [119, 120], researchers suggest that the storage capacity of an electrode is strongly related to its interfacial double-layer processes, e.g., ion adsorption and transport on the surface of an electrode, and to its structural features, including surface area, porosity, and pore size distribution (PSD).

The efficiency of electrical energy storage, in particular, is governed by the rate at which ions from an electrolyte solution can be delivered to and adsorbed on the available electrode surface area (i.e., accessible pore size). One study also revealed that large cation and anion sizes limit the effectiveness of a conventional AC surface area containing micro-pores (< 2nm) since the ions either virtually fail to fit into the pores or become diffusion-limited at the required scan rates. Nevertheless, AC micro-pores are essential for providing a larger surface area and greater energy storage capacity. In contrast, the presence of meso-pores can accelerate ion transport to the electrode, thus improving power performance at large current densities. When high levels of meso-porosity are created within the electrode materials, both ion accessibility and the average coefficient of the ion diffusion within pores can be enhanced [121, 122] , but this condition also results in a low volumetric capacitance and a reduction in energy density due to excessive pore volumes. The characterization of the structure of an electrode is therefore crucial for achieving high specific power/energy densities with fast charging/discharging rates in carbon materials, which creates reduced ion diffusion barriers and increased accessible surface area with an appropriate degree of porosity.

A number of methods that employ a variety of models have been proposed for the calculation of the PSD of microporous materials, e.g., in order of increasing complexity, the Barrett-Joyner-Halenda (BJH) method [123], the Horvath-Kawazoe (HK) method [124, 125], the density functional theory [126], and molecular simulation methods. The HK method is based on slit-shaped pore geometry and uses the relationship calculated from a modified Young-Laplace equation, especially for micro-pores. With respect to mesoporous materials, the BJH method based on the Kelvin equation provides a convenient way to calculate the PSD. The Kelvin equation used in the BJH method predicts the pressure at which an adsorptive substance will spontaneously condense in a cylindrical pore of a given size. The pore size is then calculated from the Kelvin equation and the statistical thickness equation selected. However, the BJH method severely underestimates the size of small-to-medium meso-pores. For the work presented in this thesis, a combination of the HK method for the > 2 nm region and the BJH method for the 2 nm to 50 nm region has therefore been selected for calculating the PSD because these choices are in good agreement with the known characteristics of the relevant carbon samples [127, 128].

2.3.2 Electrochemical Characterization

2.3.2.1 Cyclic Voltammetry

Cyclic voltammetry (CV) is an electrochemical analysis technique whereby the current of an electrochemical cell is plotted against its voltage at a fixed magnitude of rate of change in the voltage (scanning rate). This technique is not only the usual way of measuring material capacitance but is also the method most often employed in the investigation of faradaic reactions. In theory, an EDLC does not involve a faradaic reaction. In practice, however, EDLC behaviour includes faradaic components due to the redox reaction or the ion kinetics at the electrode/electrolyte interfaces, and CV can provide insight into these processes. A pure capacitor of constant capacitance has a rectangular CV plot; for example, at voltages high enough to initiate a redox reaction, the current increases in an exponential fashion. In the same way, the shape of the voltammetry plot manifests the complexity of the electrochemical processes at play in the EDLC.

In a cyclic voltammogram, the electrode potential rises linearly versus time as shown in Figure 2.11 (a). This ramping usually refers to the potential scanning rate, ν_s (V/s). The potential is applied between the working electrode and the reference electrode, and the current is measured between the working electrode and the counter electrode. These data are then plotted as current versus potential. An ideal EDLC based on CV analysis is represented by a rectangle within a voltammogram plot that has a constant current, as illustrated in Figure

2.11 (b). The following equation is a simple description of the relation between the current and the voltage:

$$\mathrm{I} = \mathrm{C}\frac{\mathrm{dV}}{\mathrm{dt}} = \mathrm{C} \cdot \mathrm{v_s} \qquad (34)$$

where I is the capacitive charging current, and ν_s is the scan rate of the charging voltage. Under conditions in which the resulting voltammogram has a mirror image of potential sweeps, this CV graph can be a useful criterion for establishing reversibility in double-layer capacitive or pseudocapacitive charge and discharge processes. It also constitutes a fundamental characteristic of pure EDLC behaviour in the absence of redox processes. Other materials, however, might not exhibit constant current because of their material resistances, or they might display potential specific faradaic reactions that appear as peaks in the response current due to reversible redox processes typically observable in metal oxides and conductive polymers. Characteristic profiles of these capacitive mechanisms are similar to the CV graph shown in Figure 2.11 (c). As the waveform indicates, the forward scan produces a current peak at the point at which the materials can be oxidized (or reduced depending on the direction of the initial scan) within the potential window scanned. The current increases as the potential reaches the oxidation potential of the electrolyte, but then falls off as the concentration of the electrolyte close to the surface of the electrode is depleted. If the redox couple is reversible, when the applied potential is reversed, it will then reach the potential that produces a current of polarity that is reversed from that of the forward scan. This reduction peak will usually have a shape similar to that of the oxidation peak. In this way, information can be obtained about the redox potential and electrochemical reaction rates of the compounds.

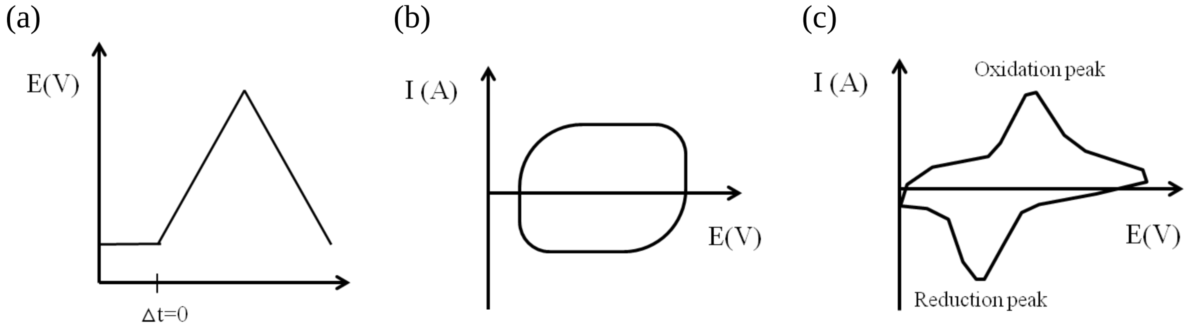

Figure 2.11 Schematic explanation of a cyclic voltammogram (b) in the absence of a redox process and (c) with an active redox reaction

Determining the capacitance, C, from CV measurements requires the integration of the current response into the CV graphs so that C can then be calculated as follows:

$$C = \frac{\int i \cdot dV}{\Delta V \cdot v_s} \tag{35}$$

2.3.2.2 Constant Current Charge/Discharge

The measurement of the CCD, also called galvanostatic charge/discharge, differs from CV because the controlled parameter is the current flowing through the working electrode rather than the potential. When a constant current density, *i (A)*, is applied, a potential difference over time across the cell is linearly created. The capacitance can then be described by the following:

$$C = \frac{\Delta q}{\Delta V} \tag{36}$$

where $\Delta q = \int i \cdot dt$ and can be used to determine the value of the capacitance according to the following:

$$\mathrm{C} = \frac{\Delta \mathrm{q}}{\Delta \mathrm{V}} = \frac{\int i \cdot \mathrm{dt}}{\Delta \mathrm{V}} = i \cdot \frac{\Delta \mathrm{t}}{\Delta \mathrm{V}} \tag{37}$$

where $\Delta\mathrm{t}/\Delta\mathrm{V}$ is the inverse slope of the response curve obtained from the charge or discharge measurements; $\Delta\mathrm{V}$ has a value within the limiting potential difference for electrolyte decomposition; and the current, i, is removed from the integral because it is constant. Figure 2.12 shows typical CCD data for an ideal EDLC cell. An ideally polarized electrode that exhibits a reversible capacitance is described by a constant linear potential increase and decrease during charging and discharging. Otherwise, a dynamic change in the slope of the potential occurs because an equivalent series resistance (ESR), or self-discharge, causes an exponentially shaped charge and discharge voltage curve. Eventually, this distorted curve represents the voltage drop (IR drop) over a cycle, as illustrated in Figure 2.13, and the ESR can be calculated as

$$ESR = \frac{IR\ drop\ (V)}{i(A)} \tag{38}$$

The overall internal resistance in a cell is generally represented by this calculated ESR values.

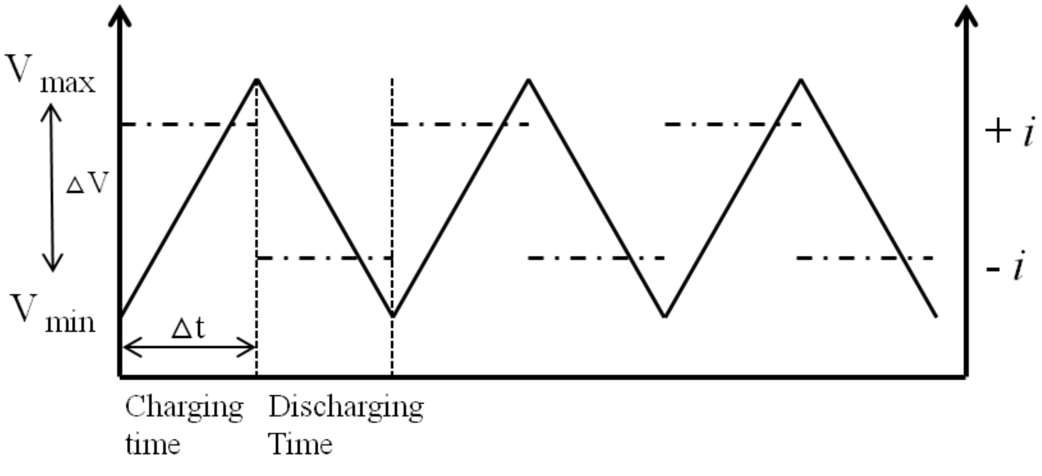

Figure 2.12 Typical CCD test results for ideal EDLCs

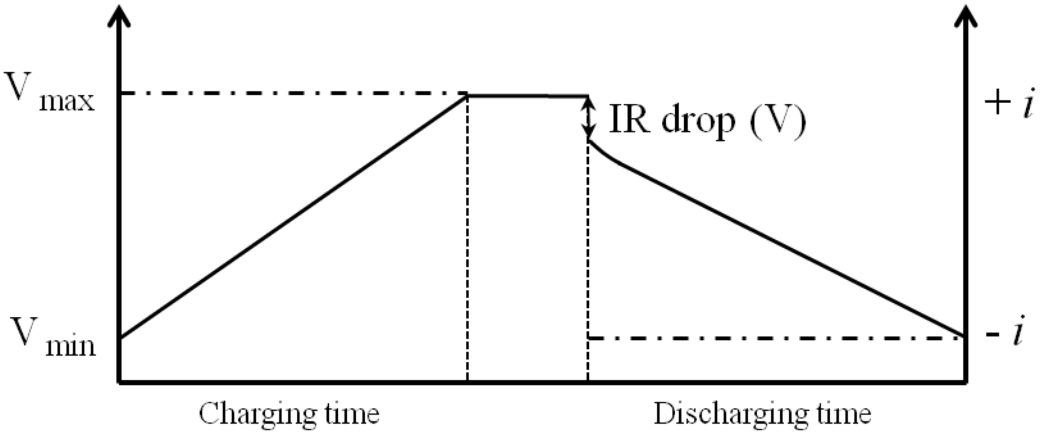

Figure 2.13 IR drop in CCD measurement due to an equivalent series resistance (ESR)

2.3.2.3 Electrochemical Impedance Spectroscopy (EIS) and Circuit Modeling

Previous sections explained how capacitance can be characterized by the response functions of the current to a variety of time-dependent changes in potential, or complementarily, changes in potential across a capacitance in response to a charging current. Another response function that characterizes electrochemical EC behavior is the alternating current generated in response to an alternating voltage as it changes with the frequency. The frequency-response characteristics of EC capacitance and resistance are generally dependent on (1) the intrinsic nature of the electrode material; (2) the pore-size distribution of the high-surface-area material used in the fabrication of the electrodes; and (3) the engineering parameters applied in the preparation of the electrodes, e.g., the configuration of the active electrode material and the nature of the particle-particle contact. The method called electrochemical impedance spectroscopy (EIS) not only enables capacitance ($Z'' = \frac{1}{j\omega C}$) values to be determined as a function of frequency but also provides quantitative information about the real ohmic component ($Z' = R$). The EIS method is especially valuable because it usually enables a separate evaluation of the frequency-independent ohmic resistance of a cell and the frequency-dependent resistance.

Impedance data for a typical EC is usually presented as a traditional Nyquist diagram of the small-signal impedance around a bias. Such EIS data is also used in electrical circuit analysis, and equivalent circuit models can be used for the interpretation of simple EIS data. Figure 2.14 shows a typical Nyquist diagram of an EDLC as well as examples of its equivalent circuit modeling.

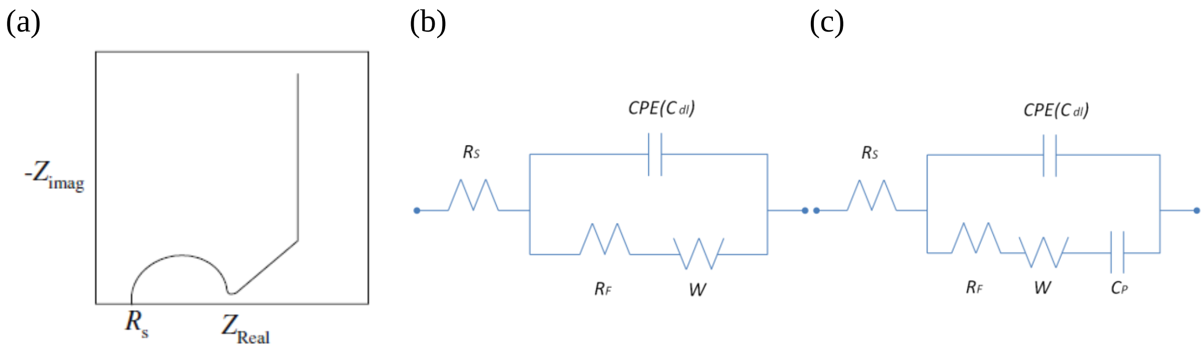

Figure 2.14 EIS data samples: (a) Nyquist plot of a typical EDLC. (b) example of equivalent circuit model for a pure EDLC. (c) example of equivalent circuit model for an EDLC that includes a pseudo-capacitance (Cp)

Table 2.3 Circuit elements used in the electric circuit models

Equivalent Element	Resistor	Capacitor	Warburg [a]	Constant Phase Element (CPE)[b]
Impedance	R	$\frac{1}{j\omega C}$	$\frac{1}{W_0\sqrt{(j\omega)}}$	$\frac{1}{Y_0(j\omega)^\alpha}$

[a]: $W_0 = 1/(\sigma\sqrt{2})$, and σ is the Warburg coefficient

[b]: $Y_0 = C =$ Capacitance, and α is generally less than 1

The elements used in the following equivalent circuits are presented in Table 2.3, and mathematical equations for impedance are given for each element.

As previously mentioned, EC systems cannot be characterized by expressing simple impedance behaviour as a function of frequency due to the porosity and/or complex electrochemical reactions of the electrode materials. As a result, as shown in Figure 2.14 (a), at high frequencies, the Nyquist curve consists of a semicircle, followed by a 45° inclination at modest frequencies and a vertical line at low frequencies. The first intersection point on the real axis of the Nyquist spectrum in the high-frequency region is represented as a series resistance (R_S), which is introduced in order to facilitate consideration of the resistance of the electrolyte and the contact resistance at the interface between porous electrodes and the current collector. Especially in the case of a porous or rough electrode surface, an arc can replace the semicircle, a possibility attributable to the rise of the constant phase element (CPE) in the high/middle frequency region [129]. In addition, the electrical double layer in the pores of the electrode is constructed because of the movement of the charge (electrolytic ions) as it diffuses toward the Helmholtz plane inside the pores. The semicircle is developed by the moving charges close to the Helmholtz plane and is represented by an interfacial resistance or charge-transfer resistance, called the faradaic resistance (R_F). Consequently, in the low-frequency region, the semi-infinite diffusion of ions can become significant for the determination of the diffusion impedance of a porous electrode. This impedance, created by the ion diffusion that occurs in a porous structure, is known as Warburg impedance (W) and usually appears as a straight line with a slope of 45°. At high frequencies, the Warburg impedance is small since the diffusing reactants do not have far to move. However, in a sufficiently low frequency range, the constantly decreasing frequency provides sufficient time for the charge-transfer complexes present in the diffusion layer to overcome the activation energy and move closer to the Helmholtz plane. This movement leads to an increase in the Warburg impedance [130]. The charges ultimately occupy all of the available surfaces inside the micropores of the electrodes and contribute to the electrical double-layer capacitance (C_{dl}). Therefore, the nearly vertical behaviour at low frequencies represents behaviour dominated by the capacitance in which the impedance can be reduced to a familiar term: $Z'' = \frac{1}{j\omega C}$. The phase angle of the impedance approaches 90°, with a near-vertical slope.

The above EC impedance characteristics can be represented by a relatively small number of electrical components when an equivalent circuit model is needed to describe the impedance behaviour of an electrode. Such a circuit model is shown in Figure 2.14 (b) as an example of the case of a pure EDLC in which a capacitor is in parallel with a Warburg impedance (W) associated with a Faradaic resistance (R_F) in order to account for the accessibility of the ions within porous structures and for surface functionalities or polarization resistance. If the contributions of the reduction and oxidation (redox) reactions of the surface functional groups that occur at the surface of the electrode cannot be neglected, the role of pseudocapacitance (C_p) should be considered [131, 132], as described in Figure 2.14 (c). This model structure is useful to provide the quantitative information on parameter variations with ease interpretation and simple simulation. However, limitations exist when these simplified circuit models, developed mainly to describe the electrochemical processes occurring at the interfacial layer, were used to explain the observed resistive and capacitive behaviors of practical EDLCs during experiments. As a result, the simulation results of these simplified circuit models deviated from experimental measurements in a practical device across its frequency range, especially at low frequencies. Worthwhile to mention, a recent model applied the multiple RC branches to account for the distribution of pores with a particular geometric structures for porous electrodes [133]. These examples, however, fail to clarify many of the details related to the definition of the transport of electrolyte ions; their electrochemical kinetics; and, in particular, the physical interpretation of equivalent EDLC circuits. Moreover, in a real EC system, multiple physical processes occur simultaneously: e.g., specific ion adsorption into pore sites and bulk electrolyte processes. An advanced equivalent circuit should therefore be correctly established based on a better understanding of each physical process and should include RC circuit branches to reflect the key electrochemical reactions in EC devices.

2.3.3 Thermal Characterization

The effects of temperature can be of major importance with respect to the practical evaluation of degradation, energy efficiency, lifetime, and the optimization of EC design for a variety of operating environments. Because the aging of ECs can also be accelerated by elevated temperatures, conventional accelerated aging tests are performed under a variety of temperatures. Many researchers have devoted considerable effort to the investigation of the temperature-dependent characteristics of ECs in which organic and solid electrolytes are used [134-138]. Liu et al. [135] and Iwama et al. [138] characterized commercial supercapacitors equipped with organic electrolytes for low-temperature operations. Hastak et al. [139] investigated the performance of AC-based EDLCs with solid electrolytes over a wider temperature range: 30 ℃ to 120 ℃. Although these reports provide valuable data and analyses that demonstrate the effects of temperature on supercapacitor performance, some limitations still exist. For example, little consideration has been given to the thermal effect on electrolytic ion characteristics, such as ionic diffusion and interfacial reaction rates. Publications include few studies [139, 140] whose goal was to develop an understanding of the temperature-dependent kinetic and diffusional behaviors of carbon-based supercapacitors involving organic electrolytes. However, to simplify the analysis, the reaction rate is usually assumed to be dependent only on the local difference in electrostatic potential between the electrode and the electrolyte, without consideration of the temperature-dependent movement of the ions into the pores, nor have many studies [137, 141] addressed the effect of porosity on the capacitive/resistive behaviour of carbon electrodes, especially with respect to their temperature-dependent characteristics. Such studies have been limited to the systematic verification of temperature-dependent electrochemical behaviour at double-layer interfaces and have neglected the effects of porosity on ion kinetics and diffusion reactions. Individual studies have also been focused on a specific individual electrolyte and have involved the implementation of different characterization methods, making a systematic comparison nearly impossible.

The thermal characterization of ECs is sensitive to the measurement method employed. Constant current discharging (CCD) is the most common test method for the evaluation of capacitance degradation, resistance variation, and cycleability, which is the same test used to evaluate batteries. The resulting capacitance degradation ratio is therefore shown as the ratio of the measured capacitance at each temperature to the capacitance at room temperature. A further consideration is that constant power (CP) discharging is preferable for EC cycle life tests rather than CCD measurement because, in practical use, the discharging current of ECs varies with a decrease in their voltage for constant power loads. In one study [142] researchers investigated EDLC temperature-dependent capacitance degradation and impedance trends under calendar life and power cycling tests. Another test method, EIS measurements, can be used to characterize capacitive and resistive behavior with respect to both frequency and temperature changes. Raik et al. [143] examined the measured and simulated capacitance and ESR of a commercialized supercapacitor (Maxwell BCAP0010), using separate frequencies for different temperatures, as shown in Figure 2.15. From these EIS measurements, it was found that capacitance is influenced by temperature primarily in the intermediate frequency range between 0.1 Hz and 10 Hz, while the ESR increases with a lower temperature in the low-frequency range.

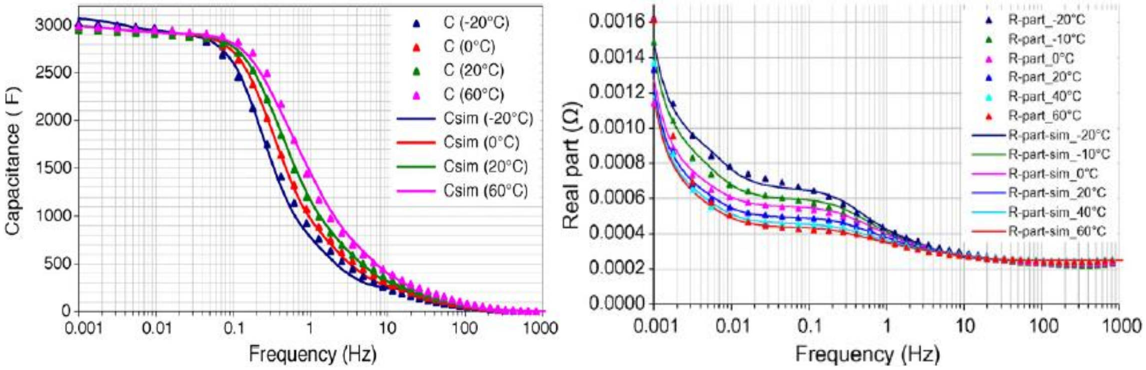

Figure 2.15 Capacitance and resistance frequency dependence of BCAP0010 for different temperatures [143]

2.3.4 Test Cell Configuration

Measurement methods for determining the performance of a material used in an EC are not well standardized, with numerous techniques currently being employed, which results in wide variations in the reported results. For this reason, when EC performance is evaluated, the measurement method should be identified, and the test methodologies selected should be capable of representing practical cells. A typical EC test cell is comprised of two electrodes that are isolated from electrical contact by a porous separator, as illustrated in Figure 2.16 (a). Because the performance of such a test cell configuration closely matches that of a real EC device, two-electrode cells are recommended for evaluating EC performance so that the results are comparable to those with actual devices. In a symmetrical two-electrode cell, the potential differences applied to each electrode are equal and are one-half of the values shown on the measurements. Therefore, for each electrode in a two-electrode system, the specific capacitance is as follows:

$$\mathrm{C_{sp}(F/g)} = 4 \times \frac{\mathrm{C}}{\mathrm{m}} \tag{39}$$

where m is the total mass of the active materials in both electrodes.

In electrochemical research, however, the common practice is to use three-electrode cells, which consist of a working electrode, a reference electrode, and a counter electrode, as shown in Figure 2.16 (b). This type of test cell configuration is valuable for analyzing the Faradaic reactions and maximum potential applied to a single electrode. With the three-electrode configuration, only one electrode, called the working electrode, contains the active materials being analyzed, and the voltage potential applied to the working electrode remains intact with respect to the reference electrode. The applied voltage and charge transfer across one electrode are therefore different from those in a two-electrode cell configuration. The working electrode of a three-electrode cell has twice the potential range of a two-electrode one, which results in a doubling of the calculated capacitance.

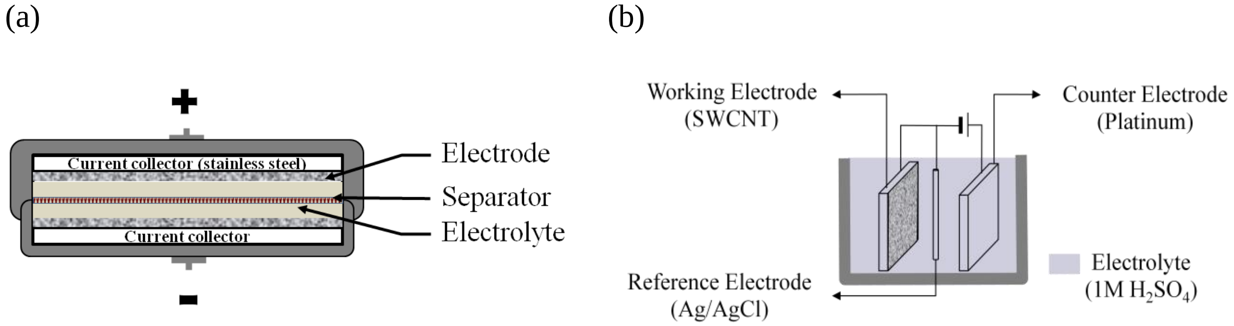

Figure 2.16 Schematic diagram of EC test cells: (a) two-electrode cell and (b) three-electrode cell

The charging rate, voltage ranges, and methods used for calculating metrics also affect reported results [144]. The measurement procedure selected should closely match currently established and accepted procedures used for packaged cells. The cell capacitance (C) is best determined from constant current charge-discharge (CCD) curves using equation (37). As described in section 2.3.2.2, CCD capacitance measurement is performed with the constant current charging and discharging at a constant current rate that corresponds to the ratio of the charge capacity being consumed within an hour. The CCD measurement is also the accepted method for determining the capacitance of packaged ECs used in industry. The same voltage range should be used for testing so that it matches the range used for commercial cells. It should also reflect the electrochemical window of the electrolyte, which ranges from 0 V to approximately 1 V for aqueous electrolytes and from 0 V to 2.4 V to 2.7 V for organic electrolytes. Another important factor is the necessity for the capacitance to be calculated using the typical operating voltage range for the application for which the device will be used. Most currently commercialized EC devices are operated in the range of V_{max} to approximately $\frac{1}{2}V_{max}$.

Chapter 3 Fabrication of Nano-Carbon Electrodes

3.1 Fabrication and Characterization of SWCNT Electrodes

Owing to its advantage of excellent electrical conductivity, remarkable chemical stability, large surface area and unique structures, a variety of carbon nanostructures including single walled (SWCNTs) and multi-walled carbon nanotubes (MWCNTs) have drawn much attention [145, 146]. Meanwhile, in order to fabricate high-performance CNT electrodes with more accessible pores, much research effort has been committed to produce CNT based electrodes with uniformly distributed and better accessible pore structures[147-149]. It has become really essential to develop an appropriate processing technology which is able to coat CNTs with right structural geometries (e.g., large surface area, uniform pores) and suitable for mass production. With these considerations, one of promising fabrication techniques for producing CNT coated electrode is the electrophoretic deposition (EPD) method, which is effective to control porosity, surface area and density of porous films [103].

The objective of the work presented in this thesis was to characterize the electrochemical properties of EPD-processed CNT coatings from suspension with different pH values. It was expected that the ions accessibility in CNT electrodes changes with the surface morphology and porous structures. The as-produced electrodes from various pH values would therefore exhibit distinguishable electrochemical properties. The second goal was to develop an equivalent circuit model for such SWCNT coated electrodes through measuring the cyclic voltammetry and electrochemical impedances of different coatings. This model is useful for later studies on characterizing of electrochemical properties of supercapacitors and recognizing complex electrochemical reactions in SWCNT electrodes.

3.1.1 Experimental

3.1.1.1. Preparation for Functionalized SWCNT Suspension

The SWCNT powder used in this work was supplied by Nano-C Inc. with a purity of 97%. The as-received samples were first acid functionalized using a mixture of nitric (HNO_3) and sulphuric (H_2SO_4) acids with a ratio of 3:1 (Sigma-Aldrich). 10 mL of this mixture was then added to 250 mg of the SWCNT powder and kept for 30 minutes to complete the carboxyl functionalization process [150]. During this process the –COOH functional groups were added to the defects and end sites of SWCNTs. This negatively polarizes the SWCNTs and allows them to disperse well in pure water without the use of additional surfactants [151]. The use of surfactants has been shown negatively affect the performance of CNT electrodes due to the remains of surfactants on the CNT's surface. After the functionalization the mixture was diluted with de-ionized water and washed through a filter to remove the residual acidic solution from SWCNTs. This process was repeated until the filtered SWCNT reached a pH of 7, then more de-ionized water was added and an aqueous suspension was produced with a concentration of approximately 0.5 mg SWCNTs/ml H_2O. In order to vary pH values of the derived SWCNT suspension, the pH value was adjusted by adding 1M sodium hydroxide (NaOH) or nitric acid solution (HCl) at room temperature (22 °C). These suspensions were then placed in a Branson 5210 Ultrasonic cleaner for 6 hours. Finally the suspensions were centrifuged at 4000 rpm for 15 minutes to remove undesirable particles and agglomerated SWCNT bundles. In each step of the filtration, centrifugation and decantation, the pH value was closely monitored using a PHH-830 meter and re-adjusted if necessary.

Finally, three suspensions with the pH values of 4, 7 and 10, respectively, were prepared and used in the EPD processing.

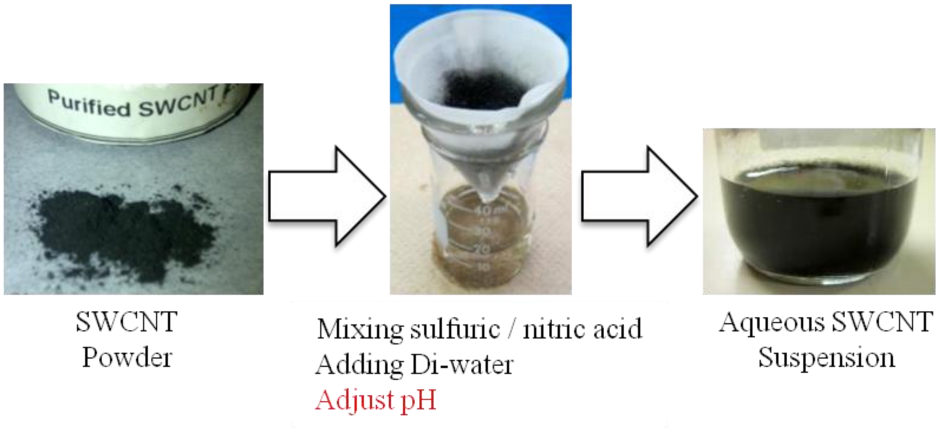

Figure 3.1 Images of functionalization processing for SWCNTs

3.1.1.2. Fabrication of SWCNT Electrodes using EPD and Measurements

The details on EPD processing of SWCNT suspensions can be found in the literature [107, 109] and here a brief description is provided. The SWCNT coated electrodes were fabricated with a working distance of 1 cm between two current collectors made in the stainless steel (SST, 70%Fe, 19%Cr, and 11% Ni: wt %, Alfa Aesar). EPD was carried out under a range of processing conditions including the deposition time between 3 and 30 minutes, room temperatures and three pH values. A DC power supply of 40 V was used. Through the previous research [97], it was determined that an EPD working voltage of 40 V was optimal for the fabrication of SWCNT electrodes. Voltages less than 30 V produced non-uniform coating and were slow to process, while above 50 V started to produce hydrogen bubbles on the electrodes from the hydrolysis of H_2O and disrupted the SWCNT coating. During EPD processing, the negatively charged SWCNTs move towards the positive electrode and uniformly coated the surface. Figure 3.2 shows a schematic diagram of EPD SWCNT coating process. In this work two types of SWCNT electrode was created. All electrodes were made with a rectangular area of 10 mm×10 mm×0.1 mm. The electrodes were finally dried on the hot plate for 30 minutes at 90 °C to remove moisture and solidify the SWCNT network.

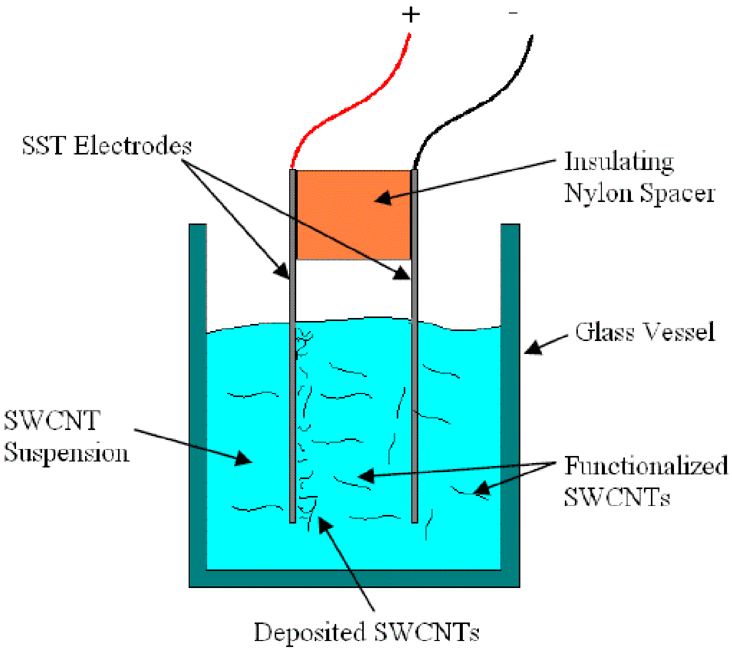

Figure 3.2 Schematic diagram of EPD SWCNT coating process

The surface morphology of the EPD processed SWCNT film was characterized by a field emission scanning electron microscope (LEO 1530 FE-SEM) for visualizing the micro-porosity. The electrochemical properties of these electrodes were evaluated using the cyclic voltammetry (CV) measured by a Gamry Reference 3000 Potentiostat within a potential range of -0.2 to 0.8 V at the scan rate of 20 mV/s. Electrochemical impedance spectroscopy (EIS) was performed on the same Potentiostat using the EIS 300 software. The frequency range was set from 0.1Hz to 100 kHz. All CV curves and EIS data were measured in three-electrode cell to verify the faradaic reactions and resistance elements inside a single electrode. The cell includes the working (SWCNT coated), counter (platinum) and reference (Ag/AgCl) electrodes. An aqueous 1 M H_2SO_4 solution was used as the electrolyte in the cell at room temperature. In order to determine the surface area and pore-size distributions Nitrogen adsorption measurements at 77K were performed using a Micrometitic Flowsorb surface area analyzer. This analyzer quantifies the Brunauer-Emmett-Teller (BET-N_2) surface area and Barrett-Joyner-Halenda (BJH) pore sizes distribution. More specifically, the specific surface (S_{BET}) was derived from the BET theory when the relative pressure (P/P_0) of nitrogen was set up to 0.3. The pore size distribution was determined by the same adsorption procedure from the gas adsorption isotherms. It has been well received that from the literature, for samples possessing a pore size range of 2 nme50 nm, the BJH method is quite accurate. The total volume of pores (V_{tot}) was obtained by summing up the adsorption pore volume up to the saturation pressure $P/P_0 = 0.99$. The pore surface area was then calculated by the measured BJH pore size.

3.1.2 Results and Discussion

3.1.2.1 Influence of pH Values of the Suspension to EPD

The effect of different pH values on the SWCNT suspension is visible and shown in Figure 3.3. As mentioned earlier, all three suspensions were prepared from the same sample with the concentration of 0.5 mg SWCNTs per 1 ml of water. Then an extra amount of NaOH or HCI was added in order to reach different pH values in the suspension. It was expected that the higher pH value produced more negatively charged SWCNTs in the suspension, and consequently SWCNTs are dispersed homogenously in higher pH conditions. Finally these samples were processed using the ultrasonic cleaner and larger agglomerates were filtered out. This sample preparation procedure resulted in different appearances and concentrations of SWCNTs in three suspensions.

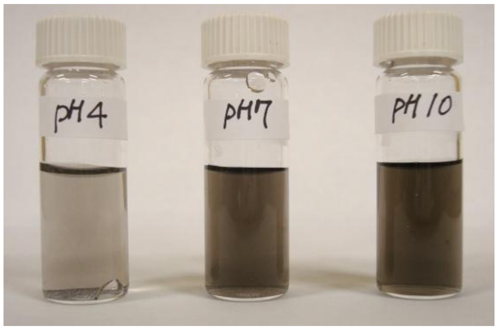

Figure 3.3 Photographs of SWCNT suspensions at pH4, 6 and 10, respectively

In general, the suspension with a lower pH value (such as pH = 4) contains less charged individual tubes and more nanotube agglomerates, and the total quantity of CNTs in this suspension is small. In contrast, the suspension with a higher pH value (e.g., pH = 10) contains less agglomerates and more individual nanotubes owing to higher surface charges (Zeta potential). The observation in Figure 3.3, in agreement with the previous studies [152, 153], reveals the higher pH values facilitate the better dispersion of SWCNTs, which can be attributed to an easier ionization of the carboxylic (COOH) group in these suspensions with large pH values. When the pH value is increased by adding hydroxide (OH-) (refer to Figure 3.4), the more carboxylate (-COO-) groups were obtained on the surface, the heavier charging of individual tubes was achieved, which led to the more effective dispersion of

SWCNTs. Consequently after filtering, the higher pH suspension has the greater concentration of dispersed SWCNTs in it.

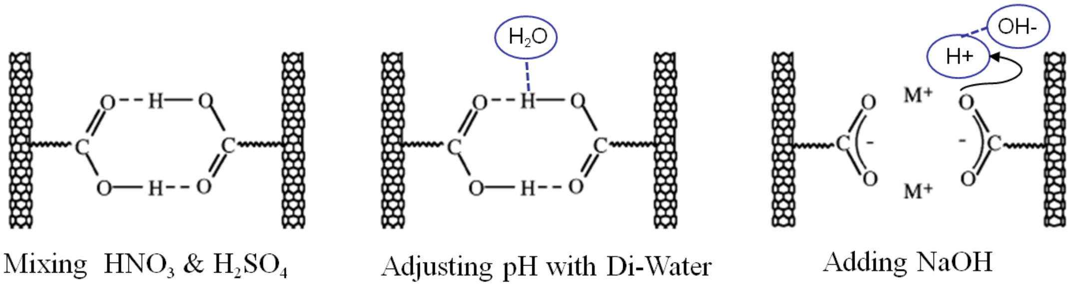

Mixing HNO_3 & H_2SO_4 Adjusting pH with Di-Water Adding NaOH

Figure 3.4 Schematic explanations for highly charged SWCNT by increasing pH values

In addition, the previous studies [112, 150] suggested that, the electrophoretic mobility and surface charges of acid-treated CNTs increase with the increasing pH value. These parameters, together with the quantity of available SWCNTs in the suspension, undoubtedly affect the deposition rate of the EPD process.

Using the suspensions with different pH values, SWCNT coated electrodes were fabricated by the EPD process at room temperature and with controlled processing times. The optical images of these as-produced electrodes showed that for the same processing time, the electrodes processed at higher pH values are much darker than other electrodes at lower pH values, and they also have a greater coverage and better uniformity. The microstructures of these electrodes were further examined using FE-SEM. Figure 3.5 shows the FE-SEM images of SWCNT networks obtained from suspensions with different pH values and for two processing times, 3min and 30min, respectively. The inserted figure shows a high-resolution SEM image of individual tubes obtained from a shorter processing time (30 seconds). In general, increasing the processing time produces thicker SWCNT films on the substrate and deposit more material as the electrode [97, 154]. For the processing time of 3 minutes as described in Figure 3.5 (a), the pH 4 suspension produced less material on the substrate while more individual SWCNTs were deposited in the pH 10 suspension.

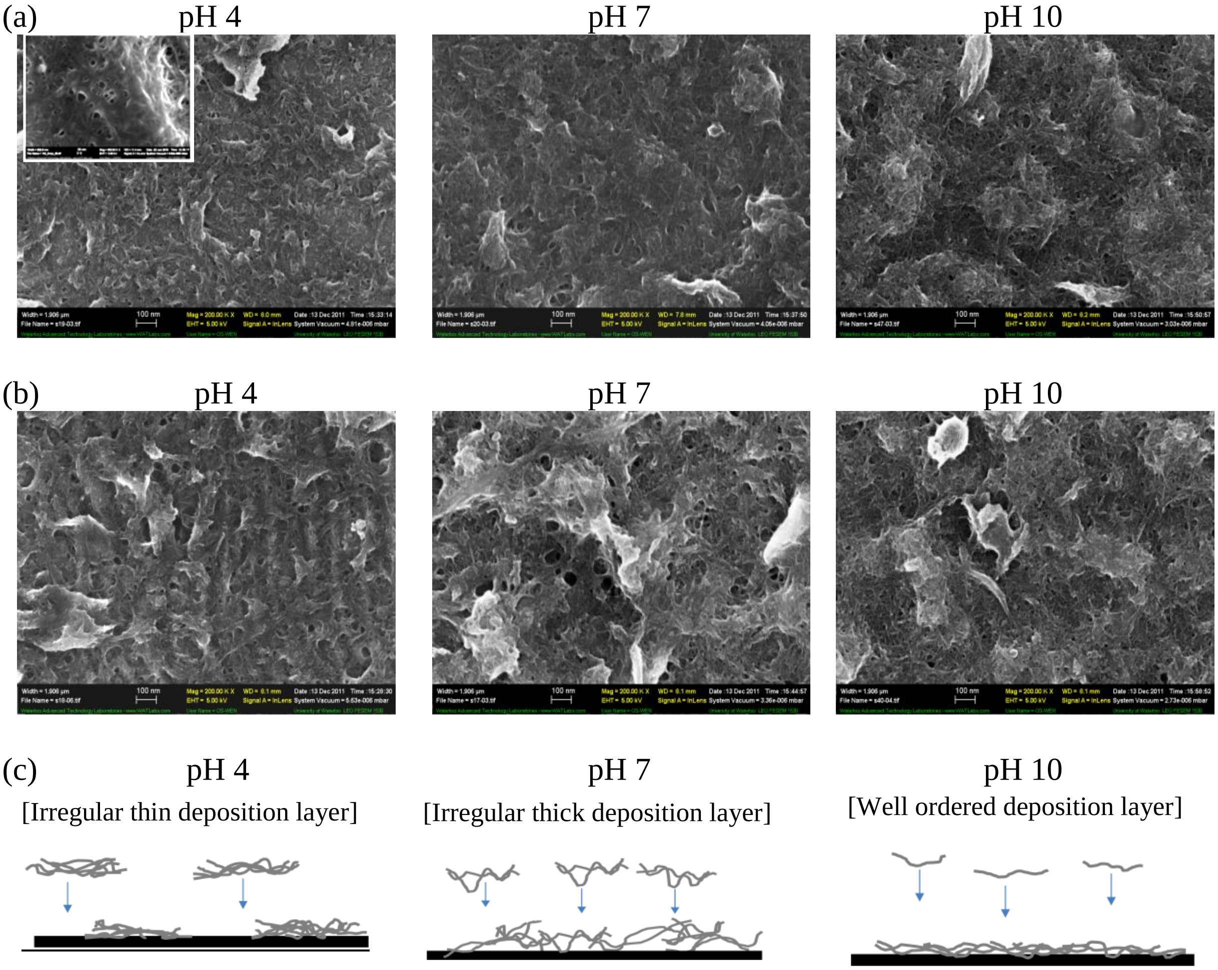

Figure 3.5 FE-SEM images of SWCNT electrodes processed from suspensions with different pH values and with the EPD period of (a) 3min, (b) 30min, respectively. (c) The qualitative illustration of the deposition mechanisms with varying pH values

In addition, for this short processing time of 3 min, the difference in surface morphology from various pH suspensions was insignificant due to a limit amount of nanotubes deposited on the substrate. The SEM images, from Figure 3.5 (a) for pH 4 and pH 10, however, still show the distinguishable appearance of these microstructures formed from EPD. On the pH 4 image, there are obviously many flakelet structures which were formed from the deposition of nanotube bundles, due to in-sufficient dispersion of individual nanotubes under low pH conditions. On the pH 10 image, however, the nanotubes and bundles are clearly observed directly on the electrode, which confirms a better deposition resulted from a satisfying dispersion of individual tubes with a higher pH value.For the processing time of 30 minutes (Figure 3.5 (b)), micro-structures of CNT bundles appeared on all three samples but the pH 10 suspension produced more individual tubes and a smoother surface morphology. Figure 3.5 (c) explains the deposition mechanism of SWCNTs in these suspensions with different pH values. For the pH4 suspension, more agglomerates exist and the deposition happens by carrying with larger bundles, which causes the formation of irregular microstructures on the substrate. Moreover, the less material available in the suspension results in a slower deposition rate and brings about less deposited material. For the pH 10 suspension, more individual tubes exist in the suspension and their surface charging levels are higher. This situation results in a larger deposition rate and a well ordered deposition film is produced. For the pH 7 suspension, the situation becomes a bit complicated due to the availability of bigger agglomerates in the suspension and the faster deposition rate of such structures. More micro-structures were observed on the coating and the morphology became less organized. The similar finding was reported in EPD processing of SiO_2 films [155]. Well dispersed particles were found in the higher pH value suspensions and more uniform films with the low surface roughness were produced. In contrast, unstable suspensions with low pH values could not produce thick films due to sedimentation. With a moderate pH values particle agglomerates in EPD processing yielded a high surface roughness.

It is important to quantify the effects of the pH value on the EPD deposition rate. In literature [98], the kinetics of EPD processing was described by Hamaker's law given by

$$\omega = \int_{t2}^{t1} f\,\mu EAC\, dt \tag{40}$$

where the deposition rate (ω) is expressed as a function of the concentration of charged particles in the suspension (C), the electrical field strength (E), the electrophoretic mobility (μ), the area for deposition (A) and a constant f. The electrophoretic mobility, which depends on both the properties of particles and the liquid, can be calculated by

$$\mu = \frac{\varepsilon \varepsilon_0 \zeta}{\eta} \tag{41}$$

where ε is the dielectric constant of the liquid, ε_0 is the vacuum permittivity, ζ is the surface charge of the particles, and η is the viscosity of the liquid. Equation (41) shows the strong dependence of the electrophoretic mobility on the surface charge of suspending SWCNTs. The suspension with a higher pH value contains CNTs with more surface charges and hence exhibits a better electrophoretic mobility. In addition, the concentration of charged nanotubes is higher in this suspension. Both factors, according to equation (40), will accelerate the EPD deposition rate in suspensions with high pH values.

3.1.2.2 Electrochemical Characterization of SWCNT Electrodes

Cyclic voltammetry (CV) graphs of these SWCNT coated electrodes derived from different pH suspensions are shown in Figure 3.6. Note that the scale of the y axis in figure 6

(a) is close to half of that of (b). These figures show that the bumped regions are less significant for electrodes produced from lower pH values, due to less surface charging (and less carboxylate groups) of the SWCNTs. Up to 30 minutes, the pH 10 suspension produced the largest area enclosed by the CV curves. For the pH 7 and pH 10 cases, the bumped regions, which are attributed to the pseudo-faradaic reactions caused by the carboxylate groups [132, 156], have been larger corresponding to the following reactions:.

$$-\mathrm{COOH} \Leftrightarrow -\mathrm{COO} + \mathrm{H}^{+} + \mathrm{e}^{-} \qquad (42)$$

$$>\mathrm{C}=\mathrm{O} + \mathrm{e}^{-} \Leftrightarrow\ >\mathrm{C}-\mathrm{O}^{-} \qquad (43)$$

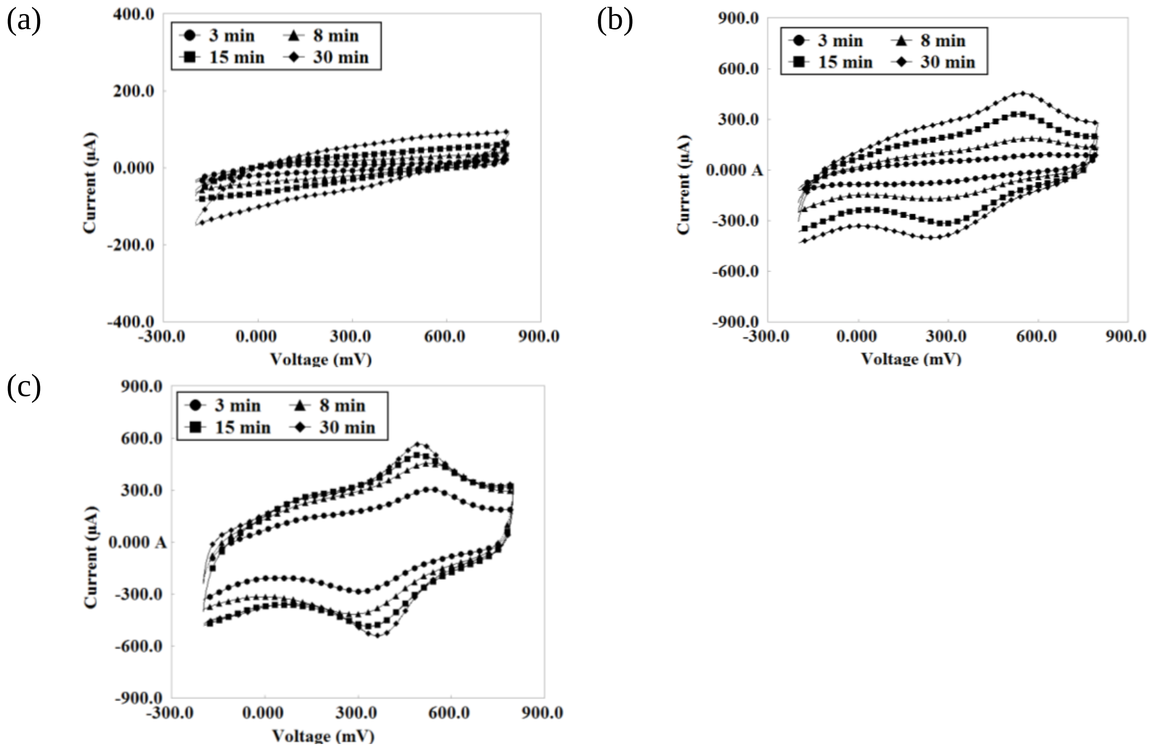

Figure 3.6 Cyclic voltammograms of SWCNT electrodes, in 1M H_2SO_4 with various pH values (a) pH4, (b) pH7 and (c) pH 10

From the CV graphs reported in Figure 3.6 the specific capacitances were calculated in regard to the geometric area (1 cm^2) of the electrode. The results are shown in Figure 3.7. The SWCNT coated electrodes derived from the pH 10 suspension exhibit the highest capacitance (mF/cm^2) for all processing times ranging from 0 to 30 minutes. The value of specific capacitance increases much faster for the pH 10 suspension, compared to two other suspensions. The pH 4 curves show the lowest specific capacitances with less pseudo-Faradaic effects in Figure 3.5 (a). The behaviors of different electrodes were expected from the distinct EPD rates and the different amounts of deposited material on the electrodes from various suspensions.

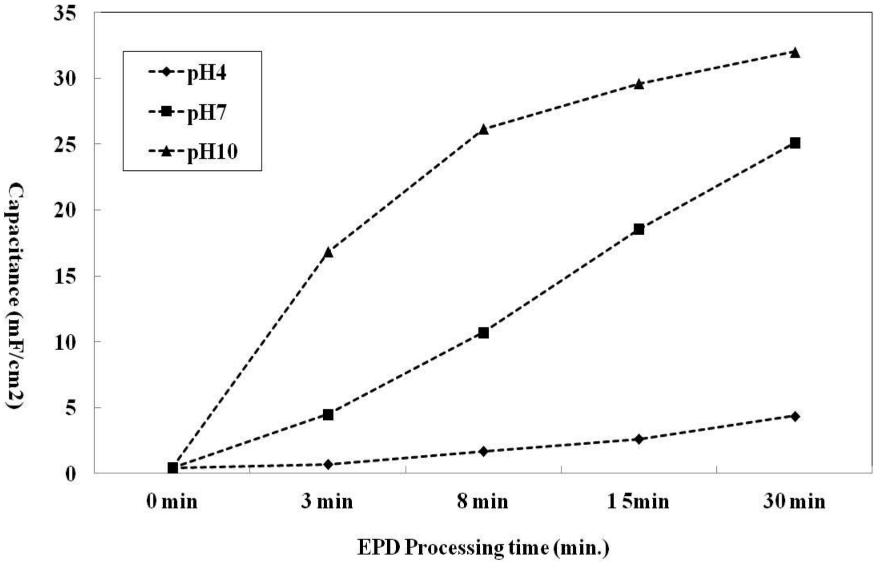

Figure 3.7 The dependence of the capacitance (evaluated by CV) on the EPD processing times for varying pH values

As mentioned earlier, there is a strong correlation between the specific surface areas of carbon nanostructures and their specific capacitances. The BET measurements were carried out in order to assess this relationship. For SWCNT electrode with various pH values, all measurements were done for different pH samples with the same EPD processing time of 30 minutes. Table 3.1 summaries the BET specific surface areas, pore volumes and average pore diameters obtained for three pH values. With increasing the pH value, the specific surface area of SWCNT network increases; whereas, the average pore diameter decreases. The electrode derived from the pH 10 suspension shows the highest BET surface area (820 m^2/g) and the smallest pore size (2.7 nm).

Table 3.1 BET surface areas, pore volumes and average pore diameters of SWCNT electrodes processed with different pH conditions

Sample (pH)	BET Surface area (m^2/g)	Pore volume (cm^3/g)	Average pore diameter (nm)
pH 4	601	0.32	4.2
pH 7	642	0.425	3.9
pH 10	820	0.629	2.7

Figure 3.8 plots the increasing trends of the specific capacitance and the surface areas for three pH cases, and these two parameters do not show a linear interdependence. This implies the essential role of pore accessibilities in ion transportation and storage [26].

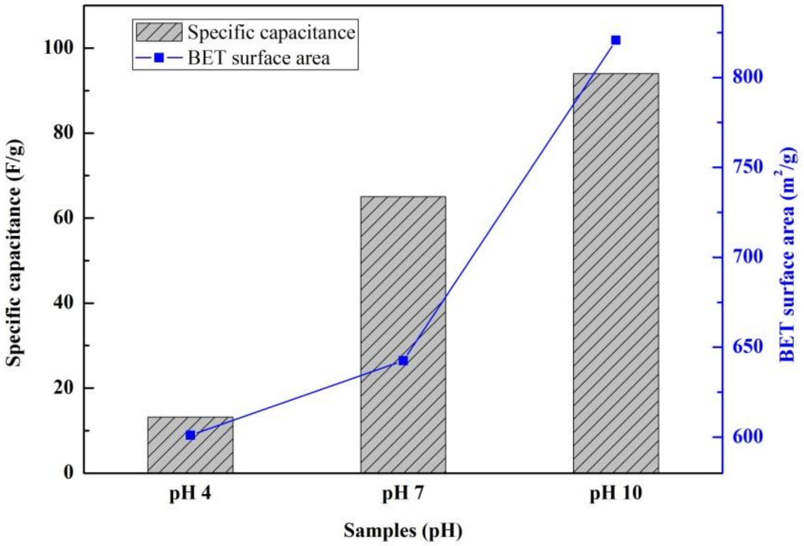

Figure 3.8 Specific capacitance (F/g) and BET surface area of SWCNT electrodes fabricated with different pH values

In order to investigate the contribution of the pore accessibility to specific capacitance, the pore volumes (also shown in Table 3.1) and pore areas of SWCNT networks on three electrodes were measured from nitrogen adsorption using the BJH method. The data are plot in Figure 3.9 against the average pore diameter. As shown, the pore surface area is greater for the electrodes fabricated from the larger pH values. For the pore volume, there are distinctly two regions which can be observed in Figure 3.9 (b). For smaller pores with their diameters less than 4 nm, the pH10 electrode has the largest number of such pores, while for larger pores with their diameters greater than 4 nm, the pH 4 electrode has the largest pore number. In comparison with Figure 3.8 which shows the pH 10 electrode has the largest specific capacitance, it can be concluded that the availability of larger pores in the wide size range (5-50 nm) do not significantly affect the specific capacitance, while the accessibility to smaller pores, corresponding to the average pore diameter below 4 nm, is dominant in determining the specific capacitance.

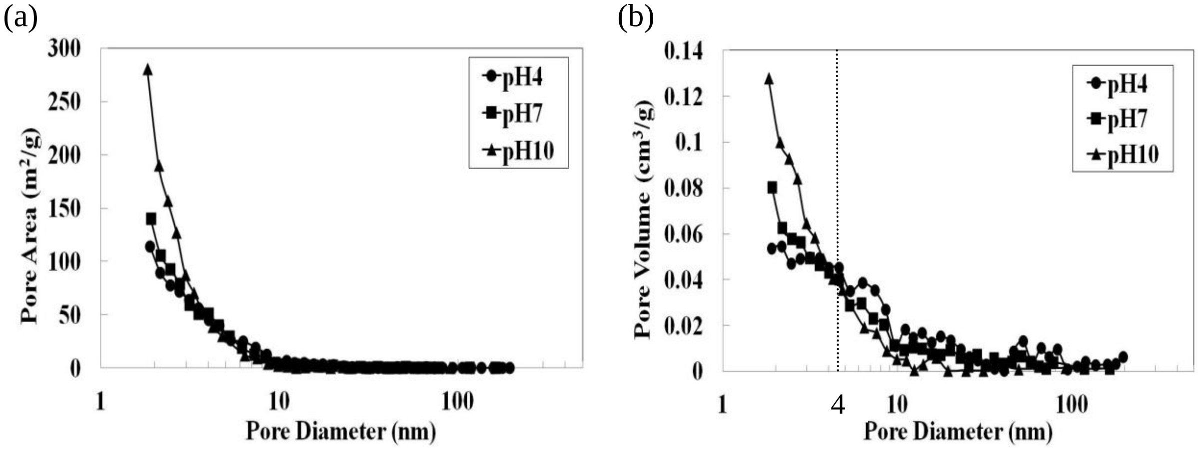

Figure 3.9 Pore size distributions of SWCNT electrodes fabricated with different pH values: (a) Pore area and (b) Pore volume

This complicate dependence of the accessibility to small pores on the pH value of the EPD suspensions result in a non-linear relationship between the specific capacitance and the specific surface area. Note that the pore accessibility depends not only on the pore distribution on the electrode but also on the type of electrolytes. In this study, the optimum pore sizes for these EPD processed SWCNT electrodes are between 2 - 4nm and lead to the highest ion accessibility. More investigations are expected for characterizing the optimum pore size for other types of electrolytes such as organic or non-aqueous ones.

3.1.2.3 Electrochemical Impedance and Equivalent Circuit Modeling

Using the EIS 300 software (Gamry Ins.), the Nyquist plots were made for the SWCNT coated electrodes fabricated from these suspensions with three pH values. 1M H_2SO_4 was used as the electrolyte and the measurements were performed for two EPD processing times of 3 minutes and 30 minutes, respectively. Figure 3.10 (a) and (b) show the Nyquist plots of 3 min electrodes in the entire range of tested frequencies ranging from 0.1 Hz to100 kHz.

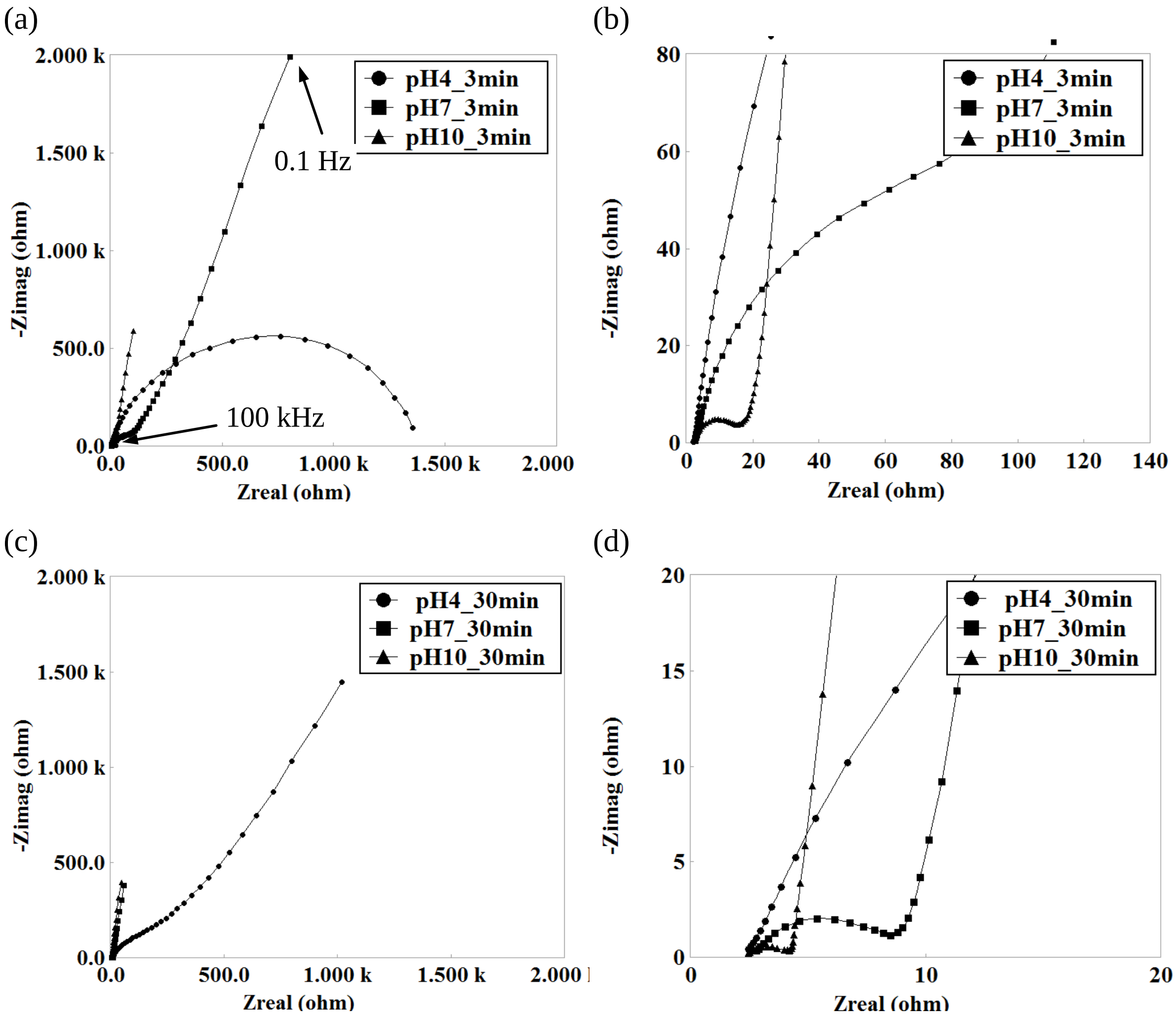

Figure 3.10 (a) Nyquist plots for the SWCNT electrodes with different pH values at EPD processing times, 3 min., and (b) enlarged sections of the Nyquist plots at high frequency. (c) Nyquist plots for the SWCNT electrodes with different pH values at EPD processing time of 30 min. (d) enlarged sections of the Nyquist plots at high frequency for (c)

The zoomed figure emphasizes the high frequency zone. On these plots, the diameter of semicircle is referred as R_F while the high frequency intercept on the Z_{real} axis represents the sum of R_S. The pH4 electrode shows an almost complete semicircle which reveals a less porous electrode after the short EPD processing time of 3 minutes. On the other hand, both pH 7 and pH 10 electrodes show a part of arc followed by a straight line showing a sharp increase in the imaginary part of the impedance at lower frequencies, which are representative of ion diffusion dominant processes. Especially the pH 10 electrode shows its linear EIS performance over a wider range of frequencies. It is also noticed that the relatively large values of R_F exist for the lower pH value electrodes. This is attributed to the poorer accessibility of ions to the pores on the electrodes fabricated from lower pH suspensions. Figure 3.10 (c) and (d) show the Nyquist plots of 30 min electrodes. In comparison with the similar observations in Figure 3.10 (a) and (b), both the pH 7 and pH 10 electrodes show very large capacitances at high frequencies.

Table 3.2 Proposed equivalent circuit models for SWCNT electrodes fabricated from different pH values

Equivalent circuit for SWCNT electrodes	
Model 1	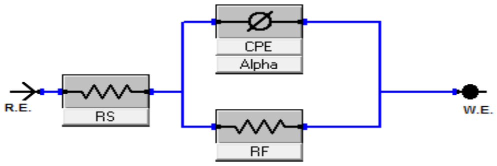
Model 2	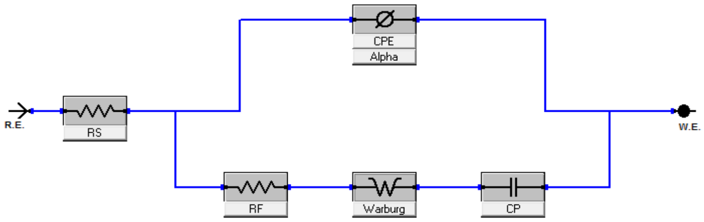

Using the measured EIS data and adapting the equivalent circuit model shown in Table 3.2, the values of C_P, R_S and R_F were fitted into the Nyquist curves. Also, the impedance of a CPE can be represented as defined below:

$$Z = \left(\frac{1}{Y_0}\right)/(j\omega)^{\alpha}, \qquad 0 < \alpha < 1 \tag{44}$$

For a double layer capacitor, the constant Y_0 indicates the capacitance and the exponent α is less than 1. Figure 3.11 (a) and (b) show the comparisons between the Nyquist plots and the plots of the derived equivalent circuit models. Table 3.3 summaries the values of three parameters determined from different electrodes. Note that the C_P values of the pH 4 electrodes are extremely small due to very limited amount of surface charges on the electrode (and less pseudo-Faradaic effect). The pH 10 electrodes with 30 min processing time show the largest C_P, which shows the existence of the pseudo-capacitance. It can be seen that R_F decreases as increasing the pH value of the suspensions, while Rs slightly increases. This can be explained using the pore distributions shown in Figure 3.9. The SWCNT coated electrode from the high pH value exhibits a lower R_F because it possesses a better electrolyte's accessibility to pores in the range of 2 - 4 nm.

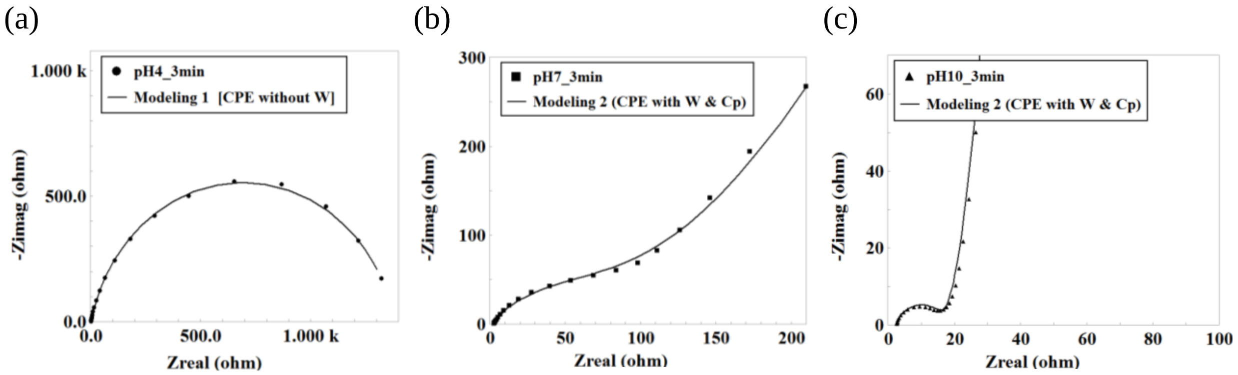

Figure 3.11 Correlation between Nyquist plots with different pH values: (a) pH 4, (b) pH 7, (c) pH 10

Table 3.3 Equivalent circuit parameters (C_P, R_S & R_F) obtained from the modeling results

	3 min				30 min		
	C_P	R_S	R_F	α	C_P	R_S	R_F
pH 4	-	2.1	1351.3	0.861	$1.6e^{-7}$	2.2	177.3
pH 7	$9.6e^{-4}$	2.4	74.6	0.81	$3.4e^{-3}$	2.4	5.5
pH 10	$2.9e^{-3}$	2.4	11.8	0.794	$4.6e^{-3}$	2.5	1.5

The contact resistance Rs at the interface may increase due to more micro-structures formed on the electrode. These observations suggest that, as the pH value increases, the sharp increase of the imaginary part of the impedance resistance appears at lower frequencies and extends to the entire frequency range. In addition, the SWCNT networks fabricated from higher pH suspensions show their larger specific capacitances which are attributed to more effective pore volumes. Moreover, pseudo-capacitances (C_p) were found important on these electrodes fabricated from higher pH suspensions. As increased pH value, the surface functionalization group contributes more pseudo-capacitance.

3.1.3 Summary

SWCNT coated electrodes were fabricated from functionalized CNT suspensions with various pH values using the electrophoretic deposition method (EPD). EPD processing at higher pH values yields SWCNT electrodes with increased surface area and more effective pore volumes, while both contributed to the increase in the specific capacitances of these electrodes. The measurements of electrochemical impedance resistance revealed the rapid increase of the imaginary part of the impedance resistance when the electrode was fabricated with higher pH. The finding from the equivalent circuit model further confirmed that the higher pH treatment is desired not only to reduce the SWCNT electrode resistance (R_F) but also to introduce a complementary effect of pseudo-capacitance. In addition, the optimized pore size distribution through modifying pH values could enhance the performance of SWCNT electrodes. Moreover, the decrease of the internal resistance was achieved when desirable nano-structured electrodes were fabricated from the EPD process. This investigation of impedances of SWCNT electrodes fabricated from functionalized suspensions with different pH values will help optimize their electrochemical properties for designing high energy density devices.

3.2 Fabrication of Activated Carbon Electrodes

For the fabrication of EDLC-typed cells using porous electrodes, activated carbon (AB-520, from MTI corp. in USA) with high specific surface area (2000 m^2/g as a powder) was used to produce active electrode films on a current collector. The activated carbon-based paste was prepared by mixing activated carbon (AC), polytetrafluoroethylene (PTFE from Aldrich) as a binding agent, and carbon black (from Alfa Aesar, with a surface area of 80 m^2/g) as a conductive agent in a mass ratio of 90:5:5 using the solvent, N-Methyl-2-pyrrolidone (NMP from MTI corp.), and then this paste was cold-rolled on a stainless steel (SST plate of 1mm thickness from Alfa Aesar) current collector. After coating activated carbon-based pastes, the electrode was placed into a vacuum oven at 90 ◦C for 12 h to remove moisture and solidify the film. The specifications for a single electrode are summarized in Table 3.4. A coin-typed cell (2032 coin cell from MTI Corporation) with identical two-electrodes was then built by assembling each AC electrode, separated by a 25 µm thick Celgard 2400 membrane. To compare different electrolytes, 1 mole organic (Et_4NBF_4 from Alfa Aesar) salts in propylene carbonates (PC from Sigma-Aldrich) and 1 or 3 mole aqueous (H_2SO_4) electrolytes were prepared.

Table 3.4 Typical specifications for a single electrode made of activated carbon

Diameter of an electrode	9/16 " (14.28 mm)
Active a of area	1.6 cm^2
Total mass of an electrode (including a current collector)	0.1713 g
AC film (Only)	0.012 g
AC film thickness	0.15 ~0.20 mm
BET specific surface area	2000 (±100) m^2/g (Activated carbon powder)

3.3 Fabrication of Graphene and SWCNT Electrodes using Vacuum Filtration

The practical evaluation of material performance in EC devices is only valid for electrodes with thickness and weight similar to those of commercial electrodes (recommended a thickness of 100 to 200 µm or a weight of about 10 mg/cm^2) [157]. However, SWCNT electrodes produced from EPD method, as described in section 3.1, possess the thickness of about 20 µm and the limited weight up to 3 mg/cm^2. To overcome these limitations, SWCNT and graphene-based electrodes were prepared using the vacuum filtration deposition (VFD) method. Commercial SWCNT (as received from Nano-C Inc.: 1.2 nm in diameter, 1.4 to 1.5 µm in length) and graphene nanoplatelets (as received from XG science: 1 to 50 µm in width, 1 to 20 nm in thickness, Grade C) were used for fabricating nano-structured electrode film on a current collector. Carbon powders in as-received condition were mixed with the condensed PTFE in water, as a binder, with a weight ratio of 4:1 wt. % in absolute ethanol, as a solvent. This suspension was subjected to intensive ultrasonification for 1 h in order to create a homogeneous mixture.

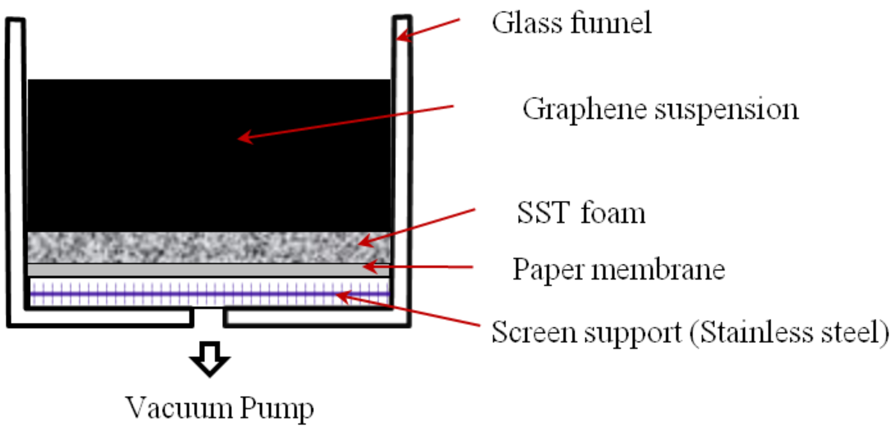

Figure 3.12 Schematic of vacuum filtration deposition process

As illustrated in Figure 3.12 , the resulting suspension, with a concentration of 1 m/ml, was then decanted and vacuum filtrated through stainless steel (SUS) foam from Nagamine Manufacturing Co. Ltd., with a thickness of 1.0 ± 0.2 mm, porosity of 84 %, and an average pore diameter of 160 μm. The carbon film deposited on the SUS foam as a current collector was dried at 60 ℃ for 24 h in order to remove the ethanol solvent and to solidify the electrode film. The final step was to assemble two pairs of each electrode in a 2032 coin cell, separated by a 25 μm thick Celgard 2400 membrane and immersed in 1 mole Et_4NBF_4/PC electrolytes. Table 3.5 summarizes the specifications for each unit cell. All these cells were assembled in a glove box filled with pure Ar gas. Since the chemical-electrical properties of the organic electrolyte can be changed by water vapor, a special care was taken during assembling to ensure the humidity in the glove box is less than 9 % RH.

Table 3.5 Typical specifications of a single electrodes made of graphene and SWCNT

Current collector (SST foam)	Diameter / Thickness	15 mm / 1.2 mm
	Average pore diameter	160 μm
	Porosity	85 %
Carbon electrode	Active area	1.6 cm^2
	Mass	12 ~ 15 mg
	BET specific surface area (measured with powders)	750 m^2g^{-1} (Graphene) 400 ~ 1,000 m^2g^{-1} (SWCNT)

Chapter 4 Development of an Equivalent Circuit Model

4.1 Introduction

For energy storage systems, e.g. batteries, fuel cells, electrochemical capacitors (EDLCs) or hybrid systems in electric vehicles, wind and solar power generation [158-161] , it is very important to obtain an accurate circuit model which describes the operation characteristics of EDLCs, and subsequently to optimize the component sizes and design in different applications. Meanwhile, equivalent circuits for EDLC modeling are valuable to predict their dynamic behaviors within a power electronic circuit. Moreover, it provides meaningful information to understand critical reactions at the double-layer interfaces.

In this work, a new equivalent circuit model with multiple-RC elements (for accounting for diffusion, adsorption and bulk media impedance, respectively) is proposed from the observed physical and electrochemical phenomena. This is aimed to develop a more adequate equivalent circuit model by considering the effect of the electrolyte on ions' transportation (ionic diffusion and migration), adsorption layer formation on electrode surface, and bulk processes in practical EDLC systems. It is expected that this circuit model can be used to interpret resistive and capacitive behaviors of an EDLC device, and quantitatively to verify the contribution of individual processes to device's performance.

4.2 Circuit Model Development

As discussed in Chapter 2, a few theoretical treatments of EDLC structures have schematically proposed to describe the properties of the double-layer at electrode/electrolyte interfaces. The first concept of EDLC structures was introduced as the compact of Helmholtz layer [31], where all counter-ions were assumed to be attracted to the charged electrode surface. This model is analogous to that of conventional dielectric capacitors with two metal planar electrodes. Therefore, the capacitance in Helmholtz model is simply expressed as follows:

$$C_H = \frac{\varepsilon_0 \varepsilon_r}{d} \cdot A \tag{45}$$

where ϵ_0, ϵ_r are the free space permittivity and the relative permittivity of the electrolyte, respectively. The distance of Helmholtz layer, *d*, can be obtained from the radius of solvated ions (refer to Figure 4.1), while *A* is the surface area of the electrode.

Another theoretical description of the EDLC has been developed by Guoy and Chapman [32, 34], which is considering into the diffuse part of the double-layer. This model treats the ions as point charges so that the ions' movements in the electrolytes are driven by the influences of diffusion. This ions transportation in EDLC determines the overall capacitance. It is subjected to applied potential, thermal fields and types of ions in the electrolyte. In the Guoy-Chapman theory, the diffuse charge is determined by the Poisson-Boltzmann equation. This equation is given for a symmetrical electrode as follows:

$$q_d = \left(\frac{2kTn_0\epsilon}{\pi}\right)^{1/2} sinh\,\frac{e_0 V}{2kT} \tag{46}$$

Therefore, the specific capacitance according to the diffuse layer, C_{diff}, can be evaluated as

$$C_{diff} = \frac{\partial q_d}{\partial V} = \left(\frac{n_0 \epsilon\, {e_0}^2}{2\pi kT}\right)^{1/2} cosh\,\frac{e_0 V}{2kT} \tag{47}$$

where n_0 is the number of ions in the bulk electrolyte, *V* is the potential drop between the electrode and the bulk electrolyte, e_0 is the charge of the ion, *k* is the Boltzmann constant, *ε* is the dielectric constant in the electrolyte**,** and *T* is the temperature.

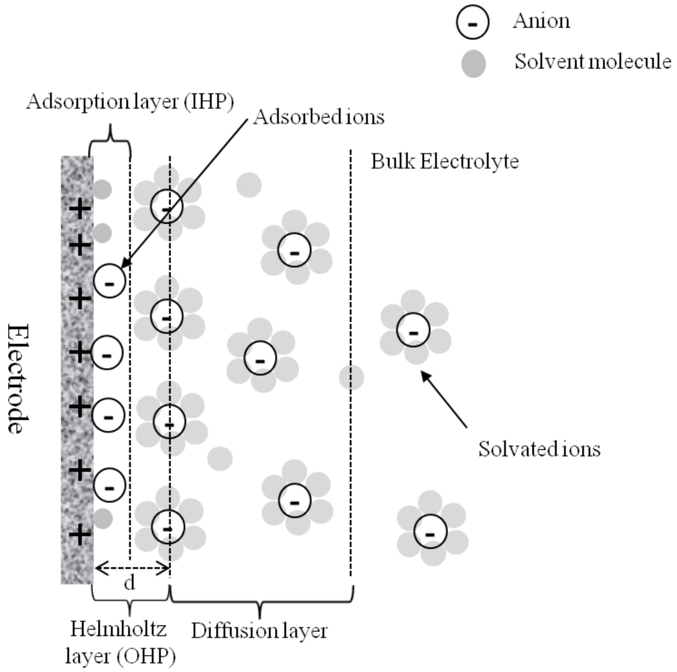

Figure 4.1 Schematics of an electrochemical double layer and the electrode/electrolyte interfaces model

And later, the diffusion layer model was combined with the Helmholtz model by Stern [33]. In that model, the overall capacitance in EDLC, C_{dl}, was considered as a series of capacitance, C_H and C_{diff},

$$\frac{1}{C_{dl}} = \frac{1}{C_H} + \frac{1}{C_{diff}} \tag{48}$$

In further developments, Graham [42] emphasised the presence of specific adsorption of ions on the electrode surface, by modeling three distinguished layers: the inner Helmholtz plane (IHP), the outer Helmholtz plane (OHP) and the diffusion layer (see Figure 4.1). The IHP region is made of solvent molecules and/or adsorbed ions (cations or anions in electrolytes) while the OHP region corresponds to the formation of hydrated ions (solvated ions) layer. Subsequently, the diffusion layer develops outside the OHP. Graham’s theory led to a better understanding of how EDLCs are affected by the nature of their electrolytes; such as ions size, polarizability and overall capacitance-dependency on the electrode potential. Moreover, it is essential to clarify integral electrochemical processes at the double-layer interface in order to present more realistic characteristics of EDLC. Therefore, the theoretical treatment of all elements in this research will be discussed based on Graham model. The proposed circuit was followed by including initial development of the relationships between electrical components, such as double-layer capacitances combined with ions diffusion and specific adsorption in both IHP and OHP, the presence of resistances at interfacial double-layer and bulk process in electrolyte.

4.2.1 Electrochemical Double Layer Capacitance at the Double-layer Interface

An ideal EDLC is independent on the working frequency or applied voltage when its capacitance and internal resistance are evaluated. In practice, however, dependence of the capacitance and resistance on frequency and voltage is commonly observed [143]. These deviations from the ideal capacitive behavior of EDLC are attributed mainly to ionic chemical/physical adsorption and diffusional impedance, incomplete polarization of the porous electrode, and Faradaic charge transfer resistance caused by the voltage differential across the electrode/electrolyte interface [162, 163]. In particular, the measured double-layer parameter is not an ideal capacitor because of the porosity of electrode materials, inhomogeneous pores distribution, roughness and non-linear current density. Due to non-ideal behavior, the double-layer capacitor is replaced by a constant phase element (CPE) representation and not a pure capacitor [129]. In many cases, the CPE is placed in parallel with an interfacial resistor in a circuit. Table 4.1 lists the common circuit elements, their impedances, the comparison between a pure capacitor and CPE, resistor and Warburg element (W). Each element is discussed with their concept of impedance representation in EDLC circuit modeling.

Table 4.1 Circuit elements used in the model and mathmatical equation for each impedance

Equivalent element	Impedance	Note
Resistor (R)	$Z_R = R$	Independent on frequency
Capacitor (C)	$Z = \frac{1}{j\omega C}$	A pure capacitor Inversely liner dependency on frequency C: capacitance, ω: frequency (1/sec)
	$Z_{CPE} = \frac{1}{Q(j\omega)^{\alpha}}$	Constant phase element (CPE) Non-liner dependency on frequency Q: CPE coefficient, α: exponent ($0 < \alpha < 1$)
Warburg (W)	$Z_W = \frac{1}{Q_w\sqrt{j\omega}}\coth\left[B\sqrt{j\omega}\right]$	Bounded diffusion layer Q_W: Warburg coefficient B is theoretically defined as follows; $\delta/D^{1/2}$ where, δ: Nernst diffusion layer thickness D: diffusion coefficient

- **Helmholtz (C_H) and diffusion (C_{diff}) capacitance**

Graham's model presents the overall double layer capacitance which is composed of three contributions: adsorption capacitance (C_{ads}), Helmholtz capacitance (C_H) and diffusion capacitance (C_{diff}). The latter two capacitances can be connected in series and expressed by equation (48). C_H represents the compact Helmholtz layer formation form solvated ions attracted electrostatically in the OHP layer while C_{diff} results from the ions transportation, caused by a gradient between the bulk and interfacial concentration of electrolyte's ion. In fact, charge-transfer processes with the measureable resistance consume the electrolyte's ions at the interface and develop a concentration gradient. In unsupported systems, there is a limited supply of ions from the electrolyte and the diffusion process occurs in a bulk solution overlapping with the diffusion layer. These phenomena can be interpreted using the Warburg element (W) for the bounded diffusion layer in series with the resistance of bulk solution (R_{bulk}) [164]. In EDLC, this diffusion capacitance is very important factor to influence the final performance of EDLCs in various applications [130, 165]. According to equation (3), the diffusion capacitance is depending on the number of ions and their charge (conductance) in electrolytes. When the frequency increases or low conductive ions are used, the number of ions involved in diffusion process can be reduced, therefore resulting in a decrease of capacitance. Otherwise, various parallel diffusion mechanisms can be determined by changing the potential difference, the electrode surface area and the bulk solution concentration.

- **Adsorption capacitance (C_{ads})**

In Grahame's theory, it was recognized that dehydrated ions in IHP region could reside on the electrode surface with specific adsorption processes. This phenomenon results in adsorption capacitance, C_{ads}. In a certain system, this C_{ads} can be regarded as another capacitive element with some part of the electrochemical charge-transfer process. This phenomenon is called pseudocapacitance. Therefore, the overall capacitance in EDLC can be represented by C_{ads} and a series combination with C_H and C_{diff} in parallel, resulting in an equivalent circuit depicted in Figure 4.2 (a). Generally speaking, for an adsorbed species formed by charge transfer in IHP, the capacitance is associated with a Faradaic charge (qF), and the charge is dependent on the potential difference (V). This allows C_{ads} to be defined as:

$$C_{ads} = \left(\frac{\partial qF}{\partial V}\right) \tag{49}$$

Therefore, it can be seen that C_{ads} corresponds to the variation between the differential charge and voltage [166]. However, it is necessary to differentiate with another pseudo-capacitance which originates from Faradaic (oxidation/reduction reactions) processes due to other sources such as metal oxide, conductive polymers or the functional group.

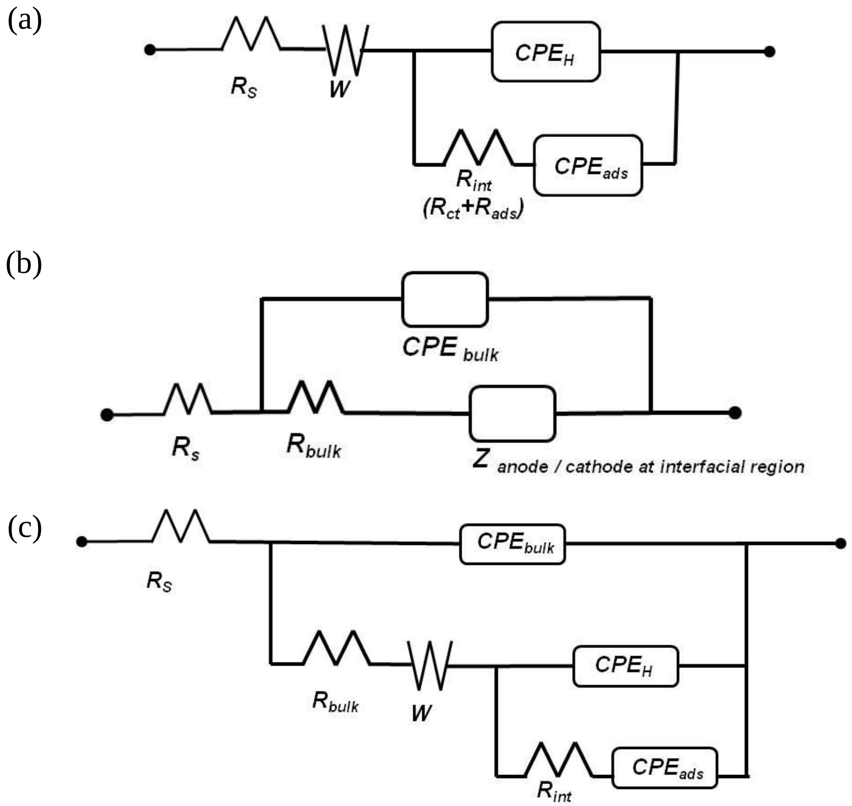

Figure 4.2 Equivalent circuits modeling of (a) interfacial processes at doulbe-layer, (b) consideration of bulk processes and (c) the completed circuit

This pseudo-capacitance is different from the employed here whose extent of faradaically delivered charges is a function of voltage, but a reversible process with the negligible leakage current [167]. In terms of circuit configurations, when a pseudo-capacitance is involved, generally, there are a Faradaic leakage resistance in parallel with pseudo-capacitor. However, in an ideal EDLC system where there are no Faradaic processes from metal oxide types of electrodes or conductive polymer, the leakage resistance in parallel with Cads may not be present or the magnitude of leakage current may be negligible.

4.2.2 Resistance at the Double-layer Interface Region

At the double layer interface, the electrochemical reaction is usually composed of charge transfer, adsorption and mass trans-port. Therefore, the interfacial resistance is associated with (1) a charge-transfer resistance (R_{ct}) where the electrode/electrolyte interface is not polarised in an ideal manner. This leads to current leakage, and (2) an adsorption resistance (R_{ads}) representing the impedance to the formation of C_{ads} resulting from kinetics of specifically adsorbed ions at interfacial layer.

- **Charge transfer resistor (R_{ct})**

The charge-transfer resistance, R_{ct}, is mainly related to the gradients of potentials between the electroactive species (in this study, hydrogen (H^+) and sulfate (SO_4^{2-}) in the aqueous electrolyte and Tetraethylammonium ($Et4N^+$) and Tetrafluoroborate ($BF4^-$) in the organic electrolyte) in electrolytes and the electrode surface, leading to the charge transfer phenomena. This charge transfer reaction is controlled by the kinetics of the electrochemical reactions and the diffusion of ions near the electrode surface. Hence, it is a common principle to connect R_{ct} in parallel with double layer capacitance to describe the interfacial leakage resistance at double layer. If there is an electron-transfer reaction, R_{ct} becomes smaller, otherwise, charge-transfer resistance becomes very large and electrode is polarised with poorly defined potential. Obviously this process is dependent on concentration of electrolytes, applied potential, temperature and surface structures of the electrode [168].

- **Adsorption resistor (R_{ads})**

The adsorption impedance depends on charges, associated with specific adsorption of charged species (dehydrated ions or solvent molecules) in the inner Helmholtz as a portion of the adsorption layer (Figure 4.1). The adsorbed species typically do not exchange electrons directly with the electrode and do not produce a pure Faradaic current, but they change the surface charge density resulting in the interfacial current path [43]. The equivalent circuit in this system can be represented by the combination of a resistor (R_{ads}) with a capacitor (C_{ads}) in series. Here, the resistance, R_{ads}, is an integral part of the physical phenomenon that gives rise to the formation of C_{ads} with no charge transfer. Otherwise, as discussed before, the adsorption processes can be treated like most charge transfer reaction, such as pseudo-capacitance. In such systems with metal oxide or conductive polymer electrodes, R_{ads} is intimately associated with the charge-transfer resistance (R_{ct}) since C_{ads} is corresponding to a Faradaic process, resulting in a parallel combination of R_{ads} with C_{ads} to present pseudo-capacitive effects. However, in this study, an electrical double layer with no pure Faradaic process is presented; therefore, the total interfacial resistance (R_{int}) can be expressed as:

$$R_{int} = R_{ct} + R_{ads} \tag{50}$$

4.2.3 Bulk Solution Impedance

In many practical cases, the high-frequency impedance response must be carefully analyzed and separated from the measured total impedance to identify the interfacial low frequency impedance components. In a typical experimental situation, the bulk electrolyte processes dominantly at high frequencies and electrochemical kinetics at the electrode-electrolyte interface is observed at lower frequencies. This is because there is not enough time to form the double layer at the very high frequency, so that there are no effects from interfacial electrochemical reactions. Therefore, the impedance analysis can treat bulk and interfacial processes separately, on the basis of selective responses to sampling AC frequencies. The bulk process is valid only at high AC frequencies, where the electric current must overcome the bulk impedance. This may lead to the formation of a capacitance in parallel with the bulk resistance. Hence, the expression for the high frequency impedance from bulk solution can be modeled by the parallel combination of bulk resistance (R_{bulk}) and capacitance (C_{bulk}). These bulk impedance elements are placed in parallel with the interfacial impedance as shown in Figure 4.2 (b).

To develop an accurate equivalent circuit, three major aspects of the physics of the EDLC have been taken into account. First, based on the theory of the interfacial layer in EDLC, the total capacitance was approximated as a combination of three separate capacitances; adsorption layer (inner Helmholtz layer), the com-pact double layer (outer Helmholtz layer) and diffusion layer in the electrolyte. More specifically, it was represented by the combination of Helmholtz-layer capacitance (C_H) in series with diffusion layer (W), and adsorption capacitance (C_{ads}) placed in parallel. Therefore, the equivalent circuit of an EDLC was modeled by three capacitive elements. The second aspect is that the interfacial resistance was defined by the combination of charge transfer resistance (R_{ct}) and adsorption resistance (R_{ads}) in Helmholtz layer (refer to Figure 4.2 (a)). Thirdly, the circuit was modified by considering the bulk media processes to present the impedance of the practical device in whole frequency range. As a result, the complete equivalent circuit for EDLCs is given as in Figure 4.2 (c) and the resulting expression for the total impedance of the cell becomes:

$$Z = R_s + \left[\frac{1}{Z_{CPE_{bulk}}} + \frac{1}{R_{bulk} + Z_W + \left[\frac{1}{Z_{CPE_H}} + \frac{1}{R_{int} + Z_{CPE_{ads}}} \right]^{-1}} \right]^{-1} \tag{51}$$

where each impedance (Z) for elements are defined in Table 4.1. This equation was employed to simulate the overall impedance value for a cell at sufficiently low frequencies.

4.3 Experimental

Activated carbon electrodes were prepared using cast-coating with slurry, as described previously in Chapter 3. To compare the electrochemical properties of two distinct electrolytes, 1 M organic (Et_4NBF_4 /PC) and 1 M aqueous (H_2SO_4) electrolytes were prepared. The electrochemical properties of a coin-typed cell with identical activated carbon electrodes and two different electrolytes were evaluated using cyclic voltammetery (CV) and constant current charging/discharging (CCD) measurements by a Gamry Reference 3000 Potentiostat. Electrochemical impedance spectroscopy (EIS) was performed on the same Potentiostat using EIS 300 software (Gamry Inc.). All EIS measurements were achieved by applying a low sinusoidal amplitude AC voltage of 4 mV on a cell at a frequency range from 10 mHz to 100 kHz. To evaluate potential dependency, measurements were performed at various fixed DC voltages depending on the type of electrolytes. Differential capacitance and resistance versus frequency curves in Bode plots were obtained by taking the real components of the impedance at different operating frequencies. Through fitting experimental EIS data with the proposed equivalent circuit, the calculated values for real and imaginary components of the impedance were corrected for each element (capacitors and resistors at frequency 10 mHz) and converted into total impedance of a cell using equation. (51).

4.4 Results and Discussion

4.2.1 Electrochemical Characteristics

Figure 4.3 shows the cyclic voltammetry curves of coin-typed cells measured in aqueous (1 M H_2SO_4) and organic (1 M Et_4NBF_4/ PC) electrolyte, respectively. Since the two electrodes were identical and the ideal activated carbon is non-Faradaic material, its current response was symmetrical and similar to an ideal EDLC.

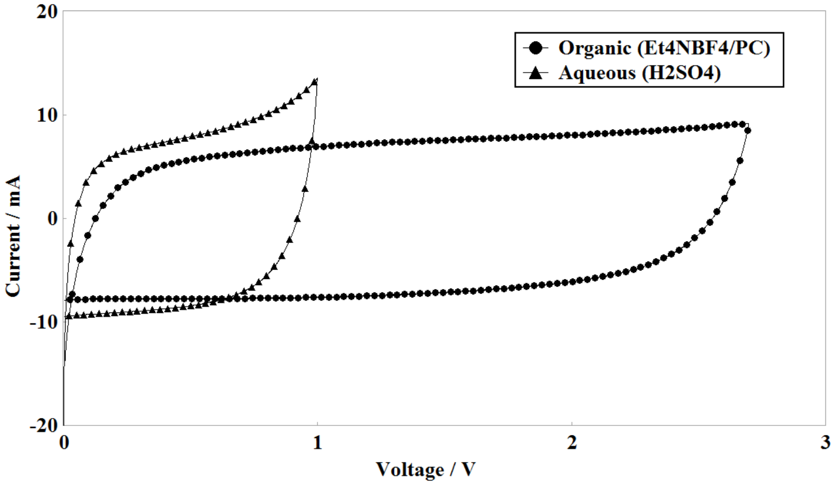

Figure 4.3 Cyclic voltammetry for organic and aqueous electrolytes at the scan rate 20 mV/s

Although the aqueous electrolyte shows some distortion from the ideal CV shape at near 1 V due to the decomposition of the electrolyte, it clearly shows that the organic electrolyte did not have any distortion up to 2.7 V. The specific capacitance for a single electrode was measured from CV measurements, which was about 108 F/g in the organic electrolyte and 134 F/g in the aqueous electrolyte, respectively. In order to clarify the absence of Faradaic processes of redox reactions, further CV measurements with different scan rates were carried out as described in Figure 4.4.

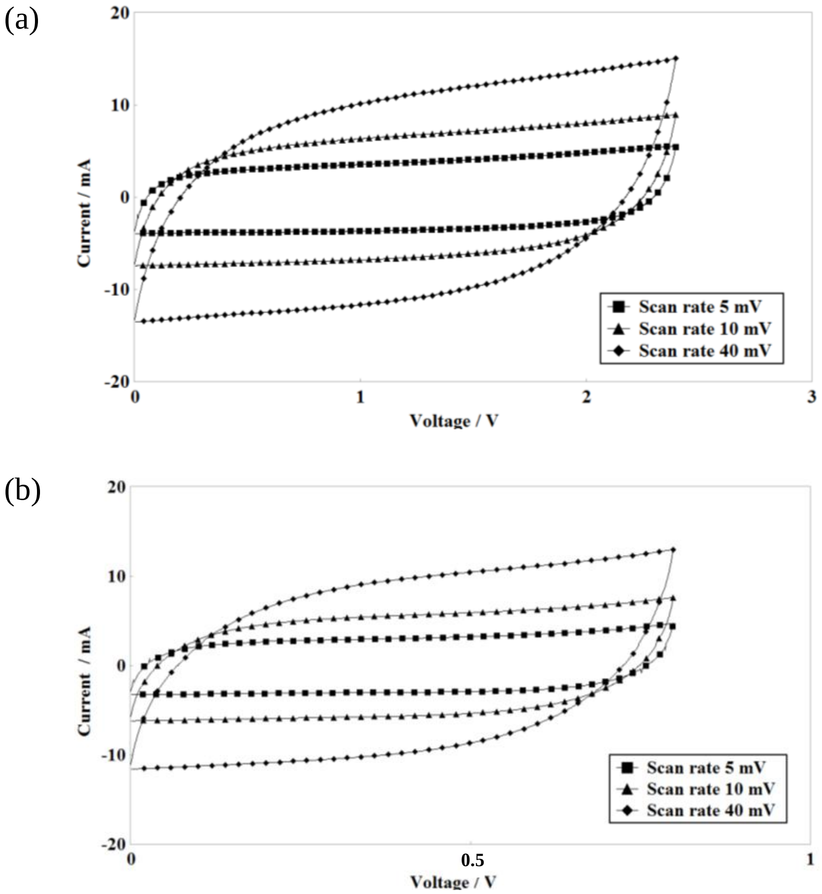

Figure 4.4 Cyclic voltammery at various scan rates, 5, 10 and 40 mV/s: (a) organic (1 M Et_4NBF_4/PC) electrolyte up to 2.4 V, (b) aqueous (1 M H_2SO_4) electrolyte up to 0.8 V, respectively

The parallelogram-like CV curves were maintained in various scan rates, which is a major characteristic of non–Faradaic process in an EDLC. This result indicates that, in both tested cells, there was less pesudocapacitance caused by surface reduction/oxidation or functional groups on the surface of the electrodes. The cells were then subjected to the constant current charge-discharge test to evaluate their capacitive behaviors and equivalent series resistances (ESR or self-discharge) by measuring the IR drop at various charging voltages, as suggested in the literature [162, 169]. For this purpose, the data from charging/discharging measurements at constant current loads were analyzed. The cells were charged from 0 V to different rated voltages to investigate the potential influence on ESR. As a result, the measured series resistance is calculated as

$$ESR = \frac{\Delta V}{\Delta I} \quad (52)$$

where V is the initial voltage (ohmic) drop at the beginning of discharging process, and I is constant charging/discharging current. The overall internal resistance in a cell was represented by the calculated ESR values. As shown in Figure 4.5, the organic electrolyte (Figure 4.5 (a)) shows a higher voltage drop than aqueous electrolyte (Figure 4.5 (b)). Also, for the same electrolyte, the ohmic drop decreased as the charging voltage increased. This difference is much larger for the organic electrolyte than the aqueous electrolyte. This is because the aqueous electrolyte has a much higher conductance than organic electrolyte [170]. The corresponding ohmic drop and ESR values calculated according to equation (52) were collected in Table 4.2.

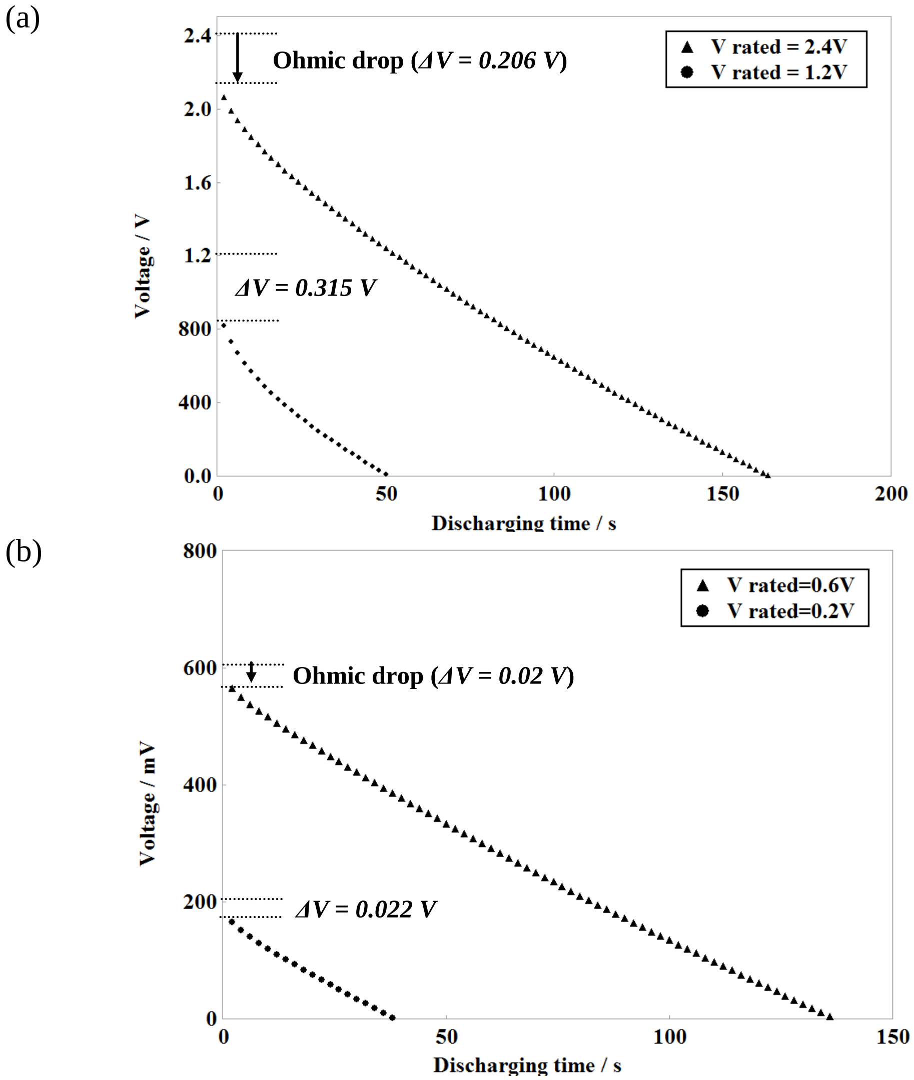

Figure 4.5 Discharging processes at the constant current (30 C-rate) and the determination of ohmic drops with different charging voltages for (a) Organic electrolyte,up to 1.2 vs. 2.4 V and (b) Aqueous electrolyte, up to 0.2 vs. 0.6 V, respectively

Clearly, the current response of the organic electrolyte is largely affected by the applied potential differential and shows an increase in capacitance and a decrease in ohmic drop with voltages. Less significant changes were observed in the aqueous electrolyte. This implies that both capacitance and internal resistance are dependent on the properties of the electrolyte, such as its conductance and ionic mobility.

Table 4.2 Measured values of ohmic drop and ESR from the charging/discharging cycle at the constant current (30 C-rate) for two electrolytes

Electrolytes	Constant current* (*mA*)	V_{min}	V_{max}	Capacitance at discharging (*mF*)	Ohmic Drop (*ΔV*)	ESR (*Ω*)
Organic (1M Et_4NBF_4/PC)	6.8	0	1.2	281	0.315	26.2
		0	2.4	325	0.206	17.1
Aquous (1M H_2SO_4)	2.3	0	0.2	514	0.022	4.82
		0	0.6	545	0.02	4.34

* This current value is corresponding to 30 C-rate (1/30 hour) at discharging from the maximum rated voltages, 2.7 V of organic or 1.0 V of aqueous electrolyte.

Figure 4.6 presents the Nyquist plot for two cells with identical activated carbon electrodes immersed in two different electrolytes: 1 M H_2SO_4 and Et_4NBF_4 in propylene carbonate (PC). The first intersection point on the real axis at the highest frequency shows a series resistance of cells (R_S) that generally originates from solution resistance in the electrolyte, separator and external circuit resistances. Since two tested systems have the same components except for the electrolyte, R_S is mainly attributed to the resistance of electrolytes. Therefore, the higher conductivity of the aqueous electrolyte leads to the lower resistance. The semi-circle present at high frequencies is associated with the interfacial resistance between electrode and electrolyte. The organic electrolyte data, as compared to the aqueous, displayed a larger semi-circle, indicating a higher resistance at its interfacial layer. At medium frequencies, a straight line with a slope of 45 ° appears and this impedance reflects the ion diffusion phenomena in the porous structure. Subsequently, both cells behave like a pure EDLC capacitor which is characterized by the vertical line at low frequencies.

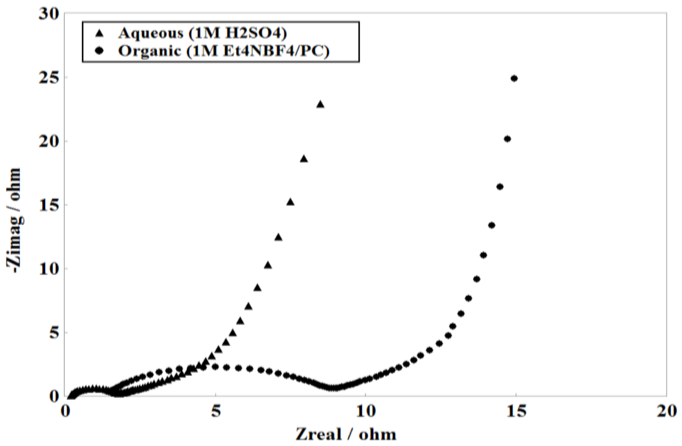

Figure 4.6 Nyquist plots for cells in 1 M H_2SO_4 and 1 M Et_4NBF_4/PC electrolytes, respectively. Measurement was performed at the applied voltage of 5 mV, with the frequency range from 10 mHz to 100 kHz

The Bode plots shown in Figure 4.7 describe the resistance and capacitance as function of the frequency. In Figure 4.7 (a), three distinguishable resistances, which are independent of frequency, exist on both curves and can be correlated to individual resistive components (R) defined in Section 4.2. Specifically, the resistance at the high frequency range shows mainly the value of R_S while the Faradaic leakage or charge transfer resistance from bulk electrolytes (R_{bulk}) appears at the medium frequency range between 10 Hz and 1kHz. The low frequency range between 10 mHz and 1 Hz includes R_{int} caused by interfacial processes, and represents the summation of R_S, R_{bulk} and R_{int}.

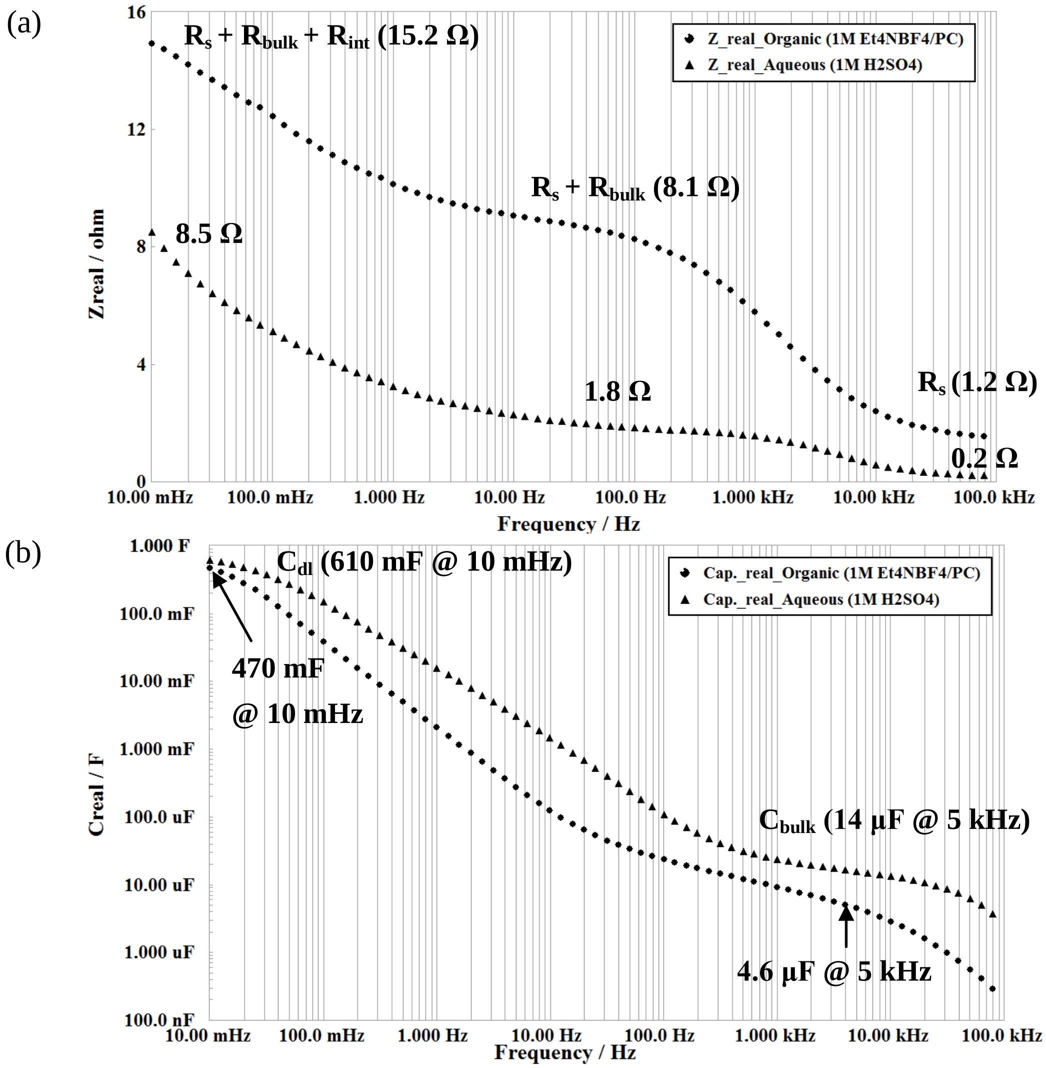

Figure 4.7 Bode polt of (a) real impedance and (b) real capacitance vs. frequency for two electrolytes

On the other hand, Figure 4.7 (b) demonstrates the frequency dependence of the capacitance. The capacitance reaches its maximum at the low frequency because the ions have sufficient time to reach to the pores and then form the double layer on the electrode surface. The value of capacitance at the lowest frequency hence represents the overall capacitance at the double layer interface (C_{dl}). The rated capacitance is around 670 mF for aqueous H_2SO_4 electrolyte and 470 mF for organic Et_4NBF_4/PC electrolyte at 10 mHz, respectively. As the frequency increases, the contribution of C_{dl} decreases due to insufficient ion transport, and the major contribution changes to partial capacitance from bulk electrolyte's process (C_{bulk}) measured as above 14 to 5 F at 5 kHz for both electrolytes, respectively. Compared to the aqueous electrolyte, the organic electrolyte exhibits a larger resistance and a lower capacitance throughout the entire frequency range, due to the greater energy barrier against its ion transport. This transport occurs in both the bulk solution and diffusion layer as ionic diffusion (driven by the concentration gradient) and ionic migration (driven by the electric field). In this study the relevant impedance was observed at the low frequency range from 1 Hz to 100 Hz (see in Figure 4.7 (a)), which confirms the diffusion dominant impedance for the organic electrolyte. Meanwhile, the ion transport impedance is closely associated with the double-layer formation process, which results in a less value of C_{dl} (see Figure 4.7 (b)).

4.2.2 Simulations with an Equivalent Circuit and Potential Dependency

The measured EIS data from Nyquist and Bode plots were compared with simulated parameters obtained from the equivalent circuit model which is given in Figure 4.2 (c). Figure 4.8 describes the measured (symbols) and simulated (lines) impedance spectra for aqueous and organic electrolytes in Nyquist plots. The experimental data closely matches the model predicted data in both low and high frequency regions, which were unsuccessfully achieved using the models shown in Figure 4.2 (a).

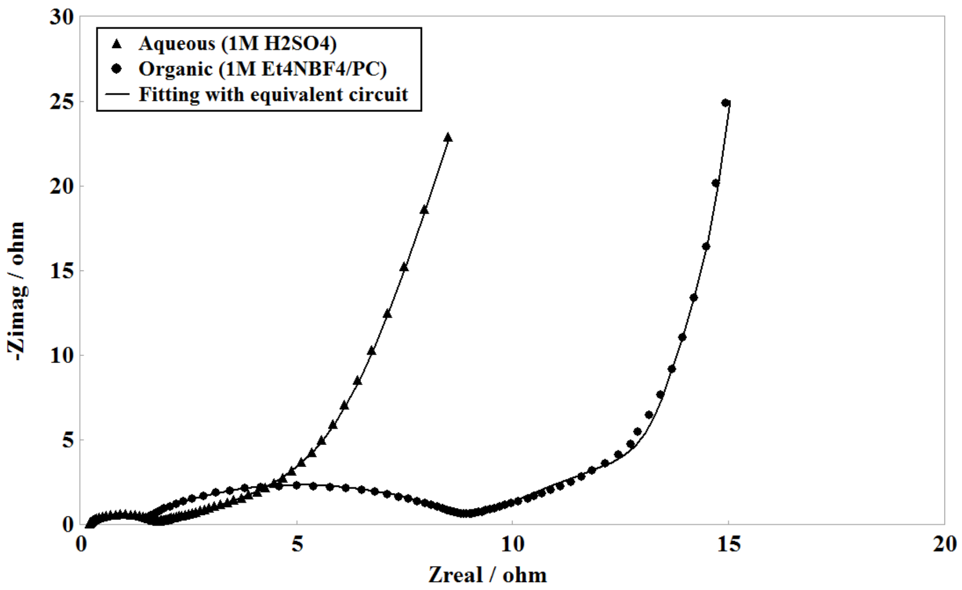

Figure 4.8 Simulated impedances, Zreal and Zimag, with measured Nyquist plots for aqueous and organic electrolytes

Using the equivalent circuit, the extracted parameters for different electrolytes are summarized in Table 4.3. In comparison with measured data from Bode plots (Figure 4.7), the simulated values for resistance and capacitance show a reasonable consistency with the measured ones. In addition, this simulation indicates that R_{int} can be considered as the most dominant parameter in determining the operating ohmic resistance of tested cells. This means R_{int} can be used to study the characteristics of ohmic leakage current or internal resistance of EDLC cells. For capacitance values, the model predicted, C_{bulk} of tens of micro farad, in agreement with experimental values. The summation of C_H and C_{ads} is around 640 mF in aqueous and 540 mF in organic electrolytes, respectively. These values are close to the measured double layer capacitance, C_{dl}, shown in Figure 4.7. Meanwhile, the organic electrolyte exhibits lower C_H and C_{ads} compared to the aqueous one.

Table 4.3 Equivalent circuit parameters (Capacitance and Resistance) obtained from the simulation results with two electrolytes

Impedance values	Aqueous (1M H_2SO_4)		Organic (1M Et_4NBF_4/PC)		Unit
	Simulated	Measured	Simulated	Measured	
Rs	0.184	0.2	1.306	1.2	*ohm*
R_{bulk}	1.512	1.6	7.508	6.9	*ohm*
R_{int}	5.899	6.7	10.2	7.1	*ohm*
Z_W	2.131	-	4.272	-	*ohm*
C_{bulk}	15	14	6	4.6	*μF*
C_H	340	-	248	-	*mF*
C_{ads}	302	-	262	-	*mF*
C_{dl}	642	610	510	470	*mF*

These values of capacitance can be considered in terms of types of electrolyte and ion radius. According to equation (45), larger sized ions of the organic electrolyte possess lower C_{ads} and C_H because its Helmholtz layer thickness, d, of closest ion's approach are larger than the aqueous electrolyte's one, leading to less capacitance. This result agrees with the theory and experiments reported by Grahame [42]. Also, the lower conductivity of organic electrolytes exhibits higher diffusion impedance (Z_W), which corresponds to the fact that organic electrolytes have the less ion movement and larger energy barrier to diffusional processes, resulting in the larger diffusion impedance (around 4.3 Ω) than one (2.1 Ω) of the aqueous electrolyte with a higher conductivity. In order to further characterize the resistance and capacitance dependency on the applied voltage level, additional EIS measurements was performed for voltage levels at 0.2 and 0.6 V on aqueous electrolytes, and at 1.2 and 2.4 V on organic electrolytes, respectively.

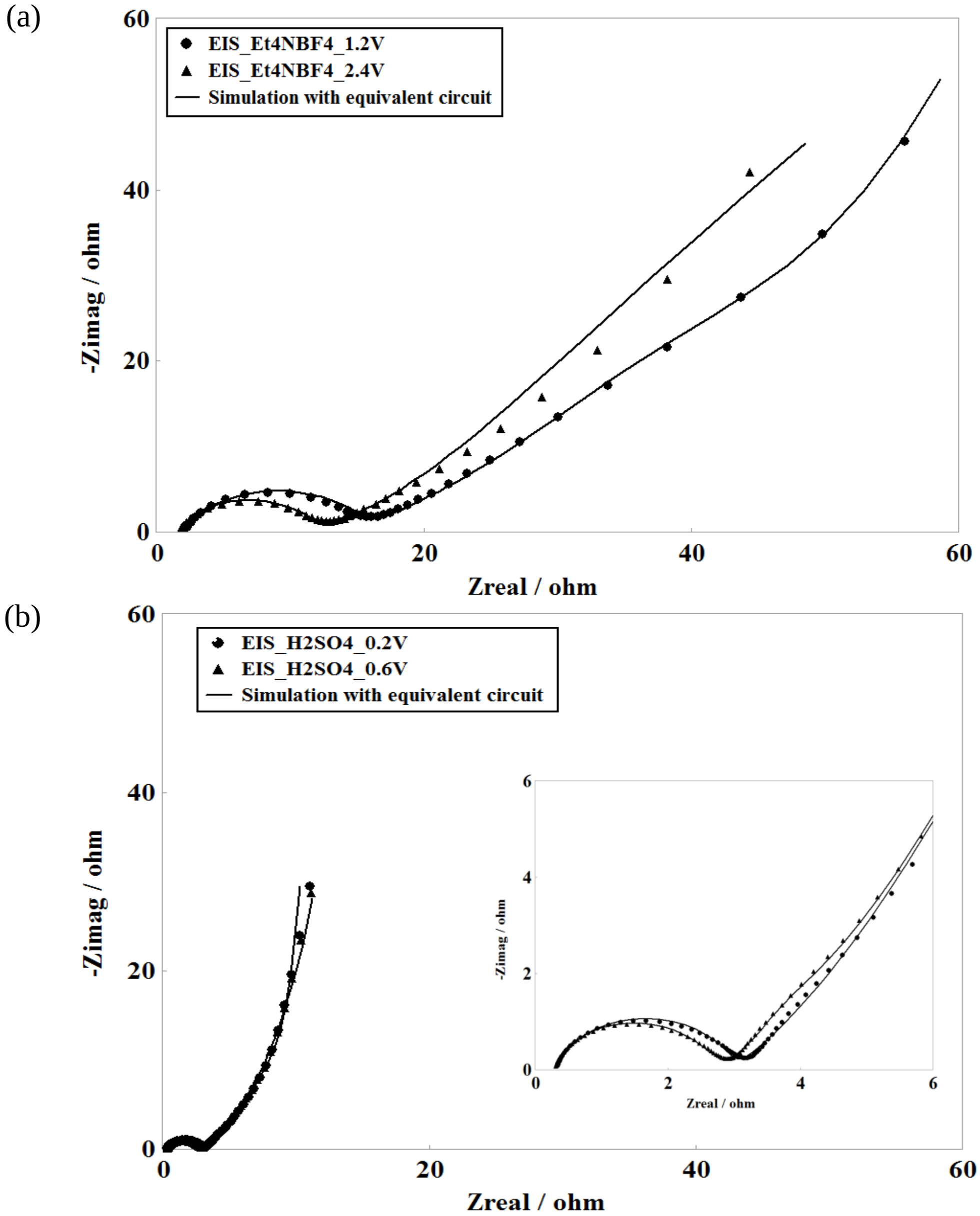

Figure 4.9 Measured and simulated impedances for the different applied voltage on (a) organic electrolyte, (b) aqueous electrolyte, respectively. The insert is an enlarged view at high frequencies

The applied voltages were respected to reflect the relative potential differential at electrode-electrolyte interface. Figure 4.9 shows the Nyquist plot for two electrolytes obtained at different voltage levels. At the low voltage with the decreased DC potential across the interfacial double layer, the more right-shifted vertical line in the low frequency region was shown and the larger semicircle was presented, which means the overall resistance increases at double layer interface.

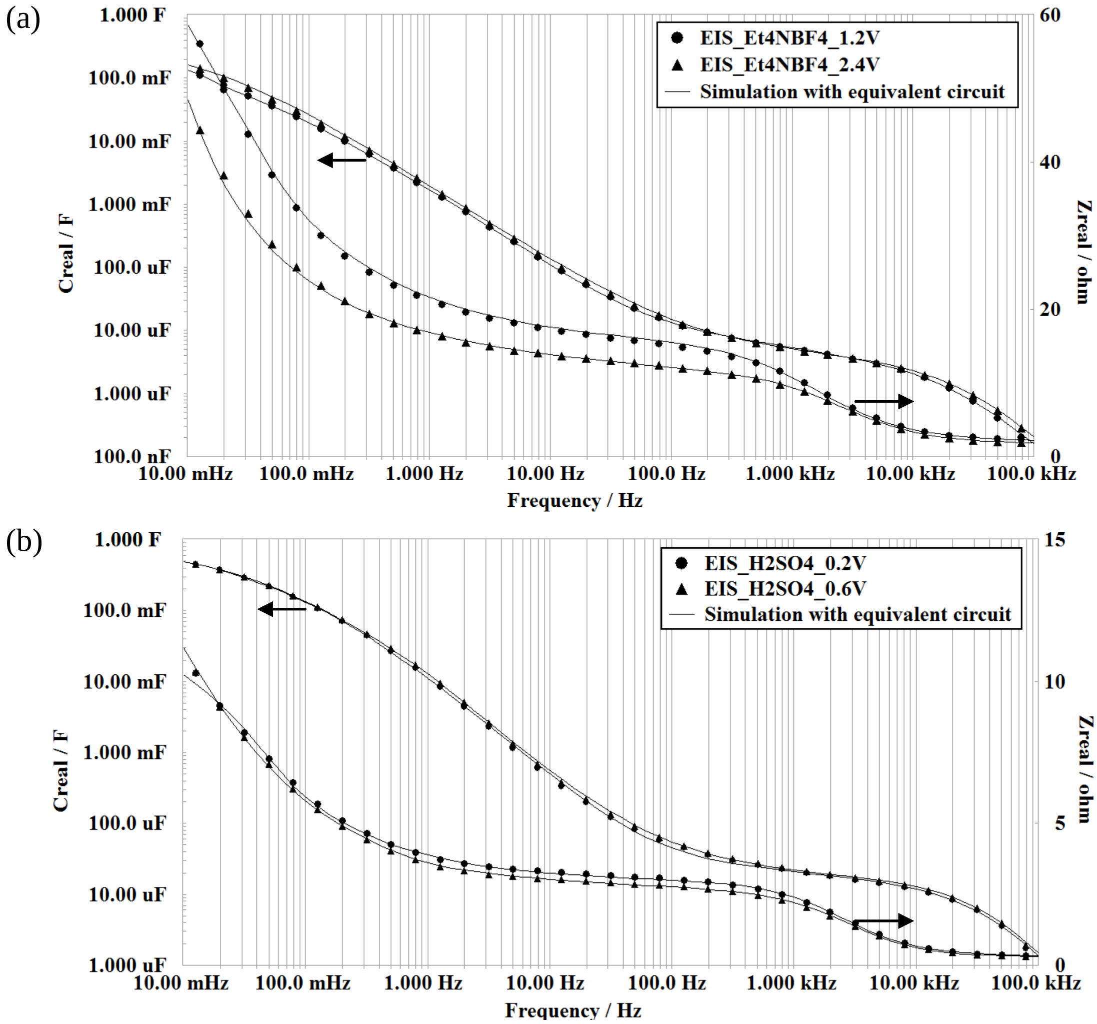

Figure 4.10 Measured and simulated differential capacitances and resistances depending on the applied voltages for (a) organic electrolyte, (b) aqueous electrolyte, respectively

That is, the higher resistance at low potential causes to larger leakage current. This result was in agreement with characteristics of the current response from various applied voltages in CCD measurements, introducing the differences of ohmic drop or ESR. The differences in capacitance and resistance as function of frequency were described in Figure 4.10, which again shows excellent agreements between measured and simulated data. It is worth-while to note that larger potential led to the lower resistance and the higher capacitance over the whole frequency range. In addition, this effect is more significant in the organic electrolyte, indicating the organic electrolyte showed a larger dependency on the applied potential change when compared to the aqueous electrolyte. For simulation, the measured impedance spectra were fitted by an equivalent circuit and the simulated parameters are summarized in Table 4.4 and Table 4.5. Similar to experimental EIS results, the notice-able resistance changes were observed. More details, compared to other resistances (R_S and R_{bulk}), it can be clearly seen that the interfacial resistance (R_{int}) is significantly reduced when the potential increased. As discussed before, R_{int} is associated with charge transfer and kinetics of adsorbed ions in the formation of outer/inner Helmholtz layers. Therefore, the higher potential leads to more electron transfer and ions adsorption at the interfacial layer, results in a smaller R_{int}. Also, the Helmholtz capacitance (C_H) decreases while the adsorption (C_{ads}) increases, and the diffusion impedance is reduced. This is mainly caused by the acceleration of adsorption reactions and diffusion rate caused by a larger differential potential. According to the Gouy-Chapman model of diffusion double layers, the capacitance is proportional to the differential potential as described in equation (47). Consequently, at high potential conditions, adsorption and diffusion capacitances contribute more to the overall capacitance.

Table 4.4 Calculated parameters (Capacitance and Resistance) obtained from the simulation results with different applied voltages on aqueous electrolyte (1M H_2SO_4)

Simulated impedance values	0.2 V	0.6 V	Unit
Rs	3.08E-01	2.85E-01	*ohm*
Q_{bulk}	9.51E-05	8.73E-05	$S*s^{\alpha}$
α_{bulk}	8.55E-01	8.69E-01	
C_{bulk}	16	17	μF
R_{bulk}	2.67	2.45	*ohm*
Q_W	3.16E-01	3.51E-01	$S*s^{(1/2)}$
B	4.85	3.15	$s^{1/2}$
Z_W	3.16	2.85	*ohm*
Q_H	6.83E-01	4.78E-01	$S*s^{\alpha}$
α_H	9.69E-01	8.97E-01	
C_H	346	281	*mF*
R_{int}	1.93	0.279	*ohm*
Q_{ads}	1.61E-02	1.22E-01	$S*s^{\alpha}$
α_{ads}	4.79E-01	5.35E-01	
C_{ads}	224	315	*mF*

Table 4.5 Calculated parameters (Capacitance and Resistance) obtained from the simulation results with different applied voltages on organic electrolyte (1M Et_4NBF_4/PC)

Simulated impedance values	1.2 V	2.4 V	Unit
Rs	2.05	1.63	ohm
Q_{bulk}	4.55E-05	3.79E-05	$S*s^{\alpha}$
α_{bulk}	7.94E-01	8.07E-01	
C_{bulk}	3.9	3.6	μF
R_{bulk}	13.2	9.79	*ohm*
Q_W	9.67E-02	8.33E-01	$S*s^{(1/2)}$
B	6.14	1.11	$s^{1/2}$
Z_W	10.34	1.2	*ohm*
Q_H	9.59E-02	5.45E-02	$S*s^{\alpha}$
α_H	4.56E-01	5.09E-01	
C_H	121	25	*mF*
R_{int}	38	24.2	*ohm*
Q_{ads}	5.47E-02	3.05E-02	$S*s^{\alpha}$
α_{ads}	8.58E-01	6.27E-01	
C_{ads}	109	262	*mF*

This tendency is similar for both electrolytes, but it is seen in Table 4.5 that larger difference in Z_W are seen in the organic electrolyte when compared to the aqueous one(see Table 4.4), which means the diffusion of organic electrolyte is more affected by the potential differences resulting in the larger deviation of Z_W.

In order to validate the equivalent circuit model, these impedance characteristics were correlated with distributed current leakage or ESR in practical cells. In Figure 4.11, the total impedance obtained from the simulation is compared with the ESR from CCD measurements.

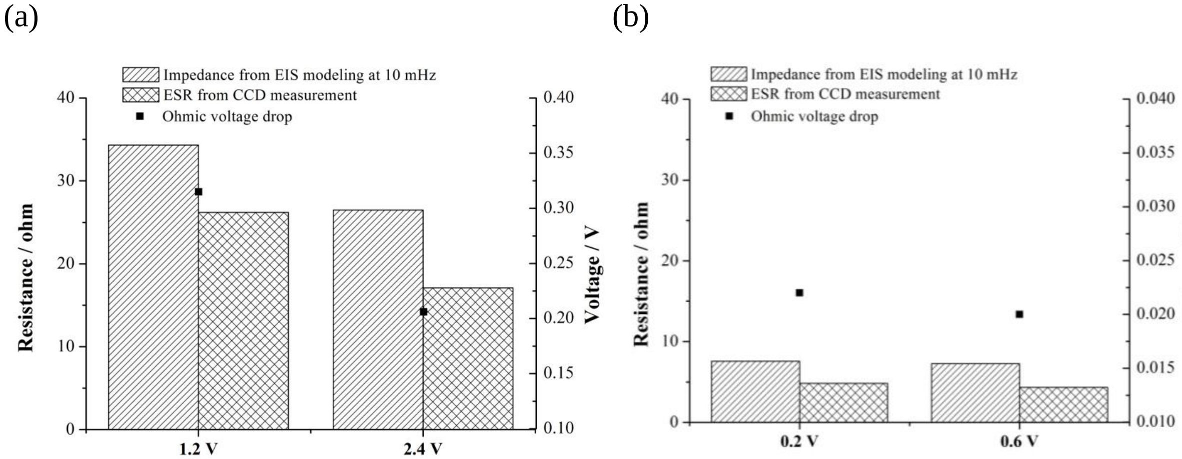

Figure 4.11 Correlation between EIS modeling and CCD measurement; ESR difference from the applied voltages for (a) organic electrolyte, (b) aqeuous electrolyte, respectively

From equation (51), the total impedance was calculated by simulating each resistor and capacitor at 10 mHz. Although the equivalent resistance from EIS measurements is usually lower than other measurement techniques [162], this value gives an informative indication of internal resistance for EDLC devices. Note, the value from modeling is not exactly same as the experimental ESR, but the similar potential dependency has been shown between EIS modeling and CCD measurement.

As for the discussion based on model prediction, two major considerations were made in the development of the equivalent circuit model for an EDLC. First, the circuit modeling was developed based on theoretical descriptions of ELDC structures and effects of electrochemical reactions coupled with diffusion and adsorption phenomena in the electrochemical double layer. Secondly, this circuit was designed to provide the meaningful information on each physical process in practical EDLC devices. The dominant resistive elements in both interfacial and bulk processes have been found by improving the fitness to the EIS data. Importantly, the interfacial resistance (R_{int}) describes the extents of electron transfer reactions and kinetic of adsorbed ions in forming the double layer. For capacitive elements, the double layer capacitance (C_{dl}) is represented by a combination of Warburg impedance, W, and the compact Helmholtz capacitor, C_H, in parallel with adsorption capacitor, C_{ads}. The values of Z_W and C_{ads} have been analyzed to understand the diffusion behavior and adsorption process which depends on the ions sizes and conductivity of electrolytes. Also, the bulk capacitance, C_{bulk}, takes into account the bulk processes for a practical EDLC cell. It was found that the defined parameters in the proposed circuit are critical to demonstrate their characteristics, such as internal resistance or the potential-dependency. Therefore, the proposed circuit can be useful to characterize the EDLC-typed capacitors which are typically composed of porous carbon-based electrodes with ionic electrolytes. Furthermore, the simulated impedances of resistive elements provides informative values to predict the energy/power density and thermal behavior of EDLCs, because these factors are mainly dominated by internal resistances [171].

4.5 Summary

This work presents an improved equivalent circuit model to investigate the electrochemical and dynamic behaviors of EDLCs with porous carbon-based electrodes using different electrolytes. The characteristics of EDLC cells with two types of electrolytes, namely, aqueous 1 M $H_2SO_4$and organic 1 M Et_4NBF_4/PC, were studied by analyzing CV and CCD measurements. At the same time, the impedance behaviors of these EDLCs were utilized to evaluate the validity of circuit modeling. The simulation results showed that this new circuit model was able to characterize EDLCs with both aqueous and organic electrolytes. Moreover, the proposed circuit model provided a reasonable interpretation on physical processes occurring within the EDLC cell, through introducing a more clarified view of their electrochemical and transport phenomena. In addition, the EIS analysis on the potential dependency supported the proposed elements in the model and the ESR correlation between EIS and CCD measurements was derived. It was suggested that this circuit model is able to simulate sufficiently the potential-dependent characteristics of double layer capacitors.

Chapter 5 Characterization of Electrochemical and Thermal Behaviors with Porous Carbon Electrodes

5.1 Introduction

As a promising energy storage device, EDLCs based on porous carbon materials have been widely investigated and developed for electric vehicle, space, and military vehicle applications due to their high power/energy densities, high efficiency, long lifetime, and fast current responses during charging/discharging [157, 172, 173]. For such applications, it is believed that the ability to quickly store and deliver a steady amount of electrical energy in harsh environments can be determined from the properties of carbon electrodes and their electrochemical interactions with the electrolyte ions at double-layer interfaces [174]. In fact, a key to designing effective nano-structured carbon electrodes for EDLCs is to uncover the relationship between electrolyte ion sizes and electrode pore sizes. Matching the type of electrolytic ion with the pore structure of the electrodes can thus be considered an optimization approach to the design of high power and energy density products. It is therefore essential not only to characterize the electrochemical properties of porous electrodes and their effects on EDLC performance, but also to correlate the pore size distributions (PDS) in porous carbon to these properties and especially to the dynamic characteristics of the electrodes. Such a correlation could be achieved through an investigation of the way in which ion accessibility corresponds to a variety of charging-discharging frequencies. The thermal characteristics of a porous carbon electrode represent an additional factor that is important for estimating the practical lifetime of a device as well as the efficiency of its energy storage, because temperature affects ion kinetics and diffusion processes at the double-layer interfaces, causing variations in the internal resistance of the cells and degradation of power/energy density [136, 138].

The main goal of the work presented in this thesis was to conduct systematic studies of electrochemical and thermal characteristics between an organic electrolyte and three distinct types of carbon electrodes, activated carbon (AC), graphene, and single-walled carbon nanotubes (SWCNTs). A particular focus was the investigation of the effects of the pore size of the electrodes on the dynamic performance of EDLCs for different charging and discharging frequencies as a means of revealing correlations between pore distribution and electrochemical characteristics at specific applied frequencies. An additional factor considered was the direct correlation between variations in the structure of the electrodes and their thermal behavior in EDLCs. Based on an examination of the structural properties of electrodes such as their microstructure, surface area, and PSD, this study has addressed the question of how porous electrodes with different pore structures influence the capacitive and resistive characteristics at a variety of operating temperatures. To achieve these goals, the recently developed equivalent circuit model [175] has been used in order to simulate the effects of porosity on the temperature-dependent kinetic reactions (charge transfer, adsorption) and diffusion processes that occur at double-layer interfaces.

5.2 Experimental

In this study, SWCNT and graphene-based electrodes were fabricated by using the vacuum filtration deposition (VFD) method, as described in Chapter 3. Meanwhile, for comparison, cast-coating method was also used to prepare activated carbon electrodes.

Briefly, powdered activated carbon was mixed with the same PTFE and carbon black in the mass ratio of 90:5:5, then cold-rolled on the SUS foam. The cells were assembled with 1 M Et4NBF4/PC electrolytes using a 2013 coin cell. The unit cells were then placed in a climate chamber that simulates temperature changes. The operating temperature varied from -30 ℃ to 60 ℃ within the operating range to an accuracy of ± 1 ℃.

The structural properties of each type of electrode were determined by means of scanning electron microscopy (SEM) and transmission electron microscopy (TEM). Atomic force microscopy (AFM-tip mode) observation was conducted for the fully sonicated samples on freshly cleaved mica surfaces. The specific surface area and pore size distributions were measured using a nitrogen (N2) adsorption analyzer (Flowsorb from Micrometitics Instrument Corporation). The specific surface was estimated based on the Brunauer-Emmett-Teller (BET) analysis technique of the N2 isotherms. Pore size distributions (PSD) were determined from the Barrett-Joyner-Halenda (BJH) method for the meso-/macroporous range (between 2 nm and 100 nm) and the Horvath-Kawazoe (HK) method for the microporous range (less than 2 nm). Electrochemical characterizations were carried out using cyclic voltammetry (CV) and constant charge/discharge (CCD) measurements on a Gamry Instruments Reference 3000 potentiostat. CV tests were conducted at a variety of scan rates, ranging from 5 to 40 mV/s within the 2.7 V maximum voltage window of the electrolyte. Electrochemical impedance spectroscopy measurement was performed wiht the same potentiostat and with EIS 300 software in the frequency range of 0.1 Hz to 100 kHz at a 0.4 V cell potential. It should be noted that the preparation of electrodes using the above processes may lead to micro-structures that differ from components fabricated using other laboratory approaches. The focus of this study, however, was on the investigation of the effects of the size of pore on their electrochemical, dynamic, and thermal behaviors, and distinguishable pores are formed in AC, graphene and SWCNT electrodes.

5.3 Results and Discussion

5.3.1 Structural Properties of Electrodes

Representative SEM images of the AC, graphene and SWCNT electrodes are shown in Figure 5.1, and their microscopic structures are illustrated schematically to enable the visualization of their structural properties. The SEM observation shown in Figure 5.1 (a) indicates that the AC is composed of randomly agglomerated coagulations of fine particles into a three-dimensional porous network. In Figure 5.1 (c), it can be seen that the SWCNT presents typical bundle structures with randomly dispersed one-dimensional carbon nanotubes. SWCNT bundles can also be observed to be spanning holes and completing the SWCNT network. In contrast, graphene layers tend to form large, two-dimensional aggregated sheets, as shown in Figure 5.1 (b). The highlighted TEM image indentified in Figure 5.1 (b) appears as a number of over layered graphene sheets. The thin-layered graphene was also characterized using AFM analysis. Considering the thickness of a typical graphene nanoplatelet (1 to 20 nm as received), which is shown in Figure 5.2 (a), most of these sheets tend to interact with one another to form aggregated structures (as can be seen in the schematic illustration of Figure 5.1 (b)).

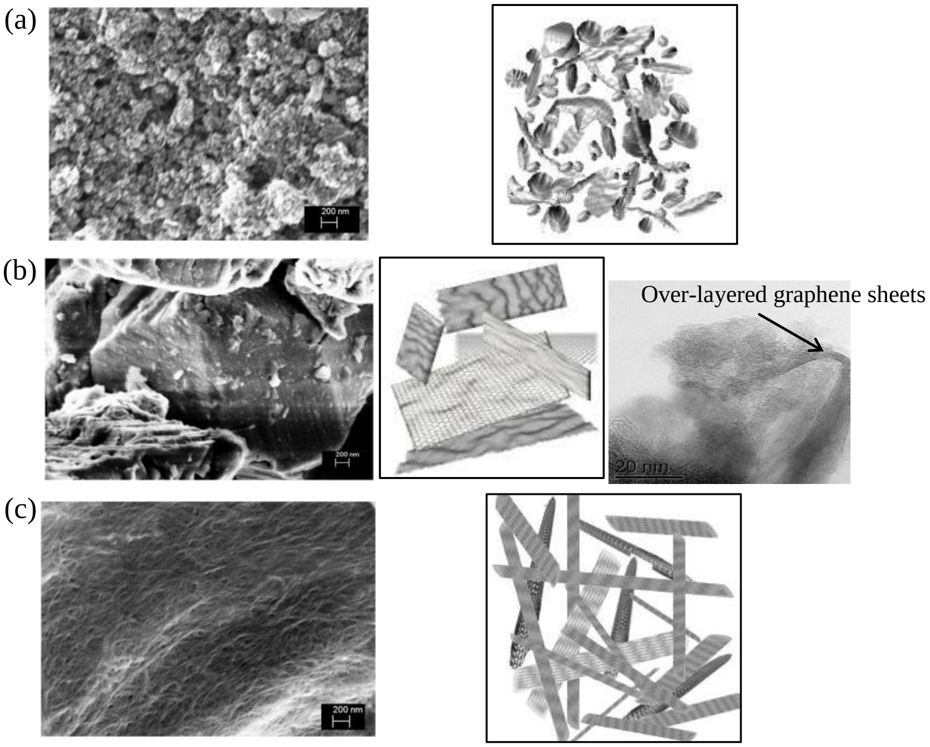

Figure 5.1 FE-SEM images of the electrodes: (a) AC, showing schematics of 3D randomly dispersed AC structures; (b) graphene, showing 2D agglomerated graphene sheets, including a TEM image of graphene layers; and (c) SWCNT, showing a 1D ramdomly dispersed SWCNT network

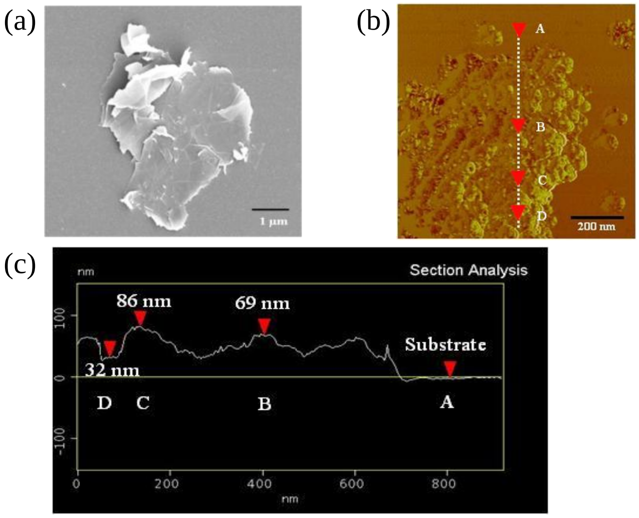

Figure 5.2 Graphene results: (a) SEM image of a typical graphene nanoplatelet; (b) AFM ichnography image; and (c) cross-section analysis of overlayered graphene nanoplatelets with A-D indicating the positions on the dotted line where the tip scanned

Figure 5.2 (b) presents the AFM ichnography, in which overlapping graphene sheets are identified. The corresponding cross-section profile in Figure 5.2 (c) clearly shows that the thickness of this overlapping structure ranges from 1 to 90 nm.

With respect to the analysis of the pore structures of the electrodes, Figure 5.3 shows a comparison of the N2 adsorption isotherms and the pore size distribution analysis of those graphs obtained for the AC, graphene and SWCNT electrodes.

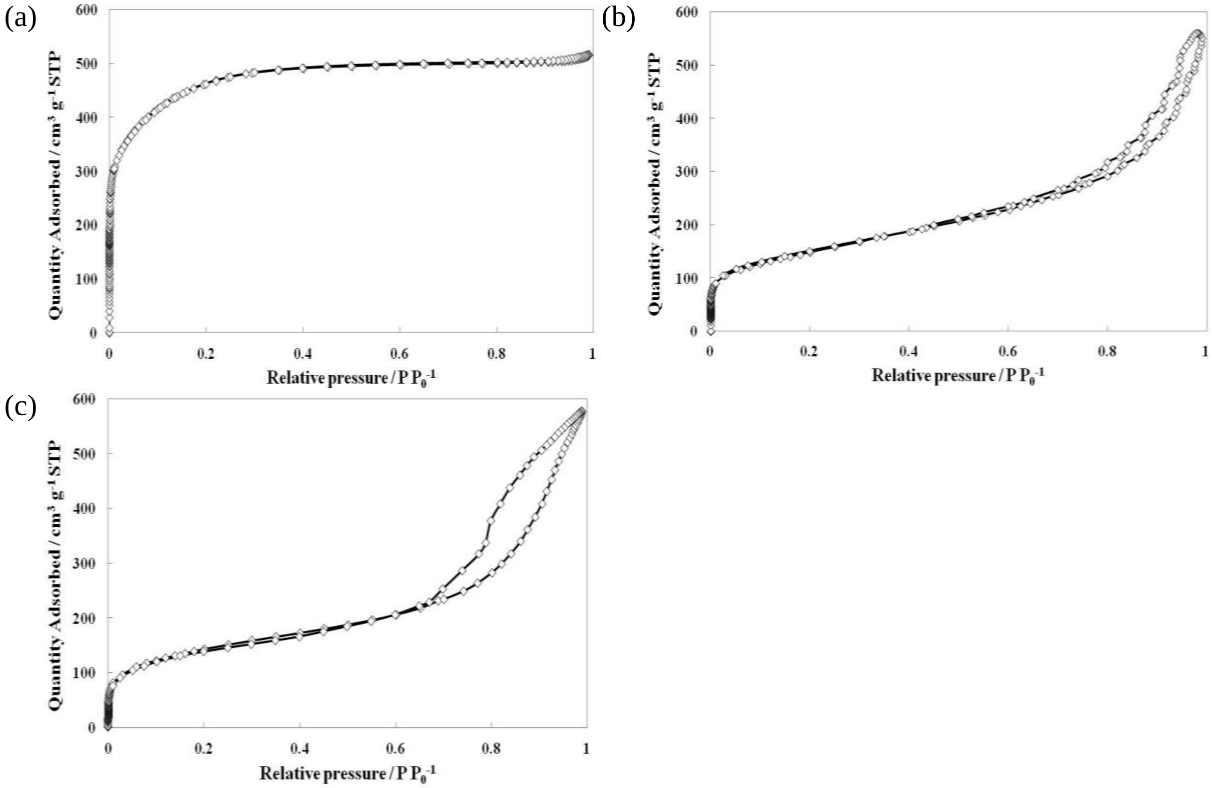

Figure 5.3 Nitrogen adsoprtion isotherms for the carbon electrodes: (a) AC; (b) graphene; and (c) SWCNT

As shown in Figure 5.3 (a), according to IUPAC classification [176], the isotherm of the AC electrode is a type I isotherm, which indicates that the AC is predominantly microporous.

The large amount of adsorption on the AC at very low pressures is due to the micro-pores filling up because of the enhanced adsorbent-adsorbate interactions in the micro-pores, and is distinct from the adsorption that occurs in the meso-pores [177]. In contrast, as shown in Figure 5.3 (b), the graphene electrode exhibits a type II isotherm with type H3 hysteresis loops, which is a characteristic of mesoporous adsorbents. As with the graphene electrode, the isotherm of the SWCNT electrode (Figure 5.3 (c)) is characterized by hysteresis loops, but closes as a type IV with a clearer hysteresis that represents a structural combination of a mesoporous and a macroporous material.

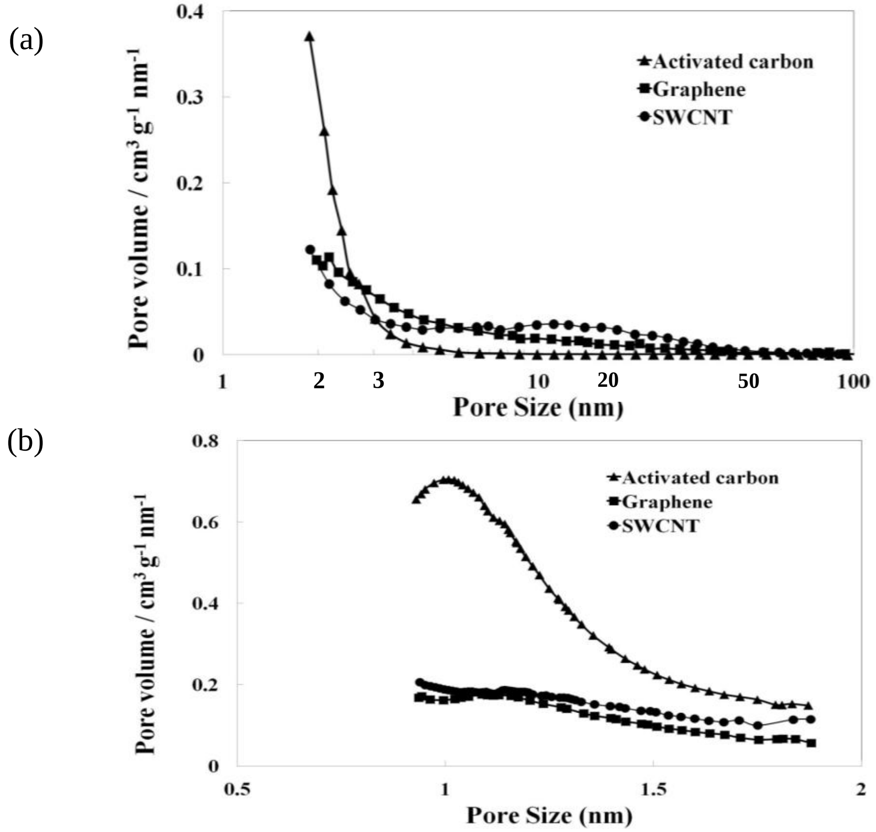

Figure 5.4 Pore volume distributions: (a) within meso-/macropore ranges of 2nm and above, based on the BJH method; and (b) within micropore range under 2nm, based on the HK method

The differences in the nitrogen adsorption isotherms of each electrode are well reflected by the PSD analysis. The pore volumes were calculated using the BJH method for meso- and macro-pores ranging from 2 nm to 100 nm, and the HK method was applied for micro-pores of less than 2 nm, as depicted in Figure 5.4. The results reveal that the AC contains narrowly distributed micro-pores from 1 nm to 3 nm, and that the most pore volumes were obtained from the micro-pore region. In comparison, the pore volumes of the graphene are widely distributed in the meso-pore region, and the volume of meso-pores between 3 nm and 10 nm is greater than in the other electrodes. The SWCNT electrode, which has two peaks, one located below 2 nm and the other between 10 nm and 20 nm, displays the greatest volume of pores larger than 10 nm. The calculations of the BET surface areas, micro-pore areas, external areas, and average pore volumes are summarized in Table 5.1. The t-plot was adopted by the reference to carbon black in order to determine the external surface area which can be defined as the surface area caused by pores larger than a micro-pore.

Table 5.1 Specific BET surface areas, external areas, pore diameters and pore volumes of the AC, graphene and SWCNT electrodes

Electrode	BET surface area (m^2/g)	Micropore area (m^2/g)	External area (m^2/g)	Average pore diameter (nm)	Pore volume [a] (cm^3/g)	Pore volume [b] (cm^3/g)
Graphene	546	40	506	6.2	0.824	0.169
Activated carbon	1558	1053	505	2.1	0.249	0.536
SWCNT	640	59	581	7.0	0.961	0.161

[a]: Pore volumes for meso-pores determined by the BJH method for meso-/macro-pores ranging from 2 nm to 100 nm; [b]: pore volumes for micro-pores as determined by the HK method for micro-pores less than 2 nm.

The micropore area was calculated based on a balance between the BET surface area and the external surface area. The BET surface area of the AC electrode was approximately 1560 m^2/g, which is attributable primarily to its micro-pore area of 1053 m^2/g. The SWCNT exhibited a larger volume for pores between 2 nm and 100 nm, with an external area of 581 m^2/g, and a total surface area of 640 m^2/g. With the value of around 550 m^2/g, the graphene electrode had a lower surface area than either the AC or SWCNT electrode, and the external area of the meso-pores provided the greatest contribution to its surface area. The graphene electrode also has an average pore diameter of 6.2 nm, which is notably larger than that of the AC electrode, at 2.1 nm, while the pore size of the SWCNT is 7 nm: larger than that of either the AC or graphene electrode. Two main structural differences are evident from a comparison of the AC, graphene, and SWCNT electrodes. First, both the SWCNT and graphene electrodes possess a larger pore volume of meso-pores, with a wider PSD that ranges from 3 nm to 50 nm, but with the SWCNT exhibiting a larger pore diameter and volume for pores above 10 nm. Second, the AC electrode has a narrow PSD and a surface area composed mainly of micro-pores (1 nm to 3 nm), resulting in the largest surface area of the three carbon electrodes.

5.3.2 Electrochemical Characterization

Cyclic voltammetry (CV) graphs were produced for the AC, graphene and SWCNT electrodes in 1M Et_4NBF_4/PC electrolytes and are shown in Figure 5.5, which gives rise to several observations. First, all of the electrodes display nearly rectangular shapes without any major Faradaic peaks in the I-V curves, although a tailed line for the current response appears near 2.5 V due to the decomposition of the electrolyte. This result implies that their capacitive behaviors can be attributed primarily to the electric double-layer formation at the electrode/electrolyte interface, which means that no pseudo-capacitance effects are present. Second, it can be clearly observed that the curves corresponding to the graphene and SWCNT electrode are closer to rectangles than the one for the AC electrode. This distinction indicates that the equivalent series resistance is smaller in the graphene and SWCNT electrodes than in the AC electrode, which relates directly to their electrical conductivity and structural properties, such as PSD.

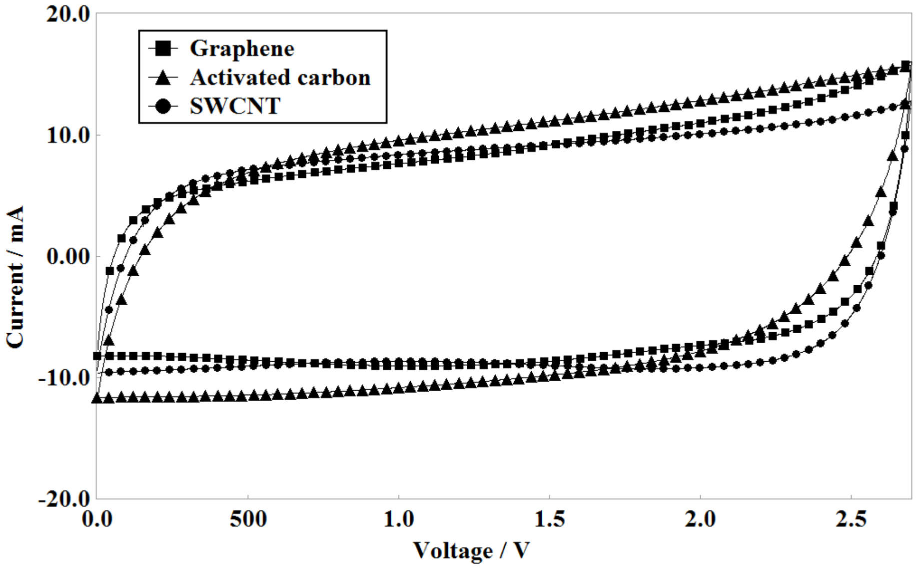

Figure 5.5 Cyclic voltammetry curves for the AC, graphene and SWCNT electrodes in an organic 1M Et_4NBF_4/PC electrolyte, produced with a scan rate of 20 mV/s

To address the effects of PSD, further voltammetry tests were conducted using a variety of electrodes at four different scan rates: 5 mV/s, 10 mV/s, 20 mV/s, and 40 mV/s. As shown in Figure 5.6 (a), the voltammogram for the AC electrodes begin to distort when the scan rate is increased, which indicates that the response of the AC electrode to high operating frequencies is slow and that their performance declines for operations involving faster ion chargeing/discharging. In contrast, Figure 5.6 (b) and (c) reveal that the shapes of both the graphene and SWCNT electrode curves are much less distorted with increased scan rates, which indicates better ion accessibility at high-voltage scan rates. The specific capacitances the calculated based on these CV measurements are listed in Table 5.2.

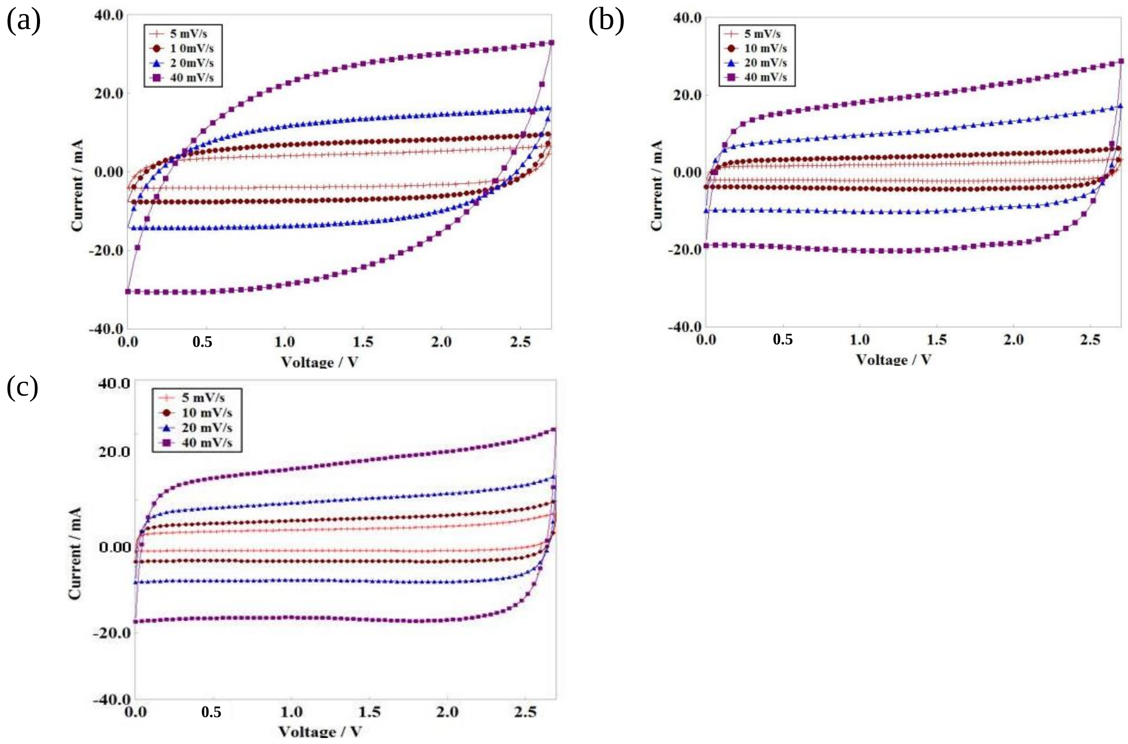

Figure 5.6 Cylic voltammetry curves: (a) for AC, (b) graphene, and (c) SWCNT electrodes in 1M Et_4NBF_4/PC electrolyte at different scan rates

Although the graphene and SWCNT electrodes exhibit a smaller capacitance at the scan rate of 5 mV/s, around 90 F/g and 96 F/g, respectively, they maintain their capacitance with a 90 % retention rate when the scan rate is increased to 40 mV/s. In comparison, the value for the AC electrodes changes significantly with the scan rate, with the highest capacitance of 132 F/g at 5 mV/s and the lowest capacitance of 89 F/g at 40 mV/s. Nevertheless, the graphene and SWCNT electrodes display a smaller voltammograms area, i.e., a lower capacitance, than the AC electrodes. This result arises directly from the smaller specific surface area of both of these electrodes compared to that of the AC electrodes, as mentioned earlier.

Table 5.2 Variation of the specific capacitance (F/g) calculated from cyclic voltammetry measurents with 1M Et_4NBF_4/PC was the electrolyte and with different scan rates

Scan rate (mV/s)	Activated carbon (F/g)	Graphene (F/g)	SWCNT (F/g)
5	132.2	90.9	96.5
10	109.8	89.5	92.9
20	96.5	87.2	89.2
40	88.8	82.3	86.7

With regard to the effects of pore volume effects, the highly microporous AC electrodes would be expected to restrict ion transport when the scan rate is too fast, due to the shorter ion migration period at higher frequencies. This effect can have the direct result of creating a greater resistance to ionic charging. The meso-pores of both the graphene and the SWCNT electrodes, on the other hand, favor ionic penetration through their porous networks, resulting in lower resistances than with the AC electrodes at high scanning rates. EIS was performed in order to shed light on the effects of meso-pores and micro-pores on the frequency-dependent resistive and capacitive behaviors of AC, graphene, and SWCNT electrodes.

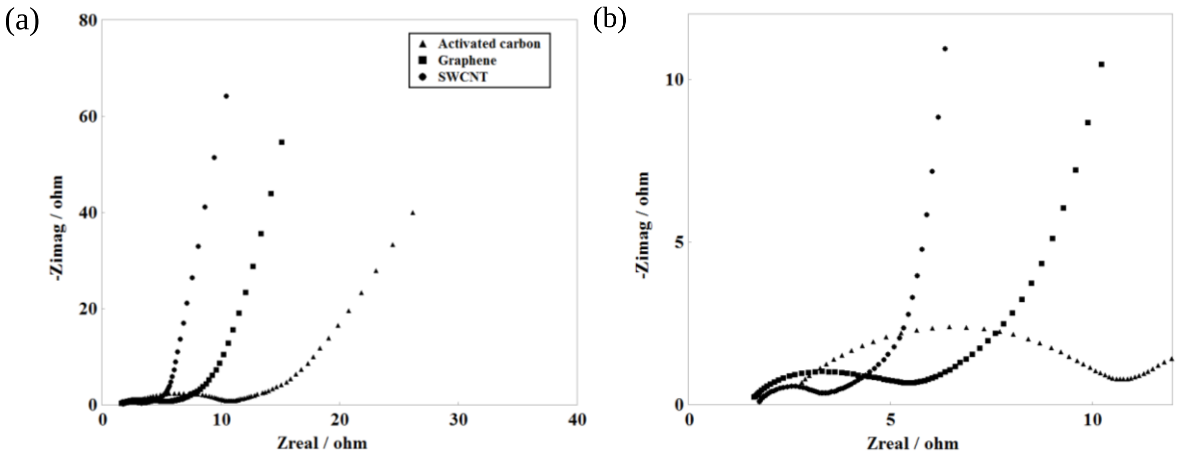

Figure 5.7 (a) Nyquist plots of AC, graphene and SWCNT electrodes in 1M Et_4NBF_4/PC with (b) the enlarged image

For this purpose, the series resistance (R_S) was first determined based on the intercept at the real impedance axis of the Nyquist plots shown in Figure 5.7. The figure shows that both the graphene and SWCNT electrodes exhibit a lower R_S value than the AC electrodes, which is directly attributed to the different intrinsic electrical conductivities of the electrodes. Subsequently, the semi-circle of the SWCNT electrode occurs at a higher frequency and with a smaller diameter, which indicates a lower interfacial resistance (R_{int}). This value of R_{int} is closely associated with the kinetics of ion transport at the electrode/electrolyte interface [175]. A lower R_{int} usually leads to smaller impedance against ion migration at the double-layer interface, which suggests better dynamic performance from the graphene and SWCNT electrodes. In the low frequency region, all of the electrodes exhibit an ideal capacitive behavior with a nearly linear line. However, the slope of the graphene and SWCNT electrodes is larger than that of the AC electrodes, especially in the case of the SWCNT electrodes which contain larger pores. These results suggest that the dynamic impedance behavior of two electrodes strongly correlates to their surface and micro-structural properties.

If an electrode is characterized by substantial porosity in the micro-pore range, the access time for the electrolyte ions to be adsorbed on its surface area must be longer. Narrow and deep pores are therefore relatively inaccessible for ions during short electrical impulses and for high-frequency currents, resulting in greater resistance levels for microporous electrodes. Such deep micro-pores also contribute to the capacitive behavior of an electrode with a high RC delay time and, as a result, its capacitance drops with increased charging frequencies. This effect is illustrated by the Bode plots included in Figure 5.8, which demonstrate the changes in real capacitance (C') and imaginary capacitance (C″) with frequency. Frequency-dependent capacitance C'(ω) generally relates directly to the kinetic processes and ion migration in the porous network of an electrode. EIS measurements are widely used for demonstrating how many solvated ions can reach the pore surface at a given frequency.

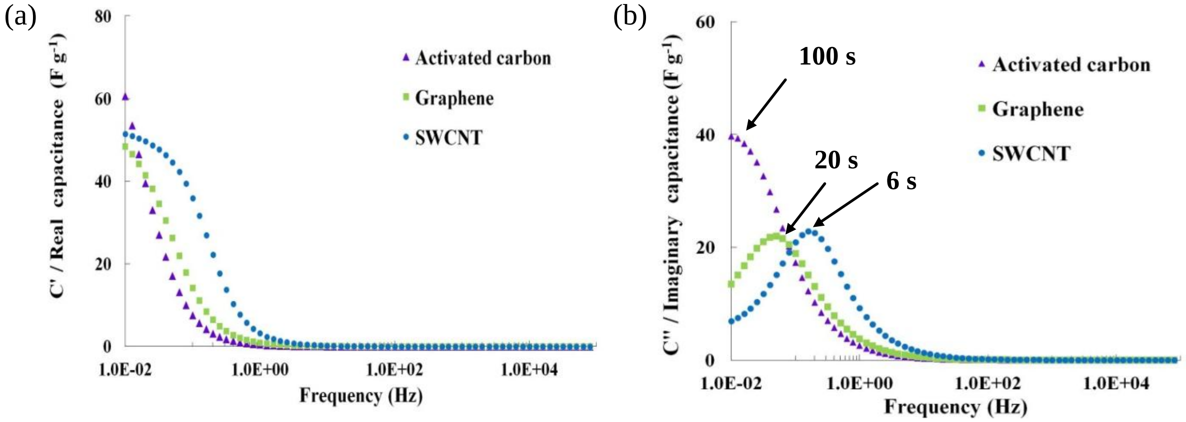

Figure 5.8 Bode plots for AC, graphene and SWCNT electrodes in 1M Et_4NBF_4/PC

As shown in Figure 5.8 (a), at lower frequencies such as 0.01 Hz, nearly the entire pore surface of the electrodes is accessible to electrolytic ions, and their specific capacitances are the highest. With increased frequencies, the Bode curves show a decrease in capacitance, which is more significant between 0.01 Hz and 1 Hz. The capacitance levels of electrodes become quite small when the frequency is greater than 100 Hz. It can also be observed that the capacitance of the SWCNT electrodes decreases at a slower rate than does that of the other electrodes. This discrepancy indicates that, for the given frequency, the ion migration to the active surface of the SWCNT electrodes is more efficient than that of the other electrodes due to the larger pores in the SWCNT network. An additional factor is that the effect of pore size on ion transport is of even greater significance in the case of the AC electrodes because of their smaller pores. Figure 5.8 (b) demonstrates the evolution of the imaginary capacitance (C″) relative to frequency. The maximum of C″ is a characteristic of the capacitive system, which roughly describes the moment when the system changes from purely resistive to purely capacitive [178]. The frequency f_0 that corresponds to the maximum C″ represents a time constant, $\tau = 1/ f_0$, which indicates quantitatively how quickly an EDLC device can respond to the charging/discharging cycles at the specified frequencies. As shown in Figure 5.8 (b), the SWCNT electrodes are characterized by a shorter time constant than the other electrodes. This finding confirms the distinctive behaviors of the three types of electrode over different charging/discharging cycles, which are the result of their differing porous structures. Since larger meso-pores can more easily be penetrated by electrolytic ions, they contribute significantly to faster responses during high-frequency charging/discharging, and hence, the SWCNT electrodes are associated with a shorter time constant. As well, the existence of a large proportion of meso-pores enables the graphene and SWCNT electrode to produce more constant capacitances at high scan rates than the AC electrodes, as discussed in relation to the CV measurements.

5.3.3 Thermal Characterization

Figure 5.9 shows cyclic voltammograms (CV) for a unit cell recorded at 20 mV/s for the AC, graphene, and SWCNT electrodes at the range of operating temperatures. With respect to the effects of temperature, all of the electrodes exhibit a larger CV area as the operating temperature increases, including a greater capacitance at a higher temperature. This finding can be attributed to a greater kinetic activities and diffusion of ions at elevated temperatures, resulting in a greater charge accumulation. Conversely, at lower temperatures, the current profile of CV curves becomes distorted from the ideal rectangular shape, and shows a slower rise, with the rectangle having rounded corners at the beginning of the charging/discharging processes.

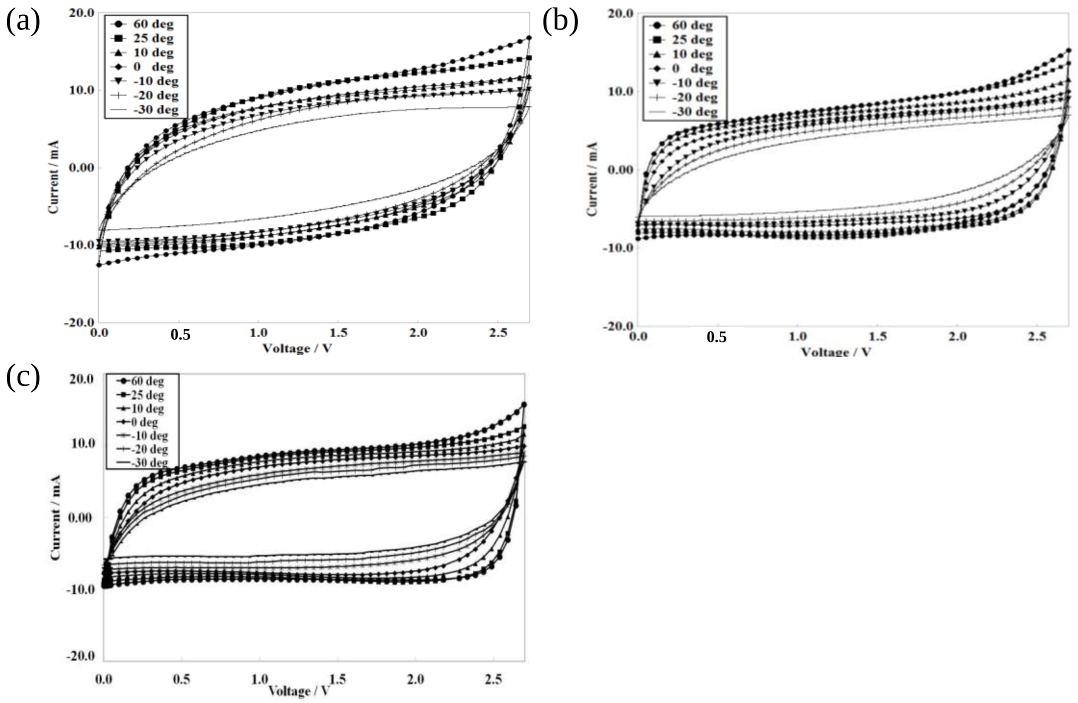

Figure 5.9 Cyclic voltammetry at a scan rate of 20 mV/s for (a) activated carbon, (b) graphene and (c) SWCNT electrodes at operating temperatures from -30 to 60 ℃

This behavior is due to an increase in internal resistance as the temperature goes down [179]. However, the AC electrodes exhibit only a slight decrease in these rounded corners at temperatures from -20 ℃ to 25 ℃, while both the graphene and SWCNT electrodes show a steady decrease over the entire temperature range. These results indicate that decreases in the rates are dependent on temperature, which cause an apparent reduction in capacitance and an increase in internal resistance at lower temperatures, especially for the AC electrodes.

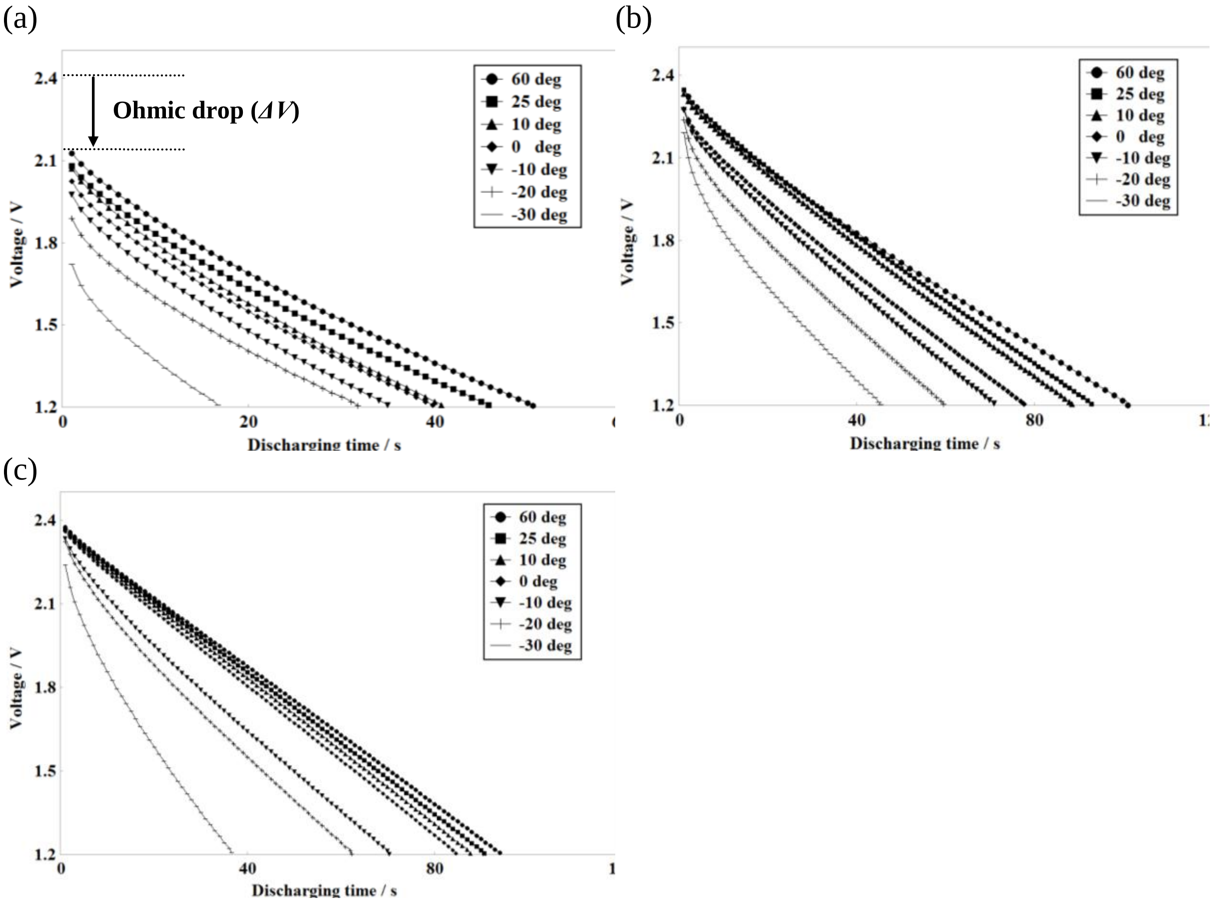

Figure 5.10 Discharging process at constant current (a rat of 30 C) and ohmic drop (ΔV) for (a) activated carbon, (b) graphene, and (c) SWCNT electrodes in 1M Et_4NBF_4/PC electrolyte at operating temperatures ranging from -30 ℃ to 60 ℃

Constant charge/discharge (CCD) measurements further confirm the increase in capacitance at elevated temperatures and the increase in internal resistance with decreasing temperatures. Figure 5.10 shows the discharge curves for activated carbon, graphene and SWCNT electrodes at each operating temperature from -30 ℃ to 60 ℃. From these curves, the specific capacitances were determined as follows:

$$\text{Specific capacitance (F/g)} = \frac{\Delta I \cdot \Delta t}{(V_{max} - V_{min}) \cdot m} \quad (53)$$

where ΔI is the applied constant current of the discharge, Δt is the discharging period, V_{max} is equal to V_{rated} (2.4 V in 1M Et_4NBF_4/PC), $V_{min} = \frac{1}{2} V_{max}$, and m is the weight of the active materials in the cell. The internal resistance was also calculated by measuring the ohmic drop caused by the discharging curves, as follows:

$$\text{Internal resistance } (\Omega) = \frac{\Delta V}{\Delta I} \quad (54)$$

where ΔV is the initial voltage (ohmic) drop at the beginning of the discharging process.

Figure 5.11 presents the resulting plots of the specific capacitance (F/g) and internal resistance (Ω) values calculated for each type of electrode based on the CCD curves shown in Figure 5.10. In comparison to the specific capacitance shown in Figure 5.11 (a), over tested temperature range tested, AC provides the greatest specific capacitance compared to the other types of electrodes, which is direct result of its larger surface area as indicated in Table 5.1. Regarding the effect of temperature on capacitance, as with the CV measurements, the AC shows a relatively small decline in capacitance, from 82 F/g to 65 F/g for temperatures of 60 ℃ to -20 ℃, whereas the capacitance of graphene decreases steadily from 70 F/g to 46 F/g when the temperature is lowered. As with the graphene, the capacitance of the SWCNT electrodes ranges from 72 F/g to 50 F/g. Figure 5.11 (b), on the other hand, shows an increase in resistance for all electrodes as the operating temperature decreases, with the AC exhibiting much larger internal resistance than either graphene or SWCNT over all temperatures.

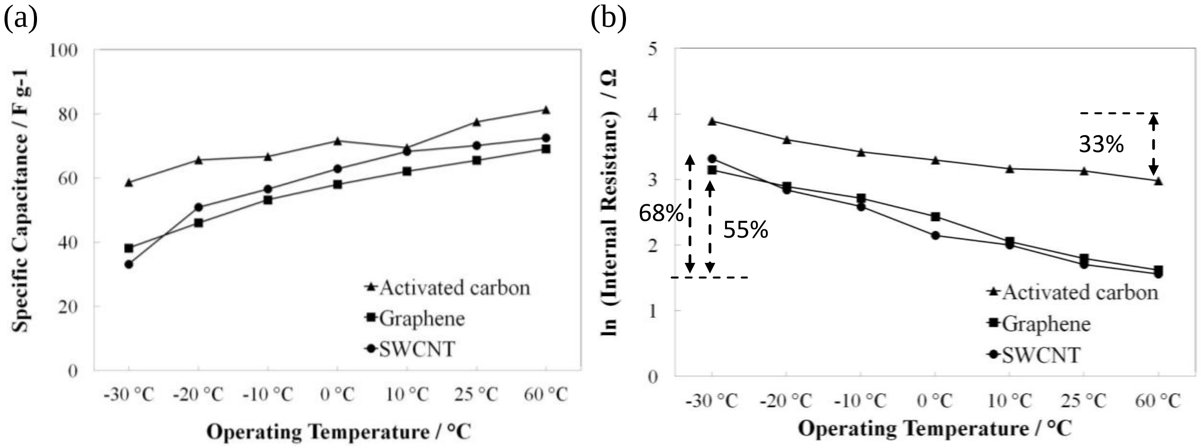

Figure 5.11 Plots for the activated carbon, graphene, and SWCNT electrodes based on the CCD cureves: (a) comparison of specific capacitance levels; (b) the differences in internal resistance with temperatures

This effect is mainly due to the lower electrical conductivity of AC compared with either graphene or SWCNT [27]. However, with respect to the effect of temperature on internal resistance, a relatively larger variation is evident for the graphene and SWCNT electrodes: in the order of 55 % for the graphene and 68 % for the SWCNT. The AC, however, displays a deviation of 33 % over the entire operating temperature range. These findings indicate that the influence of temperature on the AC electrodes is less than for the others types of electrodes, and that the SWCNT is relatively more sensitive to temperature than the graphene. Variations in the resistance and capacitance can also result in a reduction in the energy/power density, as depicted in Figure 5.12. As the temperature decreases, all of the electrodes show a decrease in power/energy densities. The maximum power density is achieved between 400 W/kg and 600 W/kg over all temperatures, while the maximum energy density obtained from the discharge curve run at 60 ℃ ranges from 6 Wh/kg to 10 Wh/kg. In the case of power density, the AC electrodes exhibit a significantly greater deviation in power density than other electrodes. This observation can be attributed to the fact that the AC electrodes have a much lower magnitude of dV due to the larger ohmic drop, which creates a significant decrease in power density.

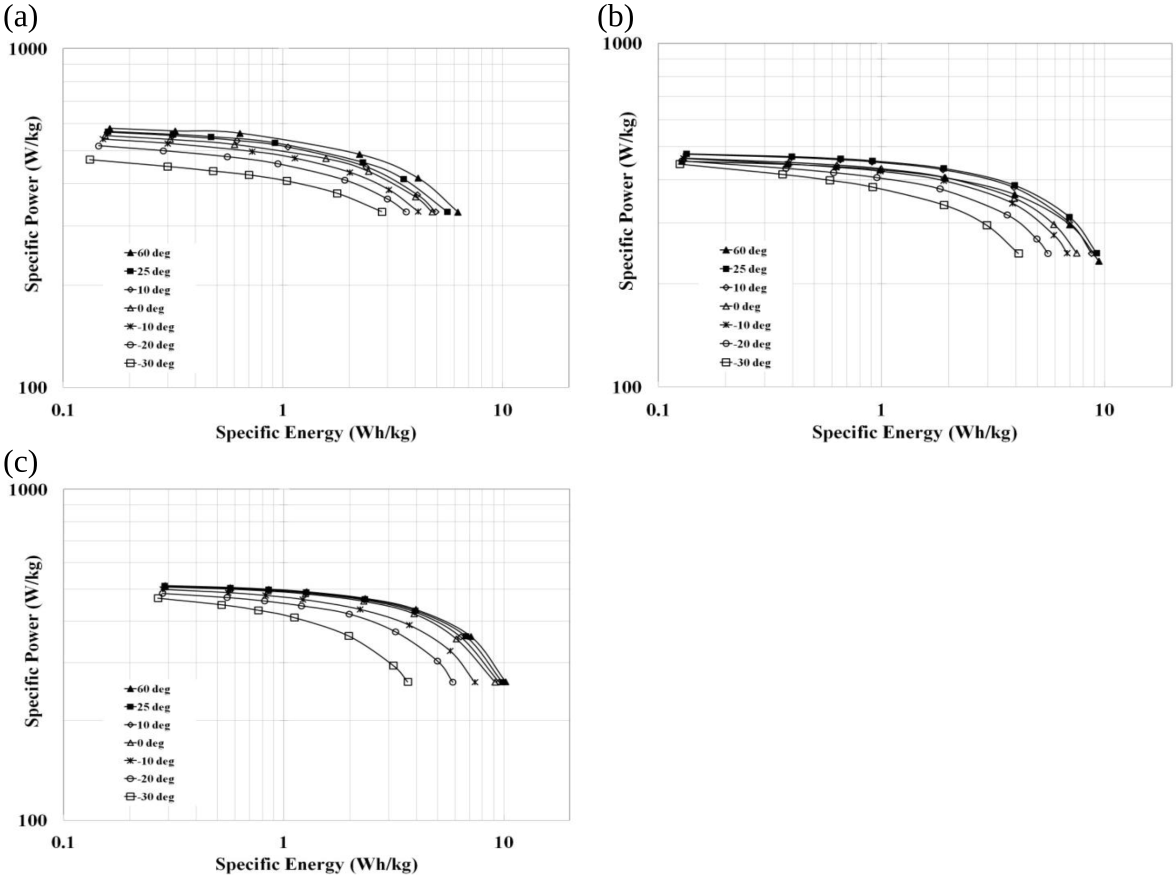

Figure 5.12 Ragone chart with specific power / energy density for (a) activated carbon, (b) graphene and (c) SWCNT-based EDLCs

On the other hand, as the temperature goes down, both the graphene and SWCNT electrodes show a gradual decrease in the energy density while a linear decrease can be observed for the AC electrodes. For operations involving a low power density (running from a low voltage, e.g., 1.2 V), the energy density is consumed quickly as the temperature decreases, especially for SWCNT electrodes.

EIS measurements were used for acquiring a more detailed understanding of on the capacitive/resistive behavior of the electrodes as a function of temperature and frequency. From the Bode plots of the real capacitance (C_{real}) shown in Figure 5.13, it was found that the C_{real} values decrease with increasing frequency and decreasing temperatures over the frequency ranges. At ultralow frequencies, the capacitance tends to remain constant relative to temperature, and this phenomenon can be clearly observed for the SWCNT electrodes. The capacitance is more influenced by temperature in the intermediate frequency range: between 0.01 Hz and 1 Hz. This variation is considerably greater in the results for the graphene and SWCNT electrodes than in those for the AC electrodes. In the case of the SWCNT electrodes, their capacitance decreases significantly as the temperature drops. This result is similar to the deviation in capacitance demonstrated by the CCD measurements, and becomes increasingly obvious under the frequency operation. To enable a comparison of the practical capacitance values that were measured mainly at 0.1 Hz, the capacitance retention of the electrodes was calculated as follows:

$$\text{Capacitance retention (\%)} = \frac{C_T}{C_{25}} \times 100 \qquad (55)$$

where C_T represents the capacitance at each temperature, and C_{25} indicates the value at 25 ℃. The results are listed in Table 5.3.

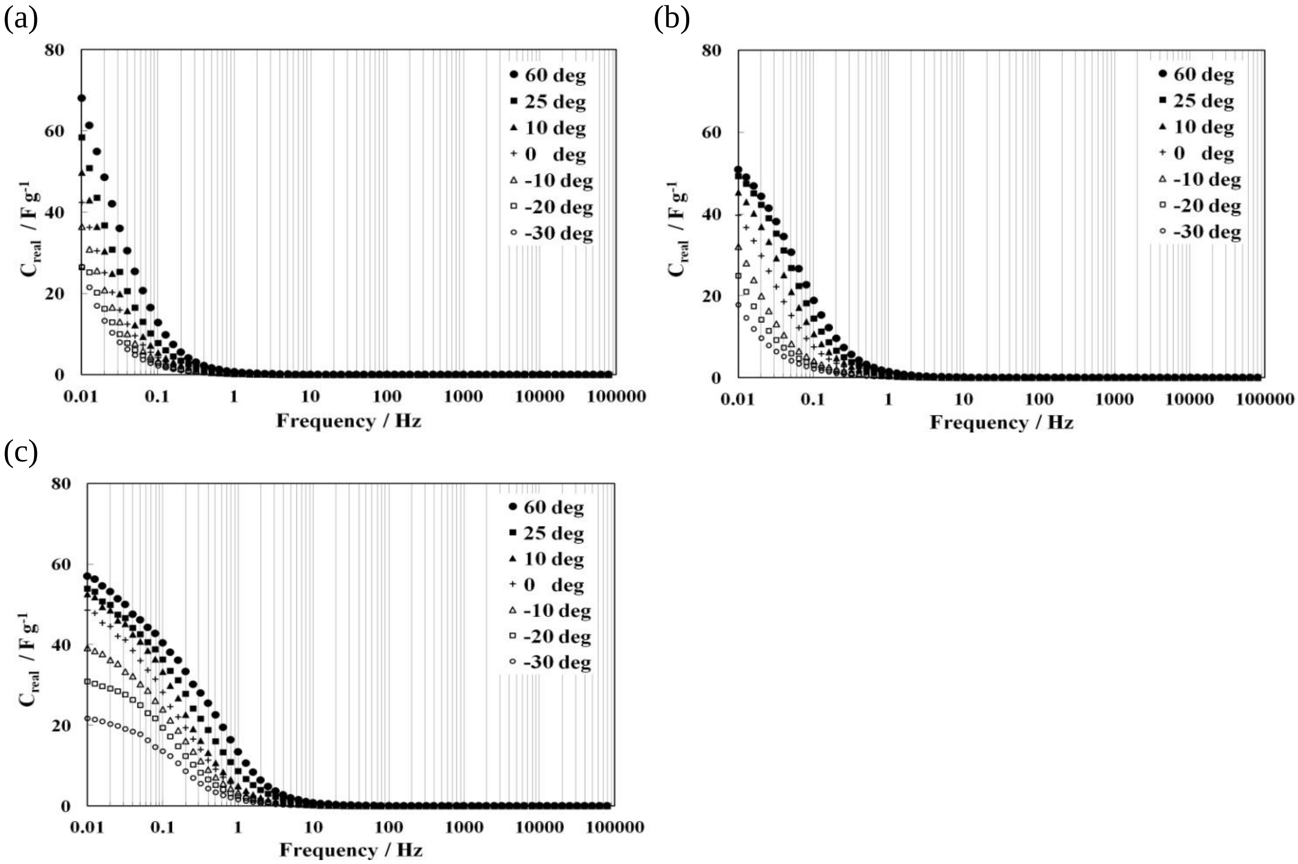

Figure 5.13 Bode plots of real capacitance for (a) activated carbon, (b) graphene and (c) SWCNT electrodes

Table 5.3 Values measured for C_{real} (F/g) from Bode plots at 0.1 Hz for activated carbon, graphene, and SWCNT electrodes

Temperature (℃)	Activated carbon (F/g)	Graphene (F/g)	SWCNT (F/g)
-30	33.5	17.8	21.1
-20	40.0	24.9	30.2
-10	49.2	32.0	39.2
0	55.2	39.7	48.6
10	63.0	45.3	52.6
25	72.8	49.3	53.9
60	79.0	52.6	56.9

The result shows that, relative to the other types of electrodes, the AC exhibits the superior capacitance retention with changes in temperature. The C_{real} of AC varies by roughly 46 % within a temperature range of -30 ℃ to 60 ℃ while the graphene and SWCNT results reveal capacitance retention values of about 35 % and of 39 %, respectively (see Figure 5.15 (a)). On the other hand, as can be seen in the Bode plots for real impedance (Z_{real}) in Figure 5.14, decreasing temperature causes an increase in the Z_{real} values over all frequency ranges and for all electrodes. A comparison of the plots shown in Figure 5.14 reveals that the AC exhibits linearly increasing Z_{real} values with reduced temperatures while the graphene and SWCNT display an exponential increase in the Z_{real} values. This phenomenon is more significant at low frequencies ranging from 0.01 Hz to 1 Hz.

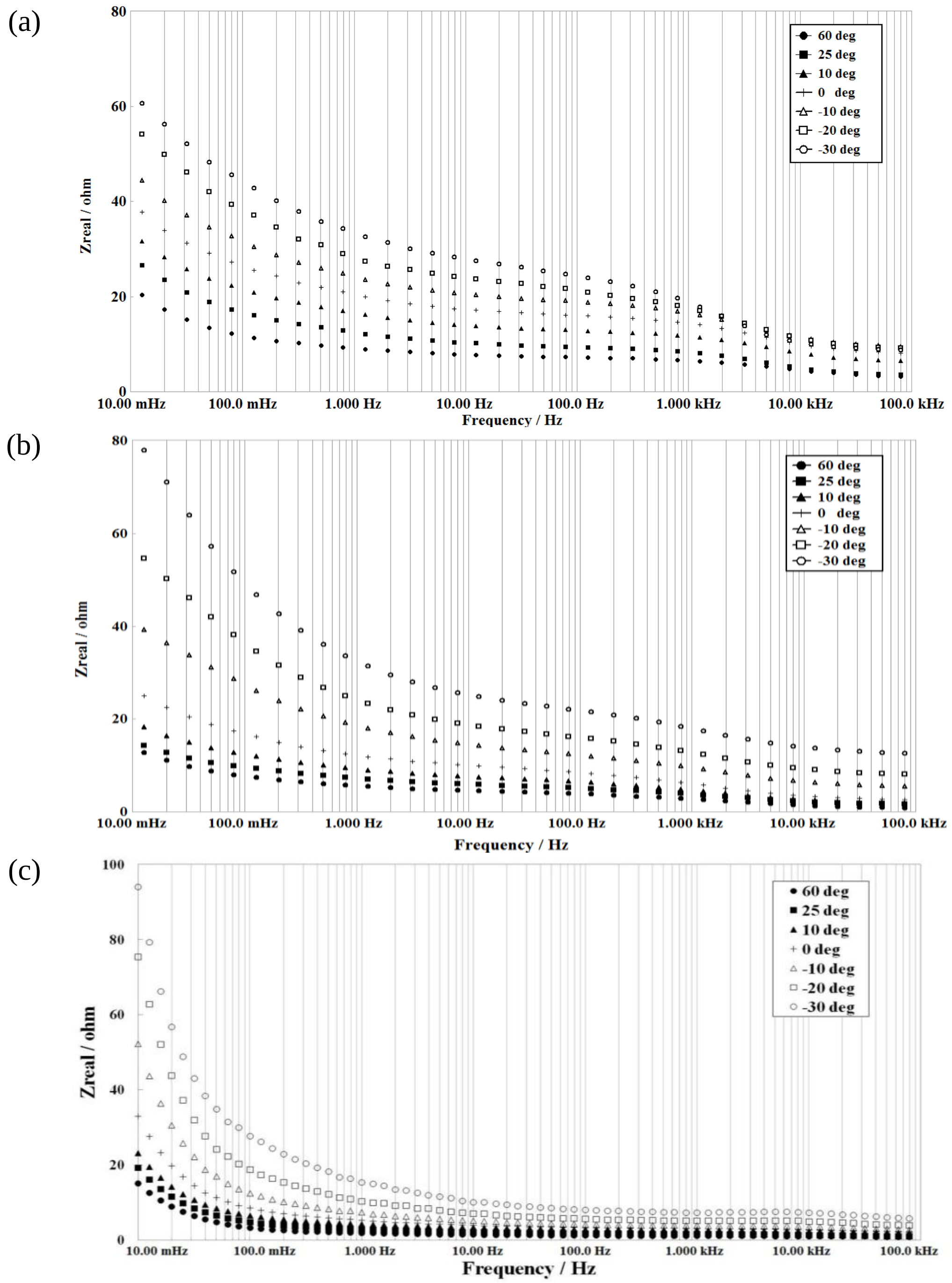

Figure 5.14 Bode plots of real impedance for (a) activated carbon, (b) graphene and (c) SWCNT electrodes

More detailed plots of the impedances measured at 0.1 Hz are provided in Figure 5.15 (b). The Z_{real} values of the AC increase from 22 Ω to 65 Ω when the temperature decreases from 60 ℃ to -30 ℃. The graphene exhibits a greater Z_{real} variation, increasing from 14 Ω (at 60 ℃) to 81 Ω (at -30 ℃) while the SWCNT shows the largest change in Z_{real} values ranging from 15 Ω (at 60 ℃) to 94 Ω (at -30 ℃). A similar trend is evident for the internal resistance values observed in the CCD measurements, leading to the conclusion that with the graphene and SWCNT, the resistance is more sensitive to temperature change than with the AC.

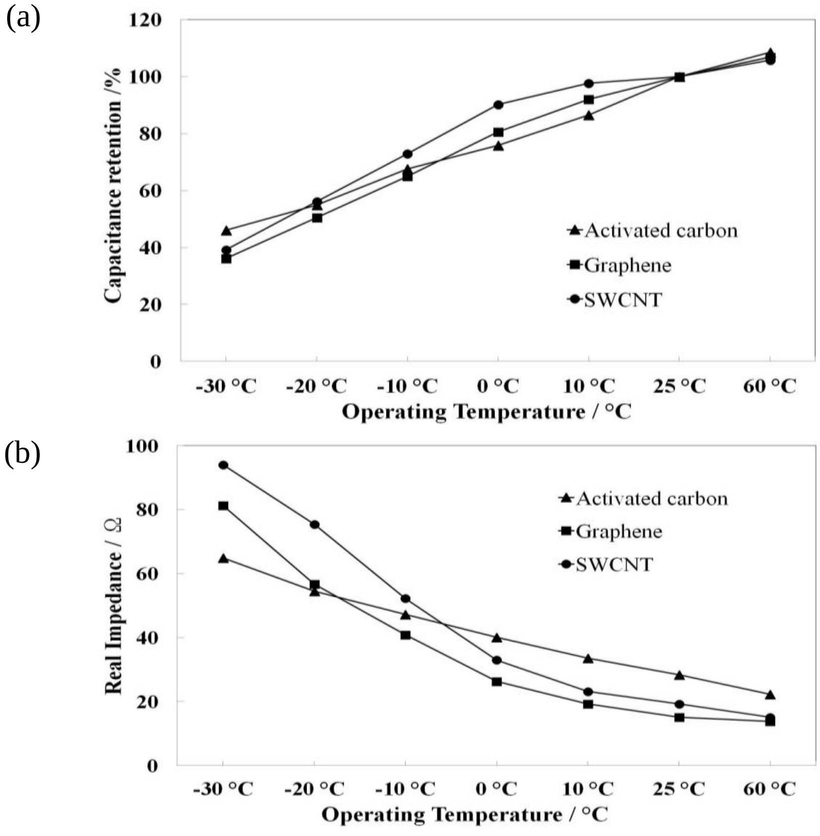

Figure 5.15 Plots of the measurement results for the activated carbon, graphene and SWCNT electrodes with respect to (a) capacitance (C_{real}) retention and (b) comparative Zreal values (measured at 10 mHz from Bode plots)

These differences in temperature dependency among the three types of electrode can be correlated with their structural characteristics, including the discrepancy in pore width and distribution. According to simulation studies [180, 181], for narrow pores that are close to the ion diameter, the capacitance tends to exhibit smaller deviations with the applied voltage due to the maximum saturation of ion adsorption in narrow pores and enhanced ion's separation. In contrast, the dependence of the capacitance on pore size becomes relatively greater as pore size increases due to the interference of the overlapping electric double layers. Another study revealed [182] that a wider pore distribution leads to observations of more pronounced porous characteristics with frequency-dependent impedances due to differing degrees of ionic penetrability into the pores. The impedance of an electrode with a wide PSD increases more rapidly with frequency, with the result that the energy loss at frequency-operation becomes greater. This phenomenon would be more critical and has greater significance at low temperature, as illustrated through the schematic representation in Figure 5.16.

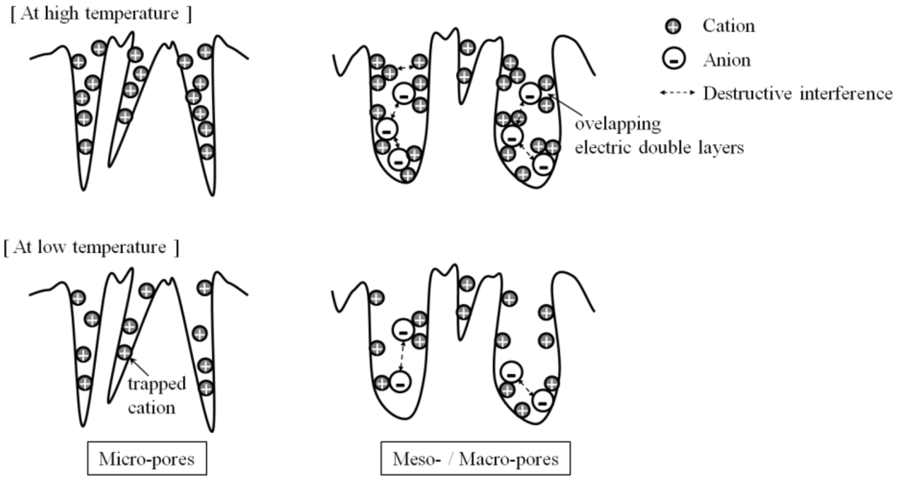

Figure 5.16 Schematic diagrams of ion adsorption and the interactions associated with micro-pores and meso-/macro-pores at varied temperatures

The possibility of an excess charge near the meso-pores of electrodes that have a broader PSD creates an increase in the stabilization time and in the energy barrier that acts against the distribution of ion movement in wider pore ranges. As the temperature drops, the decreased kinetic energy caused by lower temperatures leads to a reduction in the number of reactive ions in a pore, but the effect of interference between ions in large pores remains negative with respect to the formation of a double layer and the consequent significant deviation in impedance, which is largely dependent on temperature and frequency. In contrast, for the AC electrodes that have a narrow PSD with respect to micro-pores, the micro-pores contains fewer ions than the meso-pores, but the ion movement into the pores is mostly unchanged with temperature due to the smaller space in the deeper parts of the pores (i.e. shorter distance for ionic movement). The ions are solidly trapped into the smaller pores, which leads to less change in kinetics with temperature. The AC therefore exhibits less Z_{real} temperature dependence, and this effect becomes more dominant at lower temperatures.

To interpret the thermal characteristics of the kinetic and diffusion reactions in the three different types of electrodes, an EIS spectrum was simulated using the previously proposed equivalent circuit model presented in Figure 4.2 (c). This model provides impedance values for kinetic (R_{int}) and diffusion processes, and these rate processes are associated with specific activation energies. Accordingly, each impedance simulated at 10 mHz was processed, then it relates to the activated energy (G) according to the Arrhenius equation [41, 179]. The logarithms of R_{int} and W were plotted against the reciprocal of the temperature in K for the AC, graphene and SWCNT electrodes, as shown in Figure 5.17. Over the entire temperature range, all of the electrodes display comparable resistances values (W) for diffusion. On the other hand, in the case of the R_{int}, the AC electrode values range from 1.7 Ω to 2.4 Ω and from 2.7 Ω to 3.6 Ω for high (60 ℃ to 0 ℃) and low (0 ℃ to -30 ℃) temperature regions, respectively. The graphene results vary from 1.0 Ω to 1.8 Ω and from 2.3 Ω to 3.4 Ω for the same respective temperature regions while the SWCNT findings range from 0.1 Ω to 1.2 Ω and from 2.4 Ω to 3.9 Ω, respectively. Regardless of temperature, the AC electrodes show a larger R_{int} than the other electrodes, but they display a small deviation associated with temperature, as revealed by a comparison of the (a), (b) and (c) sections of Figure 5.17. From this type of Arrhenius plot, the activation energy of the kinetic (G_K) and diffusion processes (G_D) can be calculated. For temperatures ranging from 0 °C to 60 °C, the SWCNT electrodes possess 3.11 kJ/mol of G_K, which constitute the largest values compared to the other electrodes (1.95 kJ/mol for AC, 2.17 kJ/mol for graphene). With respect to G_D, the SWCNT electrodes show a slightly lower value of around 1.17 kJ/mol while the values of the other electrodes (1.69 kJ/mol, 1.75 kJ/mol) are similar. However, in a temperature range of 0 °C to - 30 °C, the G_K for SWCNT shows a significantly large value of 7.55 kJ/mol, followed by graphene at 4.49 kJ/mol, which is greater than for the AC (3.02 kJ/mol). In this temperature region, the G_D values range from 3.0 kJ/mol to 3.5 kJ/mol for all types of electrodes. The characteristics of the G_D values indicate that the diffusion process (G_D) is determined primarily by the properties of the electrolyte, so that the values can be similar for all types of electrodes when the same electrolyte is used. However, the G_K value is related to the ion kinetics at the interfaces between the electrode and the electrolyte. As a result, the SWCNT displays greater activation energy than the others with respect to ionic kinetics (G_K) as the temperature decreases, especially below 0 °C. This finding means that the SWCNT needs a higher level of kinetic energy in order to overcome the resistance in the interfacial double-layer regions, which is associated mainly with a wider PSD at the meso-pores range, as discussed in previous sections.

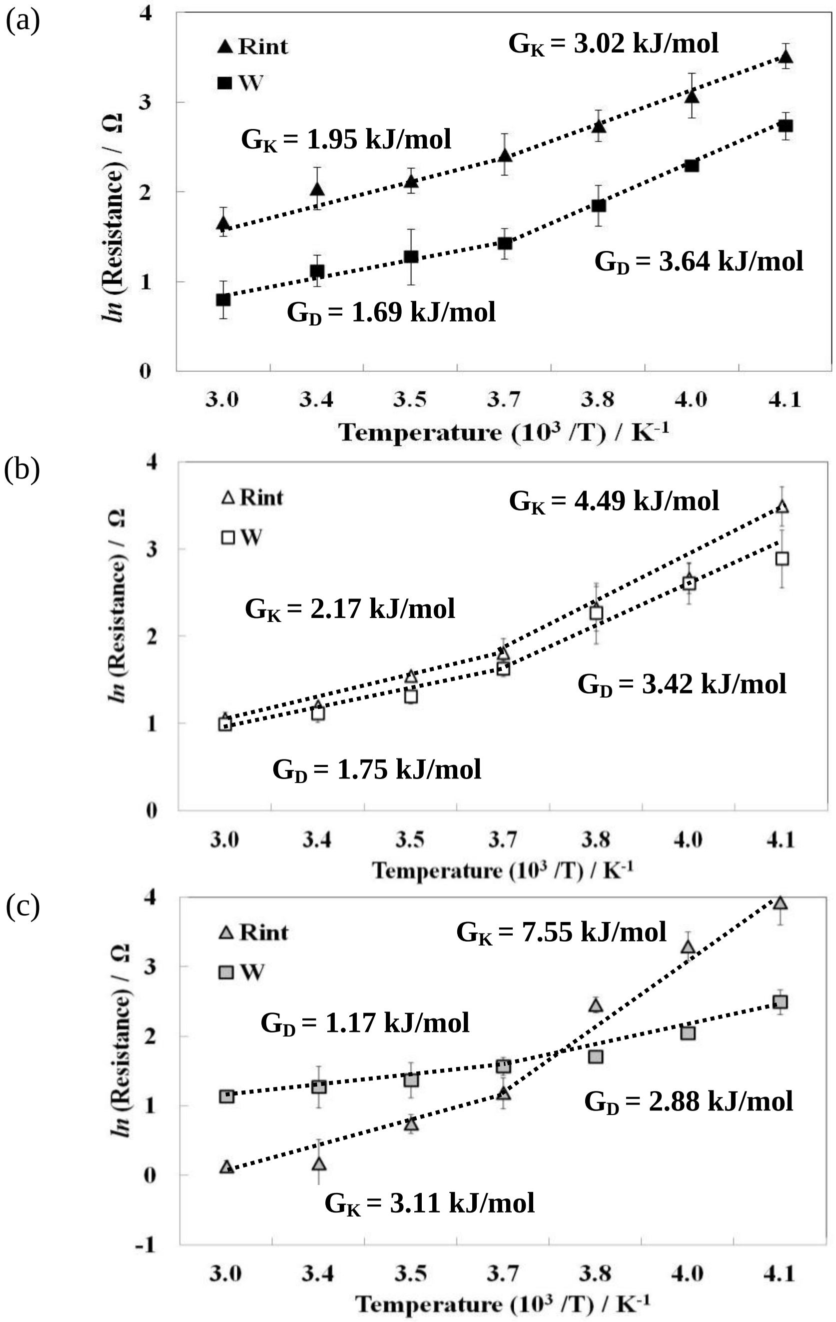

Figure 5.17 Arrhenius plots of the temperature dependency of kinetic and diffusion resistances in (a) activated carbon, (b) graphene and (c) SWCNT electrodes

5.4 Summary

The work presented in this thesis has involved the investigation of the dependence of electrochemical characteristics, especially dynamic and thermal responses, of the AC, graphene, and SWCNT electrodes on their micro-structures, as represented by their distinguishable surface area, pore size and pore size distribution. To verify the role of porous carbon electrodes in supercapacitor performance, their frequency- and temperature-dependent capacitive and resistive behavior has been characterized and correlated with the microstructures of the electrodes. Both the graphene and SWCNT electrodes exhibit lower interfacial resistance, better high-frequency performance and faster response periods in a high-frequency domain, due to the relatively high pore volumes in their meso-pore ranges, between 3 nm and 50 nm, with a wide PSD. However, they exhibit larger variations in resistance (maximum 55 % or 70 % variation for temperatures ranging from -30 ℃ to 60 ℃) and lower retention of capacitance correlated with temperatures. It is evident that the presence of dominating meso-pores in an electrode makes its surface area more accessible to electrolytic ions even at high-frequency operation, but relatively larger pores increase interference between ions, which has a negative effect on the double-layer formation at low temperatures.

In comparison, the activated carbon electrodes display a higher resistance and a longer current response period, which are attributable to the dominance of micro-pores (less than 2 nm), with a narrow PSD. Microporous AC however shows a weak dependence of capacitance and resistance (maximum 33 % variation) on temperature, and minimal temperature influence on ion kinetics at the double-layer interface, resulting in stable performance, i.e., less degradation of energy density. Differences in resistive characteristics become more significant in the frequency domain with decreasing operating temperature. This finding corresponds to the fact that the AC exhibits lower kinetic activation energy of G_K, especially below 0 ℃, which can be attributed to the probability of the existence of stabilized ions in a narrow micro-pore range. Enhancements in porous electrode performance can be achieved through the optimization of pore structure. The effects of frequency and temperature on ion movement into pores should also be considered as an important factor when an EDLC device is designed for operation in harsh environments. Therefore, a thorough understanding of the dependence of capacitance and resistance on electrodes that involve the micro-pore to meso-pore ranges can be expected to facilitate the development of high-performance porous carbon-based electrodes for EDLC devices.

Chapter 6 Characterization of Thermal Behaviors with Electrolytes

6.1 Introduction

The electrolyte, e.g. aqueous, organic and ionic liquid, plays an important role in governing the rate capability, and energy density of a device since the stored energy is directly dependent on the properties of an electrolyte including solution stability, conductivity, ionic mobility and diffusivity [17]. Currently, organic (non-aqueous) and aqueous solutions are commonly used as electrolytes in commercial products to achieve a wide voltage range at low resistances. In general, the non-aqueous electrolyte has a higher internal resistance than aqueous electrolytes, which causes a decrease in their power density. Nevertheless, non-aqueous electrolytes are preferred rather to aqueous ones in commercialized EDLC devices because of their wider potential window in operation; a wider potential window leads to increased energy density. On the other hand, aqueous electrolyte is less likely to explode at high temperature and they exhibit lower internal resistances, larger capacitances and higher efficiencies. Accordingly, in order to develop EDLC devices for specific applications and meet their requirements, not only is a suitable electrolyte needed, but a better understanding of the electrolytes' thermal properties is also necessary. Of particular interest are the effect of temperature on the kinetics (charge transfer), diffusion of ions and bulk electrolyte processes, which are crucial to determine the specific capacitance and the internal resistance of an EDLC [144, 170].

The goal of this work is to systematically study the performances of two representative electrolytes, namely aqueous (H_2SO_4) and organic (Et_4NBF_4/PC) ones, using a specified characterization procedure. The effects of temperature on capacitance retention, energy and power densities, and resistance variations are first quantified over an operating temperature range between -30 ℃ to 60 ℃ and then directly compared for the two electrolytes. In order to study the interfacial reactions and different diffusion behaviors of electrolytic ions of the two electrolytes at various operating temperatures, electrochemical impedance spectroscopy (EIS) data are simulated with an equivalent circuit model. Through analyzing these simulated impedance data, the energy barriers against kinetic reactions (charge transfer, adsorption) and diffusion processes are estimated for different temperature regions.

6.2 Experimental

For the fabrication of EDLC cells, activated carbon was used to produce the electrode film, as following the same procedure in Chapter 3. To compare the thermal characteristics of two different electrolytes, 1 M organic (Et_4NBF_4/PC) and 3 M aqueous (H_2SO_4) electrolytes were prepared, respectively. To simulate operating temperatures from -30 to 60 ℃, the coin cell was placed in a climate chamber.

The electrochemical characteristics were evaluated at different temperatures by means of cyclic voltammetery (CV) and constant current charging/discharging (CCD) measurements. During the CCD tests, the cells were assessed for their resistive behaviors and equivalent series resistances (ESR) by measuring the IR drop at discharge processing. As discussed in

Chapter 4, the overall internal resistance in a cell is represented by the calculated ESR values, while the equivalent capacitance (C) values were determined by using following equation

$$C = \frac{\Delta I \cdot \Delta t}{V_{max} - V_{min}} \tag{56}$$

where ΔI is the current of discharge, Δt is the discharging period, V_{max} is equal to V_{rated} (2.4 V in 1M Et_4NBF_4/PC, 0.8 V in 3M H_2SO_4, respectively) and V_{min} = ½ V_{max}.

Each electrochemical impedance spectroscopy (EIS) analysis was performed. From Bode plots, the capacitance and resistance at frequency 10 mHz were obtained by taking the real components of the impedance at different temperatures. These values were correlated with the specific capacitance and internal resistances (ESR) obtained from the constant current charging/discharging measurements. In order to investigate how temperature affects the properties of the electrolytes and hence the performance of the EDLC, the EIS spectrum was simulated with a previously proposed equivalent circuit as shown in Figure 4.2 (c). Still, each impedance simulated at 10 mHz was processed to obtain the correlation between the calculated total impedances and the measured ESR values.

6.3 Results and Discussion

6.3.1 Characterization of Thermal Behaviors

Figure 6.1 shows cyclic voltammograms measured on cells at each operating temperature from -30 ℃ to 60 ℃ for the two electrolytes. The CV curves in Figure 6.1 (a), obtained from the aqueous electrolyte (3 M H_2SO_4) demonstrate a saturated area of the current responses in the temperature range from -20 ℃ to 25 ℃, which represents the steady charge/discharge capacity. However, the current response was de-saturated at -30 ℃. This behavior is attributed to the water-based electrolytes characteristics which experience phase-change at close to their freezing points. For example, the freezing point of sulfuric acid solution (96 %) is about -20 ℃ [183], which leads to a low current response. At low temperatures in comparison to the aqueous electrolyte, the organic electrolyte (1 M Et_4NBF_4/PC) current responses are more distorted from the ideal rectangular shape, as shown in Figure 6.1 (b).

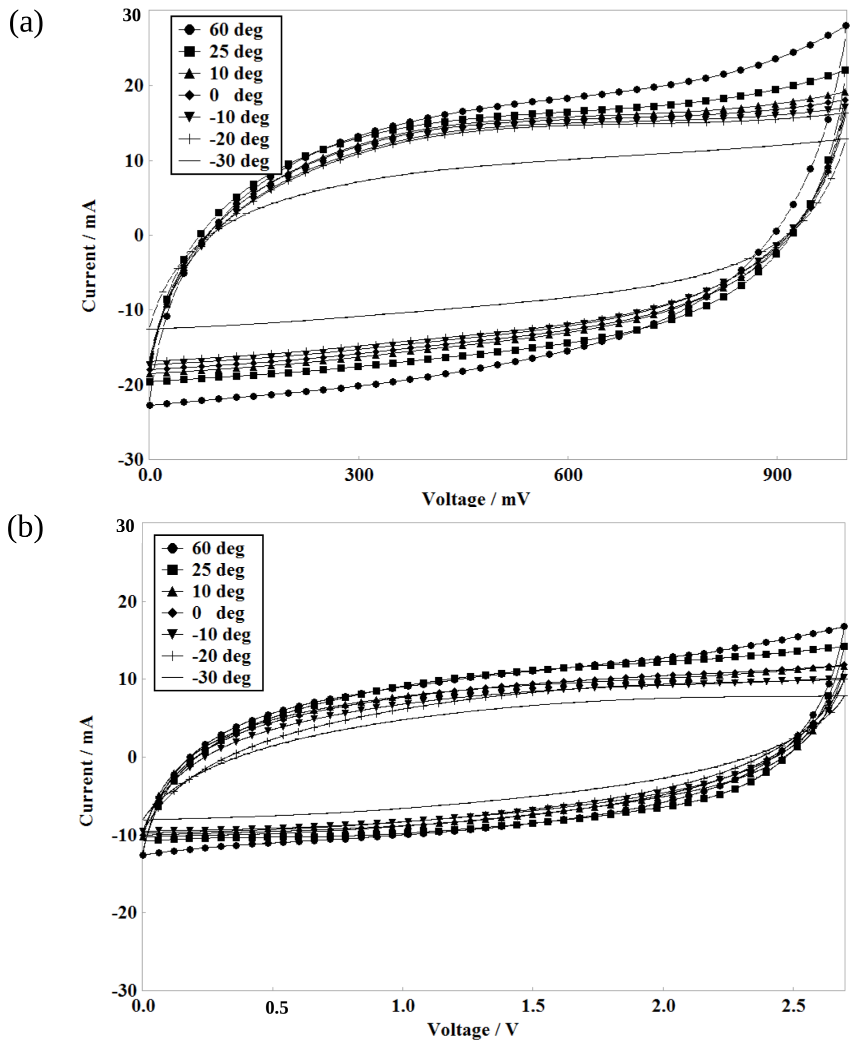

Figure 6.1 Cyclic voltammetry of (a) 3M H_2SO_4 and (b) 1M Et_4NBF_4/PC electrolyte at operating temperature from -30 to 60 ℃ at a scan rate of 20 mV/s , respectively

In general, there is a slow rise in current at the beginning of each charge/discharge process, which is caused by the internal resistance (ESR) of a cell. When it comes to the effect of temperature, a slower current rise in current and two rounded corners of the rectangle were observed at the beginning of the charge and discharge processes at lower temperatures. This indicates a significant increase in internal resistance, especially for the non-aqueous electrolyte, as the operating temperature goes down. The decreasing rates were found to be dependent on temperature. This observation agrees with previous studies [184]. On the other hand, both electrolytes displayed the slightly sharp tails of CV curves near to 1 V in H_2SO_4 and 2.7 V in Et_4NBF_4/PC when the temperature is at 60 ℃. This is caused by the decomposition of electrolytes [185].

One important issue of temperature change on an EDLC is the ability to retain specified performance levels, including capacitance, internal resistance and power/energy density. These characteristics for each electrolyte were evaluated by the constant current charge/discharge measurements.

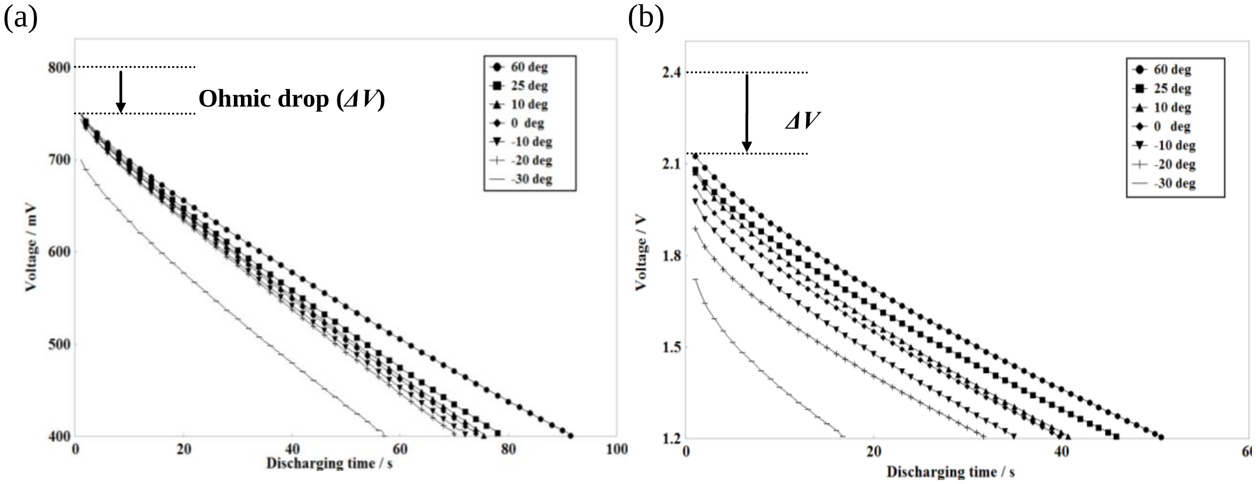

Figure 6.2 Discharging process at constant current (30 C rate) and ohmic drop (ΔV) for (a) 3M H_2SO_4 and (b) 1M Et_4NBF_4/PC electrolyte at various temperatures, respectively

Figure 6.2 shows discharge curves of a cell at different temperatures operating at a constant current density of 0.13 A/g in H_2SO_4 and 0.28 A/g in Et_4NBF_4/PC electrolyte, respectively. In this figure, the IR drop was observed at the beginning of discharging process. The voltage drop (Ohmic drop) was used to estimate the internal resistance (ESR) deviation with temperature change. As a result, Figure 6.3 shows the plots of the specific capacitance retention of EDLCs and ESR variation calculated from the discharging curves in Figure 6.2. The aqueous electrolyte was studied over the temperature range of -20 – 60 ℃, and its specific capacitance was found to change from110 F/g to 130 F/g, which indicates a maximum loss of 15 % of its capacitance. The capacitance decreases to around 100 F/g at the temperature of -30 ℃. On the other hand, the organic electrolyte showed a loss of 32 % of its capacitance, from 80 F/g at 25 ℃ to 52 F/g at -30 ℃. For the temperature effect on the internal resistance, the aqueous electrolyte showed an increase of 10 % in ESR, while the organic electrolyte displayed a more significant increase of 60 % over the tested temperature range. Both electrolytes measured their highest resistance at -30 ℃. This is attributed to the instability of electrolytes near their freezing temperatures. Moreover, it should be noticed that the variations of ESR and the capacitance can result in lowering of energy/power density as shown below:

$$\text{Energy density (Wh/kg)} = \frac{1}{2\text{m}}\text{CV}^2 \tag{57}$$

$$\text{Power density (W/kg)} = \frac{1}{4\text{m}}\frac{\text{V}^2}{\text{ESR}} \tag{58}$$

where m is the mass of an electrode and V is the operating voltage. In general, the organic electrolyte can provide larger energy/power densities than the aqueous ones due to the greater operating voltage.

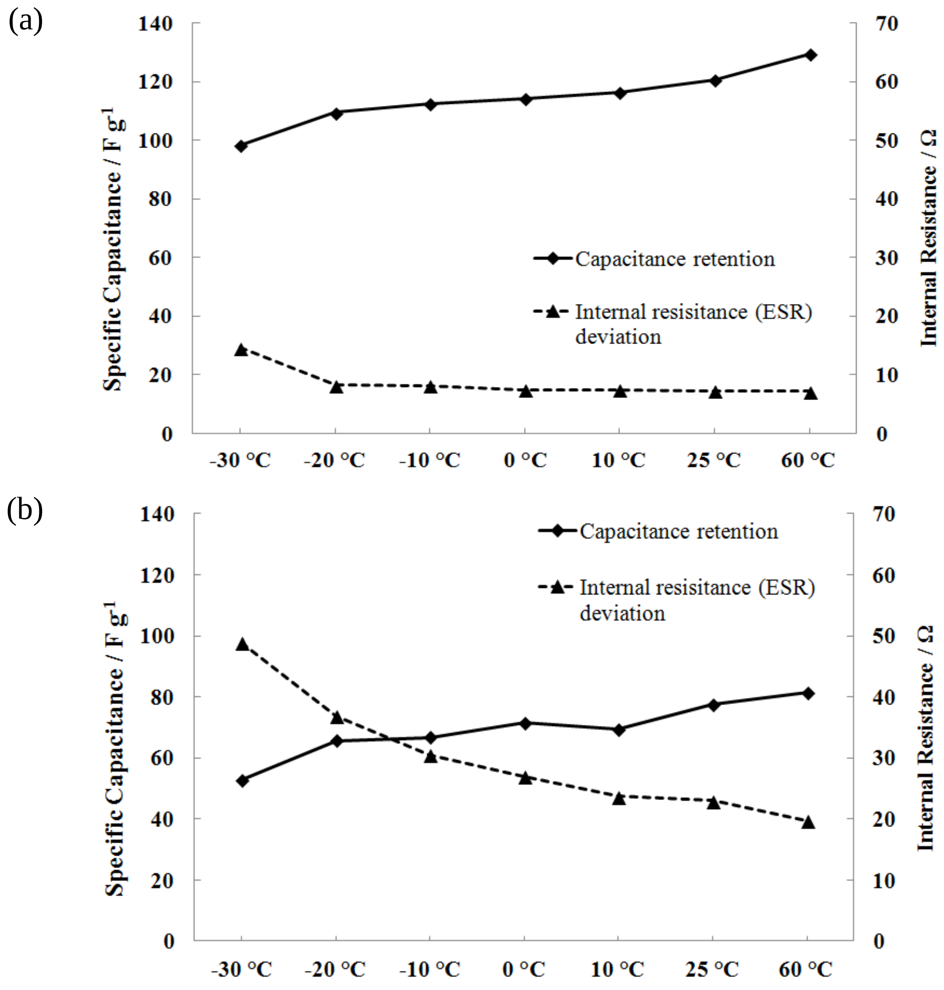

Figure 6.3 Capacitance retention and internal resistance (ESR) deviation for (a) 3M H_2SO_4 and (b) 1M Et_4NBF_4/PC electrolyte depending on temperatures, respectively

In contrast, in Figure 6.4 it is can be seen that as the temperatures decreases, the organic electrolyte showed a decrease in both energy and power densities while no significant change is observed in the aqueous electrolyte. The organic electrolyte achieved a power density of 470 W k/g at -30 ℃, 580 W/kg at 60 ℃ and an energy density of 1.8 Wh/kg (-30 ℃), 6.3 Wh/kg (60 ℃), respectively. Whereas, a power density of around 100 W/kg and an energy density of 1.7 Wh/kg over the entire temperature range were observed in the case of the aqueous electrolyte. This characteristic is associated with the variation of their capacitance and ESR with change in temperature as shown in Figure 6.3.

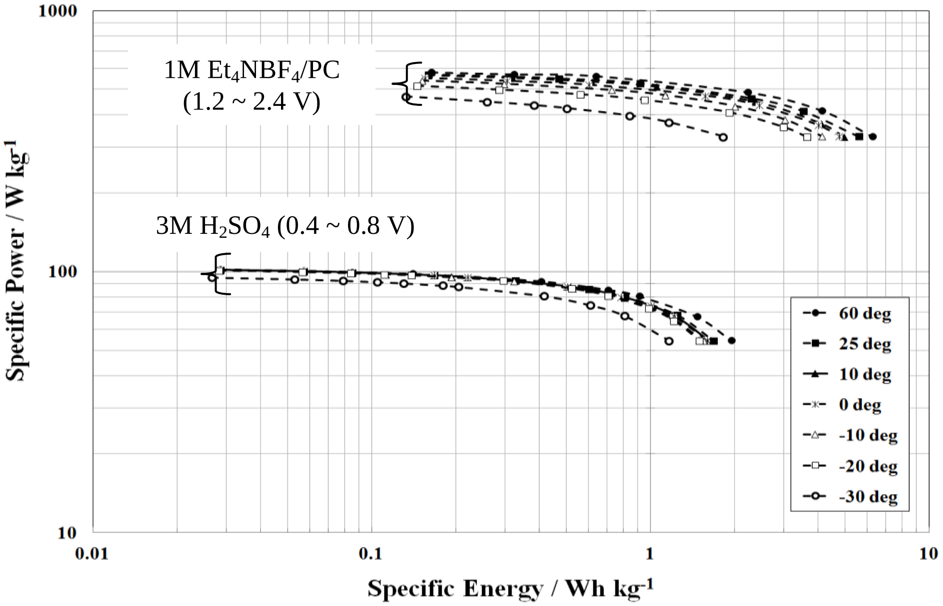

Figure 6.4 Ragone chart with specific power (W/kg)/energy density (Wh/kg) for 3M H_2SO_4 and 1M Et_4NBF_4/PC electrolytes operating from V_{min} to V_{max} at different temperatures

Figure 6.5 depicts the Nyquist plots, where x-axis is the real impedance and y-axis is the imaginary impedance, measured from 10 mHz to 100 kHz at different temperatures for each electrolyte. For both electrolytes, the curves were right-shifted with decreasing temperature, which means increasing resistances. In comparing the two electrolytes the organic electrolyte shows more right-shifted in its curves, shown in Figure 6.5 (a) and (b), indicating a larger deviation in resistance over the given temperature change. In the Nyquist plot, the first intersection of the x-axis in the high-frequency region relates to the ohmic resistance of the electrolyte while the diameter of following semicircle in the mid-frequency region provides information on the interfacial resistance of the EDLC device. Compared to the aqueous electrolyte resistances shown in Figure 6.5 (a), the organic electrolyte resistances, shown in Figure 6.5 (b), both display greater dependency on temperature.

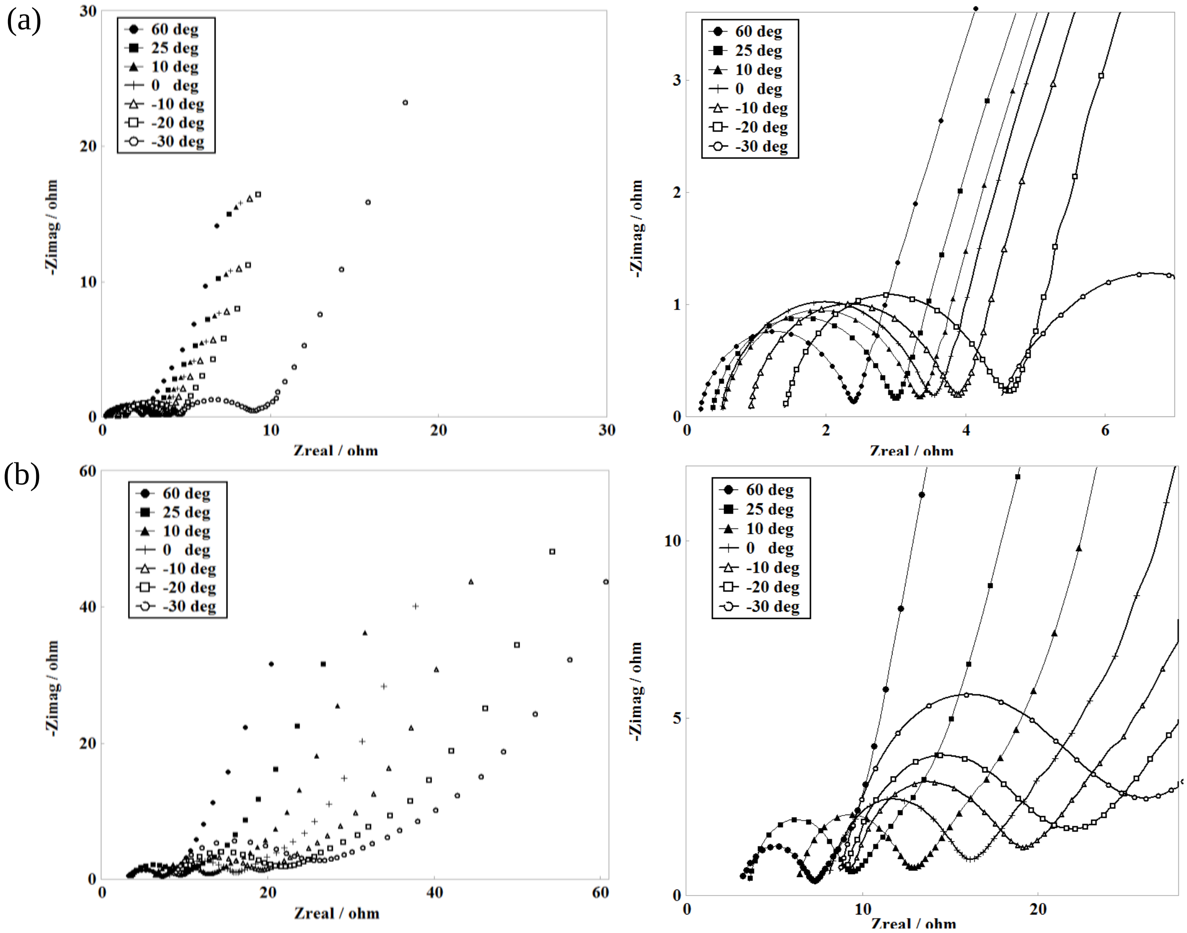

Figure 6.5 Nyquist plots for cells in (a) 3M H_2SO_4 and (b) 1M Et_4NBF_4/PC electrolytes, including enlarged images at right side

This phenomenon is in agreement with the result from the constant current charge/discharge study. The capacitive behavior of the electrolytes is investigated by studying the slopes of corresponding vertical curves (seen in the enlarged images in Figure 6.5). At low frequencies, an ideal capacitor would provide a straight line with frequency decreasing. It can be obviously observed that the aqueous electrolyte shows the nearly linear slopes while the slopes from the organic electrolyte decline as decreasing temperature. This indicates that the aqueous electrolyte produces stable capacitances while the values of the organic electrolyte significantly decrease with a lower temperature. The same tendency was found in the Bode plots, see Figure 6.6 and Figure 6.7.

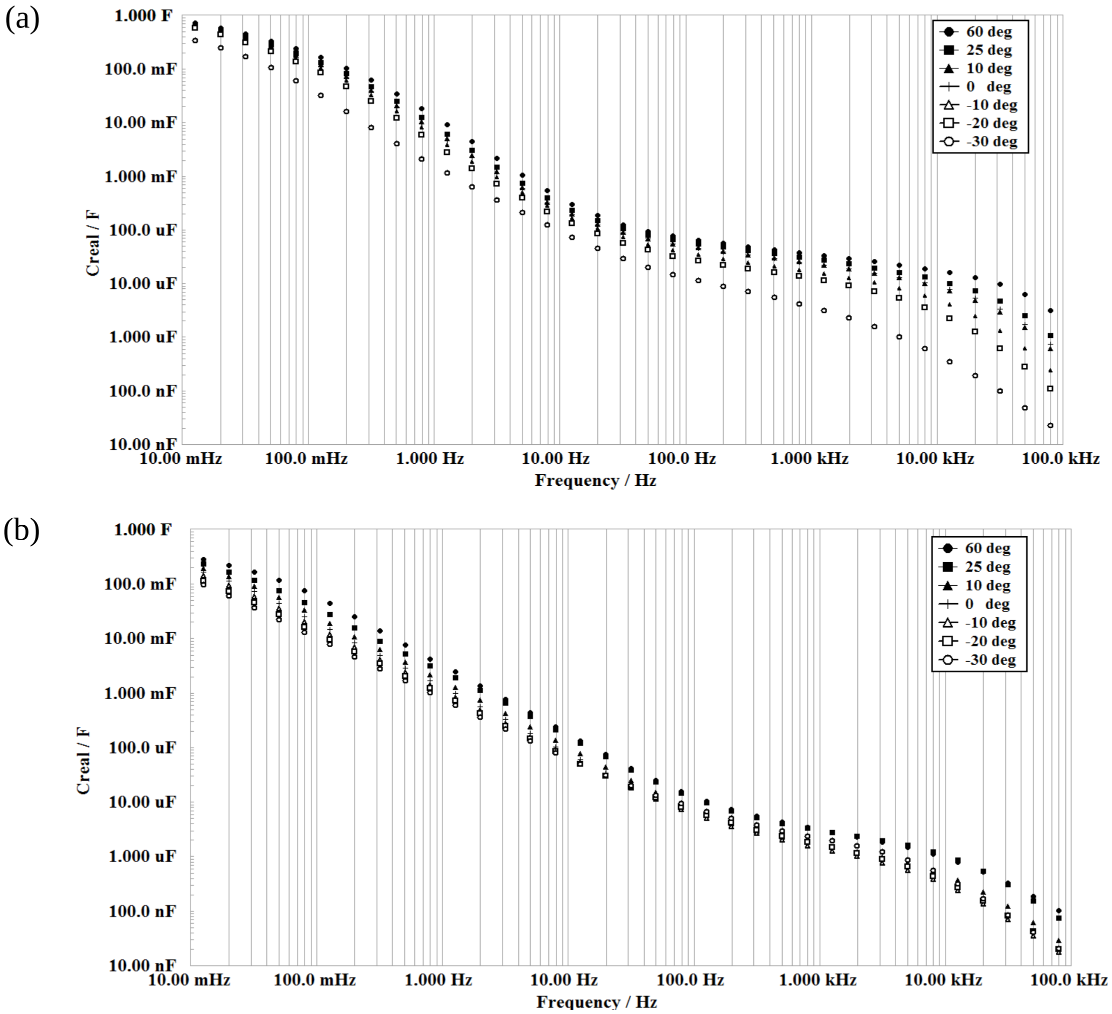

Figure 6.6 Bode plots of real capacitance for (a) 3M H_2SO_4 and (b) 1M Et_4NBF_4/PC electrolytes

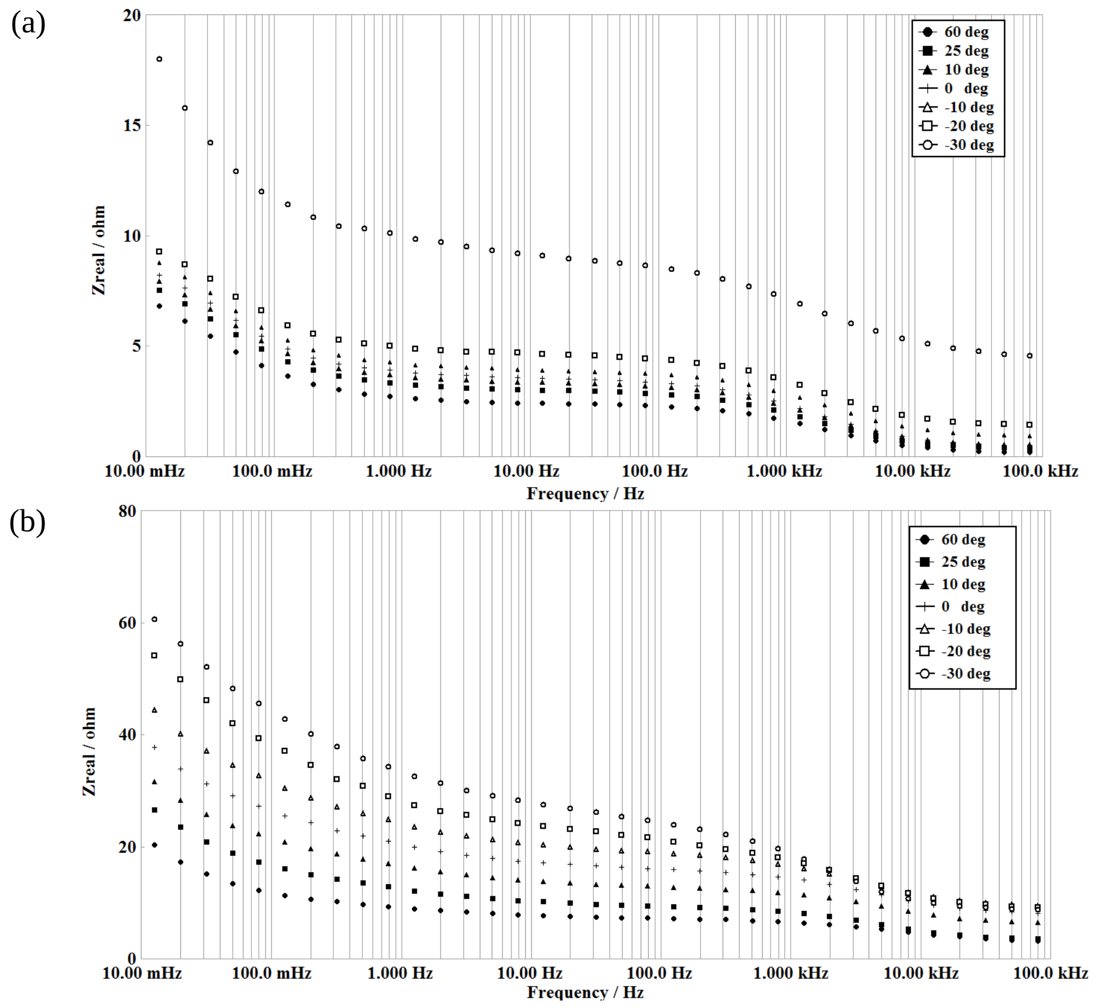

Figure 6.7 Bode plots of real impedance for (a) 3M H_2SO_4 and (b) 1M Et_4NBF_4/PC electrolytes

Figure 6.6 demonstrates that the capacitance in 10 mHz was reduced by decreasing the operating temperature. This variation is more considerable than in that of the organic electrolyte. Similarly, for the real resistance shown in Figure 6.7, the aqueous electrolyte's resistances increase slightly with decreasing temperature, while the organic electrolyte shows a larger temperature dependency.

6.3.2 EIS Simulations and Temperature-dependent Reactions

Through the EIS circuit model simulation the electrolytes' resistive and capacitive behaviors with respect to temperature were further investigated. The goal was to identify which electrochemical reaction is the dominant one in determining the overall performance of an EDLC device. As shown in Figure 4.2 (c), the proposed equivalent circuit model provides individual components corresponding to electrochemical processes that include the following: bulk processes (C_{bulk}, R_{bulk}), diffusion (W), interfacial reactions (R_{int}) and double-layer capacitance (C_H, C_{ads}). To determine the capacitance, the simulated values from the circuit model and the measured ones from Bode plots at 10 mHz were compared in Table 6.1.

Table 6.1 Simulated specific capacitances (F/g) from the circuit model vs. measured ones from Bode plots at 10 mHz for (a) 3M H_2SO_4 and (b)1M Et_4NBF_4/PC with different temperatures

(a)

H_2SO_4	Simulated				Measured
Temperature	C_{bulk}	C_H	C_{ads}	C_{total} ($C_{bulk} + C_H + C_{ads}$)	C_{total}
-30 ℃	3.1E-03	50.6	20.5	71.1	61.3
-20 ℃	4.1E-03	84.6	29.2	113.8	102.0
-10 ℃	4.1E-03	86.8	35.1	121.9	104.9
0 ℃	3.9E-03	86.6	38.1	124.7	108.6
10 ℃	4.4E-03	84.1	36.9	120.9	111.5
25 ℃	4.4E-03	87.5	40.3	127.8	115.8
60 ℃	4.6E-03	94.8	43.8	135.6	124.1

(b)

Et_4NBF_4 / PC	Simulated				Measured
Temperature	C_{bulk}	C_H	C_{ads}	C_{total} ($C_{bulk} + C_H + C_{ads}$)	C_{total}
-30 ℃	6.7E-04	16.9	24.7	41.6	33.5
-20 ℃	7.9E-04	25.3	29.0	54.3	40.2
-10 ℃	7.8E-04	24.9	31.3	56.2	49.2
0 ℃	8.7E-04	28.1	35.0	63.1	55.2
10 ℃	8.3E-04	28.6	42.4	71.1	63.3
25 ℃	1.1E-03	28.5	51.3	79.8	72.8
60 ℃	8.8E-04	29.5	64.3	93.8	79.1

As a result, the bulk capacitance is very low compared to the values of other two capacitances. The bulk capacitance value (around 4 μF) is of the order of micro-farad, which implies the practical capacitance in an EDLC is mainly attributed to the values of C_H and C_{ads}. Consequently, for the organic electrolyte total simulated specific capacitance (C_{total}) is from 54 to 80 F/g, while the aqueous one is around 125 F/g within the temperature range from -20 to 25 ℃. Although these values are slightly higher than the measured ones (with maximum error of 10 %), the simulated capacitances follow the same trend as indicated by measurements for thermal capacitive behaviors in both electrolytes. According to literature [186], the adsorption reaction is accelerated/decelerated by temperature changes, resulting in deviation of C_{ads}. This phenomenon is more significant in the organic electrolyte as illustrated in Table 6.1 (b). This increase significant is attributed to the organic electrolyte's lower conductance and slow reactivity of absorbable species compared to the aqueous electrolyte.

The EIS simulation was used to determine individual resistances of the bulk electrolyte process, the diffusion and interfacial reactions in the EDLC device, and to explain the variation in ESR with temperature from the constant current charge/discharge measurements. The simulated values of each resistive element defined in the equivalent circuit are summarized in Table 6.2. The external series resistance (R_S) and bulk electrolyte's resistance (R_{bulk}) correspond to the electrolyte ohmic resistance and the current leakage from bulk electrolyte's processes, respectively. For both resistances, the aqueous electrolyte showed a significantly less variation with temperature than the organic electrolyte. The R_S of the aqueous electrolyte varied from 1.3 to 0.2 Ω, and the R_{bulk} changes from 3.2 to 2.5 Ω with the temperature ranging from -20 to 60 ℃, whereas the organic ones range from 9.5 to 2.8 Ω (Rs) and from 12.5 to 4.4 Ω (R_{bulk}). These deviations are closely related to the electrolyte's change in conductivity with temperature. In literature, it was found that organic electrolytes have much lower conductivity (30~40 mS/cm at 25 ℃) than aqueous ones (550~700 mS/cm at 25 ℃) and shows a parabolic change with temperature [187]. Therefore, the organic electrolyte displays a larger variation in R_S and R_{bulk}, and its temperature dependencies are more significant.

Table 6.2 Simulated resistances from the circuit model for (a) 3M H_2SO_4 and (b) 1M Et_4NBF_4/PC with different temperatures

(a)

H_2SO_4	Simulated			
Temperature	R_S (ohm)	R_{bulk} (ohm)	W (ohm/$s^{1/2}$)	R_{int} (ohm)
-30 ℃	4.42	4.42	1.45	6.50
-20 ℃	1.35	3.21	1.32	5.58
-10 ℃	0.86	2.95	1.35	5.23
0 ℃	0.45	2.97	1.33	4.53
10 ℃	0.49	2.74	1.23	0.62
25 ℃	0.31	2.58	1.28	0.24
60 ℃	0.17	2.14	1.06	0.13

(b)

Et_4NBF_4 / PC	Simulated			
Temperature	R_S (ohm)	R_{bulk} (ohm)	W (ohm/$s^{1/2}$)	R_{int} (ohm)
-30 ℃	9.68	16.89	15.44	33.80
-20 ℃	9.48	12.55	9.93	21.62
-10 ℃	8.97	9.72	6.36	15.48
0 ℃	7.92	7.42	4.16	11.24
10 ℃	6.09	6.60	3.58	8.38
25 ℃	3.44	5.84	3.08	7.69
60 ℃	2.85	4.39	2.23	5.29

The diffusion resistance (W) and interfacial resistance (R_{int}), are other crucial factors that influence the ESR in the equivalent circuit. In the case of the aqueous electrolyte, W is around 1.3 Ω regardless of the temperature, while R_{int} ranges from 0.1 to 0.6 Ω and 4.5 to 6.5 Ω, in high (60 to 0 ℃) and low (0 to -30 ℃) temperature regions respectively. In contrast, the organic electrolyte shows a gradual decrease in both W (from 15 Ω at -30 ℃ to 2 Ω at 60 ℃) and R_{int} (from 33 Ω at -30 ℃ to 5 Ω at 60 ℃). These different characteristics of the two resistances indicate the diffusion and interfacial processes are strongly associated with the electrolyte's properties.

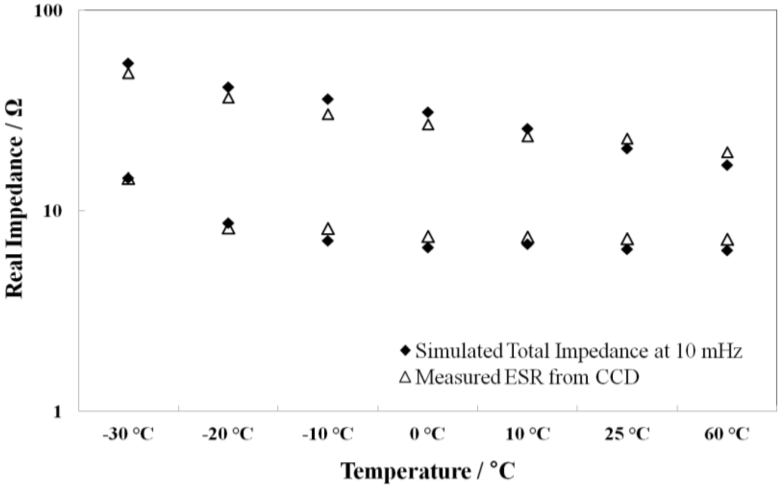

Figure 6.8 Correlation between the simulated total impedance at 10 mHz and the measured ESR from CCD measurement in log scale

In addition, the total real impedance simulated at 10 mHz is correlated with the measured ESR from CCD measurement in Figure 6.8. For both electrolytes, the simulated values are similar to the ESR estimation and present appropriately the temperature dependence of the resistance. This implies the resistive behavior of two electrolytes can be fairly accurately simulated by this equivalent circuit.

The thermal behaviors of kinetic reactions and diffusion can be rationalized quantitatively by the measured values of resistances from the EIS simulation. The temperature dependence of the double-layer interfacial resistance (referred to R_{int}) and the diffusion resistance (referred to W) of the electrolyte can be interpreted in terms of the activation energy (E) according to the Arrhenius equation [188, 189]:

$$\kappa_T = \kappa_0 \exp\left(-\frac{\Delta G}{kT}\right) \ or \ R_T = R_0 \exp\left(-\frac{\Delta G}{kT}\right) \tag{59}$$

where κ_T is the reaction rate, κ_o is a constant, k is the Boltzmann's constant, T is the absolute temperature. By replacing κ by the values of R_{int} or W in Table 6.2 and then plotting ln(R) versus 1/T, the activation energy G of the corresponding process can be obtained from the slope of the lines as shown in Figure 6.9. The variation of the two resistances indicates the energy barrier against the charge-transferring through the double-layer interfaces (R_{int}) and ion's migration towards the double layer (W). Both resistances decrease when temperature increases. This phenomenon implies that a higher temperature enlarges the free spaces, enabling it to transfer charges and reduce migration frictions, which decreases the activation energies of kinetic reactions (G_K) and diffusion (G_D). Additionally, it is realized that both activation energies can be distinguished into two temperature regions, for below and above 0℃, respectively, which have different slopes. The G_K and G_D of the organic electrolyte have comparable values in the low-temperature region (3.02 kJ/mol and 3.64 kJ/mol) and in the high-temperature region (1.95 kJ/mol and 1.69 kJ/mol), respectively, showing that their resistances are affected by the temperature change similarly in both regions.

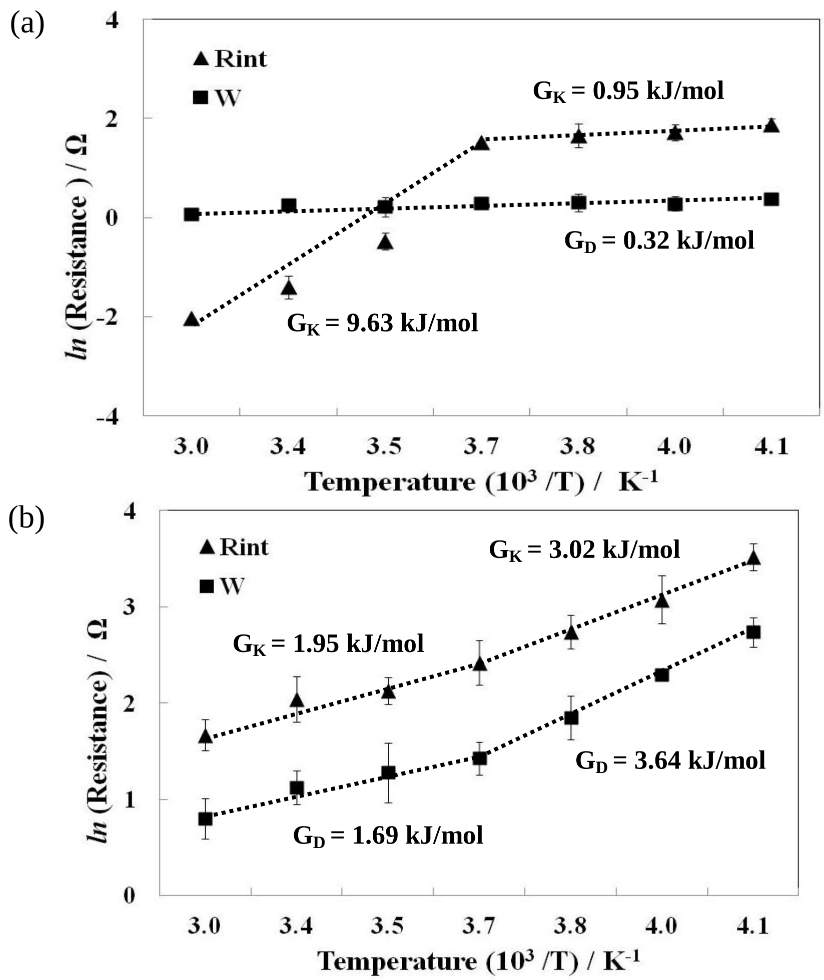

Figure 6.9 An Arrhenius plot of the temperature dependency of kinetic and diffusion resistances in (a) H_2SO_4 and (b) Et_4NBF_4/PC electrolyte

In contrast, the diffusion process in the aqueous electrolyte exhibits the same activation energy (G_D) of 0.32 kJ/mol for these two temperature regions. This energy is much less than the corresponding values of the organic electrolyte. The value of G_K (0.95 kJ/mol) is however less than the value for the organic one (3.02 kJ/mol) in the low temperature region, but its value (9.63 kJ/mol) is much larger than the value for the organic one (1.95 kJ/mol) in the high temperature region. This indicates that, the kinetic reactions of the aqueous electrolyte are greatly affected by the operating temperature, especially close to 0 ℃. This may be explained by that, the aqueous-typed ions become tightly packed with water-molecules at near the freezing point of water, and hence require some enormous kinetic energy to transfer the charge (or ions) at the interfacial double-layer. Below 0 ℃ and in the low-temperature region, the activation energy for the kinetic reactions becomes smaller and the kinetic processes at interface are less dependent on temperature changes.

6.4 Summary

The electrochemical performance of EDLCs assembled with two electrolytes, aqueous (H_2SO_4) and organic (Et_4NBF_4/PC), was systematically evaluated in a temperature range of -30 ℃ to 60 ℃. The temperature dependency of EDLCs for aqueous and organic electrolytes was explained based on CV, constant current charge/discharge, and EIS analysis. The capacitance, internal resistance and energy/power densities of the two capacitors were deduced from electrochemical measurements. The aqueous electrolyte performance was found to be less dependent on operating temperature, exhibiting less variation of capacitance, resistance and energy/power densities as compared to the organic electrolyte. Electrochemical impedance spectroscopy and simulation results with the equivalent circuit were extensively investigated. The simulated resistive/capacitive characteristics were correlated with the measured capacitance and internal resistance from the CCD measurements. Meanwhile, simulated resistances were interpreted to understand the kinetic and diffusion behaviors within the interested temperature range. For the aqueous electrolyte both the kinetic and diffusion behaviors are relatively insensitive to temperature changes from 0 to -30 ℃, however, higher energy barriers exist for the kinetic reactions and diffusion within the range between 0℃ to 60 ℃. For the organic electrolyte, the comparable energy barriers exist for kinetic reactions and diffusion, both for the low temperature and high temperature regions.

Chapter 7 Conclusions and Future Work

7.1 Conclusions

The work presented in this thesis is expected to contribute significantly to the development of nano-structured carbon electrodes and improving our understanding of their electrochemical, thermal and dynamic properties for electrochemical double-layer capacitors (EDLCs) through both experimental and numerical study. The following conclusions are drawn from this research.

First, using the electrophoretic deposition method (EPD), SWCNT coated electrodes were fabricated from functionalized CNT suspensions with various pH values. The SWCNT electrodes fabricated with a higher pH yielded an increased surface area and more-effective pore size distribution, leading to a higher specific capacitance. In addition, the measurements of electrochemical impedance revealed that the pore size distribution optimized through modifying the pH values reduced the internal resistance of SWCNT electrodes. This investigation, detailed in Chapter 3, will help optimize the structural properties of nano-structured electrodes, which can be used in the design of advanced EDLCs with high energy density.

Second, based on the theoretical description of double-layer interfaces, a new equivalent circuit model, composed of three main capacitors (C_{bulk}, C_H and C_{ads}) and resistances (R_{bulk}, R_{ct} and R_{ads}), was developed and verified through experiments and simulations. This model, described in Chapter 4, is useful in investigating the electrochemical and dynamic behaviors of EDLCs with carbon-based electrodes. In particular, the proposed circuit model provides a more straightforward way to address ions' kinetics and diffusion reactions at double-layer regions. These reactions are critical to determine the capacitive and resistive characteristics of EDLCs. The impedance behavior of EDLCs with two distinct electrolytes was studied to evaluate the validity of the circuit modeling, and the results suggested that this model is able to sufficiently simulate the characteristics of EDLCs, including their potential dependency.

Third, the dependence of electrochemical characteristics on the structural properties of porous carbon electrodes was experimentally investigated, especially these dynamic responses of porous activated carbon, graphene and SWCNT electrodes, which are represented by their morphology, surface area and distinguishable pore volume distributions to pore sizes (PDS). Both graphene and SWCNT electrodes, having a wider PSD in the meso-/macro-pore range, exhibit a greater capacitance retention and lower interfacial resistance in high-frequency operations than those of activated carbon electrodes with a narrow PSD in micro-pores. The temperature-dependent capacitive and resistive behaviors were also compared to investigate the role of porous carbon electrodes in EDLC's performance for operation in the temperature range between -30 ℃ and 60℃. Mesoporous graphene and SWCNT electrodes were found to be more sensitive to temperature change due to their larger portion of meso-pores, resulting in a larger variation in capacitance and resistance than microporous activated carbon electrodes. This work is covered in Chapter 5, and the detailed characteristics of the electrodes are summarized in Table 7.1.

Finally, the characterization of the thermal behavior of two distinct electrolytes, namely aqueous and organic, was carried out to improve the performance of EDCLs in a way compatible with electrolytes capable of stable and wider temperature operation. The aqueous electrolyte performance was found to be less dependent on operating temperatures from -

20 ℃ to 60℃, exhibiting less variation of capacitance, resistance and energy/power densities than the organic electrolyte. This finding corresponds to the fact that the aqueous electrolyte shows relatively weaker energy barriers against the kinetic and diffusion reactions at double layer interfaces.

Table 7.1 Structural and electrical properties of porous carbon electrodes, and their electrochemical and thermal behaviors

Electrode	Activated Carbon	Graphene	SWCNT
Structural properties	3-D porous network randomly agglomerated Surface area : 1560 m^2g^{-1} Pore size distributed from 1 to 3nm (Ave. 2.1nm)	2-D sheet typed accumulation Surface area: 550 m^2g^{-1} Pore size from 3 to 10nm (Ave. 6.2nm)	1-D porous randomly dispersed network Surface area: 640 m^2g^{-1} Pore size from 8 to 20nm (Ave. 7.0nm)
Electrical properties	Low conductivity (0.1~1 S/cm) Highest ohmic drop Large Rs	Highest conductivity (~106 S/cm) Lowest ohmic drop Smallest Rs	High conductivity (~105 S/cm) Low ohmic drop Small Rs
Electrochemical behavior	Specific capacitance of 96 F/g (with 1M Et_4NBF_4/PC) Slow current response for fast charging/discharging Long relaxation time (τ_0)	Specific capacitance of 88F/g Fast current response Short τ_0	Specific capacitance of 89 F/g Fast current response Shortest τ_0
Thermal behavior	Capacitance retention of 46% Internal resistance variation up to 33% Relatively small change in Cap.&Res. under freq. Require low activation energies for ion kinetic reaction (G_K of 3.0 kJ/mol below 0℃) Linearly drop in energy/power densities at low temperatures	Capacitance retention of 36% Internal resistance variation up to 55% Large change in Cap.&Res. under freq. (especially below 0℃) Large G_K of 4.5 kJ/mol Gradually drop in energy/power densities	Capacitance retention of 39% Internal resistance variation up to 68% Larger change in Cap.&Res. under freq. (especially below 0℃) Largest G_K of 7.5 kJ/mol More gradually drop in Energy/Power densities

7.2 Future Work

Although a number of important conclusions have been made in this study, several phenomena reported here need further investigations. Some recommendations for the future work are listed below:

First, with the approach presented in Chapter 3, EPD processing at higher pH values yields SWCNT electrodes with increased surface area and more-effective pore size distribution, resulting in the capacitance of around 100 F/g. However, capacitance values still remain lower than those for ACs. This result is mainly attributed to a lower mass of active material and the thickness of the electrodes. The maximum weight of SWCNT films achieved by EPD processing is about 3 mg with a thickness of about 20 µm, neither of which is sufficient to evaluate a material's performance in practice, including its energy or power density. Sample electrodes used in demonstration should be of comparable thickness and mass of an actual electrode, similar to those of commercial electrodes (100 to 200 µm or about 10 mg/cm^2 of carbon film). To increase the electrode under test's mass and thickness, it is better to develop multi-layered SWCNT films by employing printing techniques with functionalized SWCNT suspension at high pH values.

Second, the equivalent circuit model developed in this study can be used to characterize the operation parameters of EDLCs that store energy through non-Faradaic processes. It cannot be used to model the pseudo-capacitors which utilize pure Faradaic reactions, such as reversible redox reactions created by using conducting polymers and metal oxides. To apply it for all typed-EC systems, the model needs to be improved by modifying C_{ads} and R_{ads}, which corresponds to the redox reactions at double-layer regions.

Thirdly, in this thesis work two types of electrolytes: aqueous and organic, were studied. Another type of electrolyte, ionic liquids (ILs), is suggested and being developed as a superior alternative in terms of potential window for operation (up to 4V) and simplified purification. A number of ILs have recently been introduced to increase power and energy densities. However, it is known that ILs still fail to satisfy the requirements for applications in the temperature range -30 ℃ to 60 ℃ where ECs are mainly used. Therefore, further development and characterization of ILs is required to completely understand the properties of EDLCs based on different types of electrolytes with the same carbon electrodes.

References

[1] H. Ibrahim; A. Linca; J. Perron, Energy storage systems - Characteristics and comparisons, Renewable & Sustainable Energy Reviews, vol. 12, pp. 1221-1250, 2008.

[2] I. B. Weinstock, Recent advances in the US Department of Energy's energy storage technology research and development programs for hybrid electric and electric vehicles, Journal of Power Sources, vol. 110, pp. 471-474, 2002.

[3] M. Koot; J. Kesseis; W. Heemels, Energy management strategies for vehicular electric power systems, Ieee Transactions on Vehicular Technology, vol. 54, pp. 771-782, 2005.

[4] A. F. Burke, Batteries and ultracapacitors for electric, hybrid, and fuel cell vehicles, IEEE, vol. 95, 2007.

[5] M. Zandi; B. Davat; F. Meibody-Tabar, Energy management of a fuel cell/supercapacitor/battery, power source for electric vehicular applications, Ieee Transactions on Vehicular Technology, vol. 60, pp. 433-443, 2011.

[6] R. Walawalkar; R. Mancini, Economics of electric energy storage for energy arbitrage and regulation in New York, Energy Policy, vol. 35, pp. 2558-2568, 2007.

[7] T. N. C. Haisheng Chen; Wei Yang; Yulong Ding, Progress in electrical energy storage system: a critical review, Progress in Natural Science, vol. 19, pp. 291-312, 2009.

[8] M. L. Lazarewicz; T.M. Ryan, Integration of flywheel-based energy storage for frequency regulation in deregulated markets, 2010.

[9] S. G. Chalk; J. E. Miller, Key challenges and recent progress in batteries, fuel cells, and hydrogen storage for clean energy systems, Journal of Power Sources, vol. 159, pp. 73-80, 2006.

[10] M. A. Kashem; G. Ledwich, Energy requirement for distributed energy resources with battery energy storage for voltage support in three-phase distribution lines, Electric Power Systems Research, vol. 77, pp. 10-23, 2007.

[11] M. I. M. Morita; Y. Matsuda, Lithium-ion batteris: Wiley, 1998.

[12] M. Jayalakshmi; K. Balasubramanian, Simple capacitors to supercapacitors - An overview, International Journal of Electrochemical Science, vol. 3, pp. 1196-1217, 2008.

[13] A. F. B. J.R Miller, "Electrochemical capacitors: challenges and opportunities for real-world applications," electrochemical society interface, vol. 17, pp. 53-57, 2008.

[14] Image courtesy US defense and Logistics Agency (2011), in http://www.mpoweruk.com/performance.htm, ed.

[15] Nuintek. Comparison of capacitor, supercapacitor and battery [Online]. Available: http://www.nuin.co.kr

[16] R. Kotz; M. Carlen, Principles and applications of electrochemical capacitors, Electrochimica Acta, vol. 45, pp. 2483-2498, 2000.

[17] Conway, Electrochemical Supercapacitors : Scientific fundamentals and technological applications. New York: Kluwer Academic/Plenum Press, 1999.

[18] D. A. S. a. A. Palencsar, Batteries and electrochemical capacitors, The electrochemical society interface, vol. 15, pp. 17-22, 2006.

[19] K. Rand, DOE panel on advanced energy storage systems calls for materials research, MRS bulletin, vol. 32, p. 464, 2007.

[20] P. B. Simon; A.F., Nanostructured carbons: Double-layer capacitance and more, electrochemical society interface, vol. 17, pp. 38-43, 2008.

[21] R. A. Huggins, Supercapacitors and electrochemical pulse sources, Solid State Ionics, vol. 134, pp. 179-195, 2000.

[22] S. A. Hashmi, Supercapacitor: An emerging power source, National Academy Science Letters-India, vol. 27, pp. 27-46, 2004.

[23] M. T.; Wang Li-hing; Michio Inagaki, Dependence of electric double layer capacitance of activated carbon on the types of pores and their surface area, New carbon materials, vol. 23, pp. 111-115, 2008.

[24] G. Wang, L. Zhang; J. Zhang, A review of electrode materials for electrochemical supercapacitors, Chemical Society Reviews, vol. 41, pp. 797-828, 2012.

[25] F.-y. Kang; H. Du, Carbon for energy storage and conversion, New carbon materials, vol. 26, pp. 246-254, 2011.

[26] J. Gamby; P.L. Taberna; P. Simon, Studies and characterisations of various activated carbons used for carbon/carbon supercapacitors, Journal of Power Sources, vol. 101, pp. 109-116, 2001.

[27] L. L. Zhang; X. S. Zhao, Carbon-based materials as supercapacitor electrodes, Chemical Society Reviews, vol. 38, pp. 2520-2531, 2009.

[28] M. Lazzari; F. Soavi; M. Mastragostino, Mesoporous carbon design for ionic liquid-based double-layer supercapacitors, Fuel Cells, vol. 10, pp. 840-847, 2010.

[29] P. S. Weiss; S.K. Kim, Vertial aligment of single-walled caron nanotube films formed by electrophoretic deposition, Langmuir, vol. 24, pp. 12936-12942, 2008.

[30] G. L.; A.B. Fuertes; E. Frackowiak, Templated mesoporous carbons for supercapacitor application, Electrochimica Acta, vol. 50, pp. 2799-2805, 2005.

[31] H. V. Helmholtz, Ueber einige gesetze der vertheilung elektrischer ströme in körperlichen leitern, mit anwendung auf die thierisch-elektrischen versuche, Ann. Phys. Chem, vol. 89, pp. 211-233, 1853.

[32] D. L. Chapman, A contribution to the theory of electrocapillarity, Philosophical Magazine, vol. 25, pp. 475-481, 1913.

[33] O. Stern, The theory of the electrolytic double shift, Zeitschrift Fur Elektrochemie Und Angewandte Physikalische Chemie, vol. 30, pp. 508-516, 1924.

[34] G. Gouy, Constitution of the electric charge at the surface of an electrolyte, Journal of Physics, vol. 9, pp. 441-467, 1910.

[35] R. H. Fowler; E. A. Guggenheim, Statistical thermodynamics: Cambridge University Press, 1939.

[36] B. E. Conway, Ionic hydration in chemistry and biophysics, edited Amsterdam: Elsevier, 1981.

[37] K. R. Prasad; N. Munichandraiah, Fabrication and evaluation of 450 F electrochemical redox supercapacitors using inexpensive and high-performance,

polyaniline coated, stainless-steel electrodes, Journal of Power Sources, vol. 112, pp. 443-451, 2002.

[38] A. Clemente; S. Panero; B. Scrosati, Solid-state, polymer-based, redox capacitors, Solid State Ionics, vol. 85, pp. 273-277, 1996.

[39] X. Lan; A. Hirata; M. Chen, Nanoporous metal/oxide hybrid electrodes for electrochemical supercapacitors, Nature Nanotechnology, vol. 6, pp. 232-236, 2011.

[40] Q. X. Jia; S.G. Song; X.D. Wu, Epitaxial growth of highly conductive RuO_2 thin films on (100) Si, Applied Physics Letters, vol. 68, pp. 1069-1071, 1996.

[41] A. J. F. Bard; Larry R., Electrochemical methods: fundamentals and applications, 2nd ed.: New York: Chichester England: John Wiley, 1994.

[42] D. C. Grahame, The electrical double layer and the theory of electrocapillarity, Chemical Reviews, vol. 41, pp. 441-501, 1947.

[43] V. F. Lvovich, Impedance spectroscopy: Applications to Electrochemical and Dielectric phenomena. New Jersey: John Wiley & Sons, Inc., 2012.

[44] J. R. Miller; D.A. Evans, Design and performance of high-reliability double-layer capacitors, 40th Electronic Components and Technology Conference, Vols 1 and 2, pp. 289-297, 1990.

[45] B. E. Conway; W.G. Pell; T.C. Liu, Diagnostic analyses for mechanisms of self-discharge of electrochemical capacitors and batteries, Journal of Power Sources, vol. 16, 1997.

[46] H. Yang; Y. Zhang, Self-discharge analysis and characterization of supercapacitors for environmentally powered wireless sensor network applications, Journal of Power Sources, vol. 196, pp. 8866-8873, 2011.

[47] A. M. Oickle; H. A. Andreas, Examination of water electrolysis and oxygen reduction as self-discharge mechanisms for carbon-based, aqueous electrolyte electrochemical capacitors, Journal of Physical Chemistry C, vol. 115, pp. 4283-4288, 2011.

[48] J. Kowal; E. Avaroglu; A.S. Enfelds; D.U. Sauer, Detailed analysis of the self-discharge of supercapacitors, Journal of Power Sources, vol. 196, pp. 573-579, 2011.

[49] H. S. Chen; Y. Ding, Progress in electrical energy storage system: A critical review, Progress in Natural Science, vol. 19, pp. 291-312, 2009.

[50] H. S. Deyang Qu, Studies of activated carbons used in double-layer capacitors, Journal of Power Sources, vol. 74, pp. 99-107, 1998.

[51] R. Lin; Taberna; P.L.; Chmiola, J., Microelectrode study of pore size, ion size, and solvent effects on the charge/discharge behavior of microporous carbons for electrical double-layer capacitors, Journal of Electrochem. Soc., vol. 156, pp. A7-A12, 2009.

[52] Y. D. Yunpu Zhai; D. Zhao; S. Dai, Carbon materials for chemical capacitive energy storage, Advanced Materials, vol. 23, pp. 4828-4850, 2011.

[53] P. Simon; Y. Gogotsi, Materials for electrochemical capacitors, Nature Materials, vol. 7, pp. 845-854, 2008.

[54] V. N. Popov, Carbon nanotubes: properties and application, Materials Science & Engineering R-Reports, vol. 43, pp. 61-102, 2004.

[55] A. G. Pandolfo; A. F. Hollenkamp, Carbon properties and their role in supercapacitors, Journal of Power Sources, vol. 157, pp. 11-27, 2006.

[56] E. Frackowiak, Carbon materials for supercapacitor application, Physical Chemistry Chemical Physics, vol. 9, pp. 1774-1785, 2007.
[57] Z. Wang; M. A. Fierke; A. Stein, Functionalization of porous carbon materials with designed pore architecture, Advanced Materials, vol. 21, pp. 265-293, 2009.
[58] N. Shimodaira; A. Masui, Raman spectroscopic investigations of activated carbon materials, Journal of Applied Physics, vol. 92, pp. 902-909, 2002.
[59] A. Jane; H. Kurig; E. Lust, Characterisation of activated nanoporous carbon for supercapacitor electrode materials, Carbon, vol. 45, pp. 1226-1233, 2007.
[60] B. Z. Fang; L. Binder, A novel carbon electrode material for highly improved EDLC performance, Journal of Physical Chemistry B, vol. 110, pp. 7877-7882, 2006.
[61] P. Azais; P. Florian; M.A. Lillo-Rodenas; F. Beguin, Causes of supercapacitors ageing in organic electrolyte, Journal of Power Sources, vol. 171, pp. 1046-1053, 2007.
[62] M. Zh; C.J. Weber; A.M. Bittner, Chemical and electrochemical ageing of carbon materials used in supercapacitor electrodes, Carbon, vol. 46, pp. 1829-1840, 2008.
[63] J. Chmiola; Celine Largeot, Relation betweeen the ion size and pore size for an electric double-layer capacitor, Journal of American Chemical Society, vol. 130, pp. 2730-2731, 2008.
[64] J. Chmiola; Y. Gogotsi; P.L. Taberna, Anomalous increase in carbon capacitance at pore sizes less than 1 nanometer, Science, vol. 313, pp. 1760-1763, 2006.
[65] R. M. Reilly, Carbon nantubes: Potential benefits and risks of nanotechnology in unclear medicine, Journal of Nuclear Medicine, vol. 48-7, pp. 1039-1042, 2007.
[66] M. Inagaki; H. Konno; O. tanaike, Carbon materials for electrochemical capacitors, Journal of Power Sources, vol. 195, pp. 7880-7903, 2010.
[67] A. Peigne; C. Laurent; E. Flahaut; R.R. Bacsa; A. Rousset, Specific surface area of carbon nanotubes and bundles of carbon nanotubes, Carbon, vol. 39, pp. 507-514, 2001.
[68] C. Liu; F. Li; L.P. Ma; H.M. Cheng, Advanced materials for energy storage, Advanced Materials, vol. 22, 2010.
[69] C. M. Niu; E.K. Sichel; H. Tennent, High power electrochemical capacitors based on carbon nanotube electrodes, Applied Physics Letters, vol. 70, pp. 1480-1482, 1997.
[70] R. Z. Ma; B. Zhang; C.L. Wu, Study of electrochemical capacitors utilizing carbon nanotube electrodes, Journal of Power Sources, vol. 84, pp. 126-129, 1999.
[71] K. H. An, W.S. Kim; D.J. Bae; Y.H Lee, Electrochemical properties of high-power supercapacitors using single-walled carbon nanotube electrodes, Advanced Functional Materials, vol. 11, pp. 387-392, 2001.
[72] S. Shiraishi; H. Kurihara; K. Okabe; D. Hulicova; A. Oya, Electric double layer capacitance of highly pure single-walled carbon nanotubes in propylene carbonate electrolytes, Electrochemistry Communications, vol. 4, pp. 593-598, 2002.
[73] C. Emmenegger; P. Mauron; P. Sudan; P. Wenger; V. Hermann; R. Gallay; A. Zuttel, Investigation of electrochemical double-layer (ECDL) capacitors electrodes based on carbon nanotubes and activated carbon materials, Journal of Power Sources, vol. 124, pp. 321-329, 2003.

[74] C. Y. Liu; A.J. Bard; F. Wudl; I. Weitz; J.R. Heath, Electrochemical characterization of films of single-walled carbon nanotubes and their possible application in supercapacitors, Electrochemical and Solid State Letters, vol. 2, pp. 577-578, 1999.

[75] C. S. Du; D. Heldbrant; N. Pan, Preparation and preliminary property study of carbon nanotubes films by electrophoretic deposition, Materials Letters, vol. 57, pp. 434-438, 2002.

[76] L. Cooper; H. Amano; M. Hiraide; S. Houkyou; I.Y. Jang; Y.J. Kim; H. Muramatsu; J.H. Kim; T. Hayashi; Y.A. Kim; M. Endo; M.S. Dresselhaus, Freestanding, bendable thin film for supercapacitors using DNA-dispersed double walled carbon nanotubes, Applied Physics Letters, vol. 95, 2009.

[77] K. Kordas; T. Mustonen; G. Toth; H. Jantunen; M. Lajunen; C. Soldano; S. Talapatra; S. Kar; R. Vajtai; P.M. Ajayan, Inkjet printing of electrically conductive patterns of carbon nanotubes, Small, vol. 2, pp. 1021-1025, 2006.

[78] P. Chen; H. Chen; C. Zhou, Inkjet printing of single-walled carbon nanotube/RuO2 nanowire supercapacitors on cloth fabrics and flexible substrates, Nano Research, vol. 3, pp. 594-603, 2010.

[79] X. Zhao; B.T.T. Chu; B. Ballesteros; W. Wang; C. Johnston; J.M. Sykes; P.S. Grant; Spray deposition of steam treated and functionalized single-walled and multi-walled carbon nanotube films for supercapacitors, Nanotechnology, vol. 20, 2009.

[80] M. Kaempgen; C.K. Chan; J. Ma; Y. Cui; G. Gruner, Printable thin film supercapacitors using single-walled carbon nanotubes, Nano Letters, vol. 9, pp. 1872-1876, 2009.

[81] S. W. Lee, et al., Nanostructured carbon-based electrodes: bridging the gap between thin-film lithium-ion batteries and electrochemical capacitors, Energy & Environmental Science, vol. 4, pp. 1972-1985, 2011.

[82] D. Zilli, et al., Effect of alignment on adsorption characteristics of self-oriented multi-walled carbon nanotube arrays, Nanotechnology, vol. 17, pp. 5136-5141, 2006.

[83] H. Zhang, et al., Comparison between electrochemical properties of aligned carbon nanotube array and entangled carbon nanotube electrodes, Journal of the Electrochemical Society, vol. 155, pp. K19-K22, 2008.

[84] Q. L. Chen, et al., Fabrication and electrochemical properties of carbon nanotube array electrode for supercapacitors, Electrochimica Acta, vol. 49, pp. 4157-4161, 2004.

[85] W. Lu, et al., High performance electrochemical capacitors from aligned carbon nanotube electrodes and ionic liquid electrolytes, Journal of Power Sources, vol. 189, pp. 1270-1277, 2009.

[86] E. Frackowiak, et al., Enhanced capacitance of carbon nanotubes through chemical activation, Chemical Physics Letters, vol. 361, pp. 35-41, 2002.

[87] J. Y. Lee, et al., Fabrication of supercapacitor electrodes using fluorinated single-walled carbon nanotubes, Journal of Physical Chemistry B, vol. 107, pp. 8812-8815, 2003.

[88] B. J. Yoon, et al., Electrical properties of electrical double layer capacitors with integrated carbon nanotube electrodes, Chemical Physics Letters, vol. 388, pp. 170-174, 2004.

[89] S. B. Dolly Shin; C. Yan; B. H. Hong, Synthesis and applications of graphene electrodes, Carbon Letters, vol. 13, pp. 1-16, 2012.

[90] J. T. Qian Cheng; Jun Ma; Han Zhang; Lu-Chang Qin, Graphene and carbon nanobue composite electrodes for supercapacitors with ultra-high energy density, Physical Chemistry Chemical Physics, vol. 13, pp. 17615-17624, 2011.

[91] Y. Wang, et al., Supercapacitor Devices Based on Graphene Materials, Journal of Physical Chemistry C, vol. 113, pp. 13103-13107, 2009.

[92] S. R. C. Vivekchand, et al., Graphene-based electrochemical supercapacitors, Journal of Chemical Sciences, vol. 120, pp. 9-13, 2008.

[93] M. D. Stoller, et al., Graphene-Based Ultracapacitors, Nano Letters, vol. 8, pp. 3498-3502, 2008.

[94] Y. Huang, et al., An Overview of the Applications of Graphene-Based Materials in Supercapacitors, Small, vol. 8, pp. 1805-1834, 2012.

[95] Q. Du, et al., Preparation of functionalized graphene sheets by a low-temperature thermal exfoliation approach and their electrochemical supercapacitive behaviors, Electrochimica Acta, vol. 55, pp. 3897-3903, 2010.

[96] Y. Chen, et al., Electrophoretic deposition of graphene nanosheets on nickel foams for electrochemical capacitors, Journal of Power Sources, vol. 195, pp. 3031-3035, 2010.

[97] J. J. Moore, et al., Fabrication and characterization of single walled nanotube supercapacitor electrodes with uniform pores using electrophoretic deposition, Materials Chemistry and Physics, vol. 134, pp. 68-73, 2012.

[98] J. Cho, et al., Characterisation of carbon nanotube films deposited by electrophoretic deposition, Carbon, vol. 47, pp. 58-67, 2009.

[99] Z. C. Wu, et al., Transparent, conductive carbon nanotube films, Science, vol. 305, pp. 1273-1276, 2004.

[100] A. A. Green and M. C. Hersam, Colored semitransparent conductive coatings consisting of monodisperse metallic single-walled carbon nanotubes, Nano Letters, vol. 8, pp. 1417-1422, 2008.

[101] M. K. Marco Fritsch; Michael Schneider; Mathias Weiser, Scaleable electrode manufacturing technology for supercapas, German Federal Ministry of Education and Research, 2008.

[102] N.-S. P; J. A. Lim; J.H. Choi, Fabrication and characterization of a porous carbon electrode for desalination of brackish water, Desalination, vol. 238, pp. 37-42, 2009.

[103] L. Besra; M. Liu, A review on fundamentals and applications of electrophoretic deposition (EPD), Progress in Materials Science, vol. 52, pp. 1-61, 2007.

[104] B. J. C. Thomas, et al., Electrophoretic deposition of carbon nanotubes on metallic surfaces," in Electrophoretic Depositon: Fundamentals and Applications, vol. 314, pp. 141-146, 2006,.

[105] A. Y. Wu; Vilarinho P. M.; Kingon, A. I., Electrophoretic deposition of lead zirconate titanate films on metal foils for embedded components, Journal of Americal Ceramic Society, vol. 89, pp. 575-581, 2006.

[106] G. Cao; D. Liu, Template-based synthesis of nanorod, nanowire, and nanotube arrays, Advances in Colloid and Interface Science, vol. 136, pp. 45-64, 2008.

[107] A. R. Boccaccini, et al., Electrophoretic deposition of carbon nanotubes, Carbon, vol. 44, pp. 3149-3160, 2006.

[108] B. Gao, et al., Fabrication and electron field emission properties of carbon nanotube films by electrophoretic deposition, Advanced Materials, vol. 13, pp. 1770-1773, 2001.

[109] B. J. C. Thomas, et al., Multi-walled carbon nanotube coatings using electrophoretic deposition (EPD), Journal of the American Ceramic Society, vol. 88, pp. 980-982, 2005.

[110] C. Du; N. Pan, Supercapacitors using carbon nanotubes films by electrophoretic deposition, Journal of Power Sources, vol. 160, pp. 1487-1494, 2006.

[111] Y. Yang, et al., Electrophoresis coating of titanium dioxide on aligned carbon nanotubes for controlled syntheses of photoelectronic nanomaterials, Advanced Materials, vol. 19, pp. 1239, 2007.

[112] B. Smith, et al., Influence of surface oxides on the colloidal stability of multi-walled carbon nanotubes: A structure-property relationship, Langmuir, vol. 25, pp. 9767-9776, 2009.

[113] B. Smith, et al., Colloidal properties of aqueous suspensions of acid-treated, multi-walled carbon nanotubes, Environmental Science & Technology, vol. 43, pp. 819-825, 2009.

[114] H. Gu; T. M. Swager, Fabrication of free-standing, conductive, and transparent carbon nanotube films, Advanced Materials, vol. 20, pp. 4433-4437, 2008.

[115] M. B. Jakubinek, et al., Novel method to produce single-walled carbon nanotube films and their thermal and electrical properties, Journal of Nanoscience and Nanotechnology, vol. 10, pp. 8151-8157, 2010.

[116] H. L. N.; A.B. McEwen; K. Le, Electrochemical properties of Imidazolium salt electrolytes for electrochemical capacitor applications, Journal of Electrochemical society, vol. 146, pp. 1687-1695, 1999.

[117] A. Lewandowski; M. Galinski, Practical and theoretical limits for electrochemical double-layer capacitors, Journal of Power Sources, vol. 173, pp. 822-828, 2007.

[118] S. Brunauer, et al., Adsorption of gases in multimolecular layers, Journal of the American Chemical Society, vol. 60, pp. 309-319, 1938.

[119] S. Vaquero, et al., Insights into the influence of pore size distribution and surface functionalities in the behaviour of carbon supercapacitors, Electrochimica Acta, vol. 86, pp. 241-247, 2012.

[120] Christopher M.; A. Brett, Electrochemistry: principles, methods, and applications: Oxford University Press, 1993.

[121] B. Xu, et al., Highly mesoporous and high surface area carbon: A high capacitance electrode material for EDLCs with various electrolytes, Electrochemistry Communications, vol. 10, pp. 795-797, 2008.

[122] W.-Y. Tsai, et al., Ordered mesoporous silicon carbide-derived carbon for high-power supercapacitors, Electrochemistry Communications, vol. 34, pp. 109-112, 2013.

[123] T. W. Thomas JM, Principles and practice of heterogeneous catalysis, pp. 257-275, 1997.

[124] K. K. Horvath G, Method for the calculation of effective pore size distribution in molecular sieve carbon, Journal of Chemical Engineering Japan, vol. 16, pp. 470-475, 1983.

[125] F. H. Sito A, Curvature and parametric sensitivity in models for adsorption in micropores, AIChE Journal, vol. 37, pp. 429-436, 1991.

[126] G. K. Lastoskie C; Quirke N., Pore size heterogeneity and the carbon slit pore: a density functional theory model, Langmuir, vol. 9, pp. 2693-2702, 1993.

[127] Y. W. Fanxing Li, Characterization of single-wall carbon nanotubes by N2 adsorption, Carbon, vol. 42, pp. 2375-2383, 2004.

[128] F. R. Reinoso; D.L. Valladares, Characterization of active carbons: the influence of the method in the determination of the pore size distribution, Carbon, vol. 36, pp. 1491-1499, 1998.

[129] A. Lasia, Modeling of impedance of porous electrodes, in Modeling and Numerical Simulations ed: Springer New York, 2009, pp. 67-137.

[130] S. R. Taylor; E. Gileadi, Physical interpretation of the warburg impedance, Corrosion, vol. 51, pp. 664-671, 1995.

[131] Z. M. Markovic, et al., The effect of oxidation on structureal and electrical properties of single wall carbon nantubes, Hemijska Industrija, vol. 65, pp. 363-370, 2011.

[132] L. xiang, The effect of carbonyl, carboxyl and hydroxyl groups on the capacitance of carbon nantubes, New carbon materials, vol. 26, pp. 224-228, 2011.

[133] S. Buller, et al., Modeling the dynamic behavior of supercapacitors using impedance spectroscopy, in Conference Record of the 2001 Ieee Industry Applications Conference, Vols 1-4, ed, 2001, pp. 2500-2504.

[134] E. J. Brandon, et al., Extending the low temperature operational limit of double-layer capacitors, Journal of Power Sources, vol. 170, pp. 225-232, 2007.

[135] P. Liu, et al., Influence of temperature and electrolyte on the performance of activated-carbon supercapacitors, Journal of Power Sources, vol. 156, pp. 712-718, 2006.

[136] R. Kotz, et al., Temperature behavior and impedance fundamentals of supercapacitors, Journal of Power Sources, vol. 154, pp. 550-555, 2006.

[137] K. Hung, et al., Wide-temperature range operation supercapacitors from nanostructured activated carbon fabric, Journal of Power Sources, vol. 193, pp. 944-949, 2009.

[138] E. Iwama, et al., Characterization of commercial supercapacitors for low temperature applications, Journal of Power Sources, vol. 219, pp. 235-239, 2012.

[139] R. S. Hastak, et al., All solid supercapacitor based on activated carbon and poly 2,5-benzimidazole for high temperature application, Electrochimica Acta, vol. 59, pp. 296-303, 2012.

[140] C. Masarapu, et al., Effect of Temperature on the Capacitance of Carbon Nanotube Supercapacitors, Acs Nano, vol. 3, pp. 2199-2206, 2009.

[141] R. S. Hastak, et al., High temperature all solid state supercapacitor based on multi-walled carbon nanotubes and poly 2,5 benzimidazole, Journal of Solid State Electrochemistry, vol. 16, pp. 3215-3226, 2012.

[142] H. El Brouji, et al., Comparison between changes of ultracapacitors model parameters during calendar life and power cycling ageing tests, Microelectronics Reliability, vol. 48, pp. 1473-1478, 2008.

[143] H. G. F. Rafik; R. Gallay; A. Crausaz; A. Berthon, Frequency, thermal and voltage supercapacitor characterization and modeling, Journal of Power Sources, vol. 165, pp. 928-934, 2007.

[144] M. D. S.; R. S. Ruoff, Best practice methods for determining an electrode material's performance for ultracapacitors, Energy & Environmental Science, vol. 3, pp. 1294-1301, 2010.

[145] G. Lota, et al., Carbon nanotubes and their composites in electrochemical applications, Energy & Environmental Science, vol. 4, pp. 1592-1605, 2011.

[146] Y. Yamada, et al., Capacitor properties and pore structure of single- and double-walled carbon nanotubes, Electrochemical and Solid State Letters, vol. 12, pp. K14-K16, 2009.

[147] A. Izadi-Najafabadi, et al., High-power supercapacitor electrodes from single-walled carbon nanotube composite, ACS Nano, vol. 5, pp. 811-819, 2011.

[148] A. Izadi-Najafabadi, et al., Extracting the full potential of single-walled carbon nanotubes as durable supercapacitor electrodes operable at 4 V with high power and energy Ddnsity, Advanced Materials, vol. 22, pp. E235, 2010.

[149] D. N. Futaba, et al., Shape-engineerable and highly densely packed single-walled carbon nanotubes and their application as super-capacitor electrodes, Nature Materials, vol. 5, pp. 987-994, 2006.

[150] M. Farbod, et al., Surface oxidation and effect of electric field on dispersion and colloids stability of multiwalled carbon nanotubes, Colloids and Surfaces Physicochemical and Engineering Aspects, vol. 384, pp. 685-690, 2011.

[151] M. F. Islam, et al., High weight fraction surfactant solubilization of single-wall carbon nanotubes in water, Nano Letters, vol. 3, pp. 269-273, 2003.

[152] L. L. Zeng, et al., Tailoring aqueous solubility of functionalized single-wall carbon nanotubes over a wide pH range through substituent chain length, Nano Letters, vol. 5, pp. 2001-2004, 2005.

[153] J.Y. Chang; Y.-T. Shieh, The effect of pH and ionic strength on the dispersion of carbon nanotubes in poly solutions, Polym Int, 2011.

[154] J. J. E. Moore, et al., Performance of nanotube-based electrodes from temperature-controlled electrophoretic deposition, Journal of Applied Electrochemistry, vol. 42, pp. 501-508, 2012.

[155] Y. S. Joung; C. R. Buie, Electrophoretic Deposition of Unstable Colloidal Suspensions for Superhydrophobic Surfaces, Langmuir, vol. 27, pp. 4156-4163, 2011.

[156] Y. T. Kim, et al., Drastic change of electric double layer capacitance by surface functionalization of carbon nanotubes, Applied Physics Letters, vol. 87, 2005.

[157] Y. Gogotsi; P. Simon, True performance metrics in electrochemical energy storage," Science, vol. 334, pp. 917-918, 2011.

[158] X. Li, et al., Modeling and control of aggregated supercapacitor energy storage system for wind power generation, 34th Annual Conference of the Ieee Industrial Electronics Society, Vols 1-5, Proceedings, ed, 2008, pp. 3259-3264.

[159] M. B. Camara, et al., Supercapacitors modeling and integration in transport applications," in 2011 IEEE Industry Applications Society Annual Meeting, 2011.

[160] S. Fiorenti, et al., Modeling and experimental validation of a Hybridized Energy Storage System for automotive applications, Journal of Power Sources, vol. 241, pp. 112-120, 2013.

[161] L. Zubieta; R. Bonert, Characterization of double-layer capacitors for power electronics applications, IEEE Transactions on Industry Applications, vol. 36, pp. 199-205, 2000.

[162] P. V.; G. R. Yasser Diab, Electrical, frequency and thermal measurement and modeling of supercapacitor performance, in 3rd European Symposium on Supercapacitors and Applications, Italy, 2008.

[163] C. T. That; B.W. Ricketts, Self-discharge of carbon-based supercapacitors with organic electrolytes, Journal of Power Sources, vol. 89, pp. 64-69, 2000.

[164] V. S. Muralidharan, Warburg impedance - Basics revisited, Anti-Corrosion Methods and Materials, vol. 44, pp. 26-&, 1997.

[165] R. Zhang, et al., Effects of ash contents of activated carbon on the performance of electric double layer capacitors, in Applications of Engineering Materials, pp. 1-4, vol. 287-290, 2011.

[166] S. Srinivasan, Fuel cells: from fundamentals to applications, Berlin, 2006.

[167] B. P. Bakhmatyuk, et al., Intercalation pseudo-capacitance in carbon systems of energy storage, Reviews on Advanced Materials Science, vol. 14, pp. 151-156, 2007.

[168] L. R. Falkner; A.J. Bard, Electrochemical methods, fundamentals and applications, New York: J. Wiley & Sons, 2001.

[169] P. Simon; J. F. Fauvarque; P. L. Taberna, Electrochemical characteristics and impedance spectroscopy studies of carbon-carbon supercapacitors, Journal of Electrochemical Society, vol. 150, pp. 292-300, 2003.

[170] A. Lewandowski, et al., Performance of carbon-carbon supercapacitors based on organic, aqueous and ionic liquid electrolytes, Journal of Power Sources, vol. 195, pp. 5814-5819, 2010.

[171] C. Z. Kai Liu; Rengui Lu; C. C. Chan, Improved study of temperature dependence equivalent circuit model for supercapacitors, presented at the Electromagnetic Launch Technology (EML), 2012 16th International Symposium, Beijing, 2013.

[172] L. Boulon, et al., Simulation model of a military HEV with a highly redundant architecture, IEE Transactions on Vehicular Technology, vol. 59, pp. 2654-2663, 2010.

[173] A. Du Pasquier, et al., Characteristics and performance of 500 F asymmetric hybrid advanced supercapacitor prototypes, Journal of Power Sources, vol. 113, pp. 62-71, 2003.

[174] P. Simon; Y. Gogotsi, Charge storage mechanism in nanoporous carbons and its consequence for electrical double layer capacitors, Philosophical Transactions of the Royal Society a-Mathematical Physical and Engineering Sciences, vol. 368, pp. 3457-3467, 2010.

[175] J. Wen; J. H. Kang; S. H. Jayaram; A. Yu; X. Wang, Development of an equivalent circuit model for electrochemical double layer capacitors (EDLCs) with distinct electrolytes, Electrochimica Acta, vol. 115, pp. 587-598, 2014.

[176] A. R. Paniego, Reporting physisorption data for gas-solid systems with special reference to the determination of surface area and porosity," Anales De Quimica Serie a-Quimica Fisica Y Quimica Tecnica, vol. 85, pp. 386-399, 1989.

[177] J. R.; K. S; F. Rouquerol, Adsorption by powders and porous solids : Principles, Methodology and Applications: Academic Press, 1999.

[178] P. L. Taberna, et al., Electrochemical characteristics and impedance spectroscopy studies of carbon-carbon supercapacitors, Journal of the Electrochemical Society, vol. 150, pp. A292-A300, 2003.

[179] J. Kang, et al., Characterization of thermal behaviors of electrochemical double layer capacitors (EDLCs) with aqueous and organic electrolytes, Electrochimica Acta, vol. 144, pp. 200-210, 2014.

[180] O. Pizio, et al., Electric double layer capacitance of restricted primitive model for an ionic fluid in slit-like nanopores: A density functional approach, Journal of Chemical Physics, vol. 137, 2012.

[181] D.-e. Jiang, et al., Oscillation of capacitance inside nanopores, Nano Letters, vol. 11, pp. 5373-5377, 2011.

[182] H. K. Song, et al., Electrochemical impedance spectroscopy of porous electrodes: the effect of pore size distribution, Electrochimica Acta, vol. 44, pp. 3513-3519, 1999.

[183] C. M. Gable, et al., "Phase equilibria of the system sulfur trioxide water, Journal of the American Chemical Society, vol. 72, pp. 1445-1448, 1950.

[184] W. G. Pell; B. E. Conway, Analysis of power limitations at porous supercapacitor electrodes under cyclic voltammetry modulation and dc charge, Journal of Power Sources, vol. 96, pp. 57-67, 2001.

[185] L. Demarconnay, et al., A symmetric carbon/carbon supercapacitor operating at 1.6 V by using a neutral aqueous solution, Electrochemistry Communications, vol. 12, pp. 1275-1278, 2010.

[186] M. F.; S. Vadim; F. Lvovich, Non-linear impedance analysis of industrial lubricants, Electrochimica Acta, vol. 53, pp. 7375-7385, 2008.

[187] T. R. Jow; S. P. Ding, Nonaqueous electrolyte development for electrochemical capacitors, U.S. Army Research Laboratory, Adelphi, 1999.

[188] G. Alcicek, et al., Experimental study of temperature effect on ultracapacitor ageing, 2007.

[189] A. B. Brett; Oliveira Brett; Ana Maria, Electrochemistry : principles, methods and applications, Oxford University Press, 1993.